学位論文

The FastSound Spectroscopic Redshift Survey at $z \sim 1.4$: Survey Design, Development of Data Analysis Method, and Production of Redshift Catalog

(赤方偏移1.4の宇宙論的分光サーベイ FastSound におけるサーベイデザインの検討、データ解析手法の開発および赤方偏移カタログの構築)

平成27年12月博士（理学）申請

東京大学大学院理学系研究科
天文学専攻
舎川 元成

Abstract

Constraining the nature of dark energy through galaxy redshift surveys is one of the most powerful way to investigate the origin of the accelerated expansion of our Universe. Redshift space distortion (RSD) seen in the 3-D galaxy distribution gives a measurement of the growth rate of structure $f\sigma_8$ and this value can be used to test General Relativity at a cosmological scale, because $f\sigma_8$ is sensitive to the modification of the theory of gravity. This test has been carried out by various redshift survey up to the effective redshift of $z \sim 0.7$, and FastSound is the first galaxy redshift survey using Fiber-Multi Object Spectrograph (FMOS) on Subaru Telescope aiming at RSD and measure the normalized structure growth rate $f\sigma_8$ to test the theory of gravity at $z \sim 1.4$. FastSound survey collects Hα emission lines ($6,563\mu$m in the rest frame) from star-forming galaxies with the wavelength coverage of 1.45–1.68μm (corresponding to redshift 1.2–1.55) to reveal the 3-D galaxy distribution. The survey started in March 2012 and completed in July 2014. This thesis presents the fundamentals of the FastSound survey focusing on the survey strategy, observations, data analysis, and production of the redshift catalog. The target selection method was examined in the pilot observation in September and October 2012, where the emission line detection rates of several selection methods are compared, and the selection based on photometric redshifts using five optical magnitudes of Canada-France-Hawaii telescope legacy survey (CFHTLS) was finally adopted for the main FastSound survey. The main observation was carried out over 35 nights from March 2012 to July 2014. The FMOS data were processed by the standard pipeline (*FIBRE-pac*) to obtain the reduced 2-D image used for an automated emission-line detection. To detect emission lines from spectroscopic data automatically is a key for treating large data of galaxy surveys, because this reduces the uncertainty of the cosmological implications caused by the non-uniformity of eye-inspection and allows an effective data processing. We developed a dedicated software algorithm (*FIELD*) for detecting emission line profiles in 2-D images. The use of bad pixel map produced by the standard pipeline and revaluation of noise-level near the OH airglow line, which happens in any ground near-infrared observations, drastically decreased the false detection rate by cosmic rays and OH lines. The performance of this algorithm was assessed by applying it to the "inverted image" which is obtained by exchanging object and sky frames in the

data reduction process by FIBRE-pac. As a result, we obtained $\sim 4,000$ redshifts of star-forming galaxies at median redshift of $z \sim 1.36$ with the signal-to-noise (S/N) ratio above 4.5, which is currently the largest galaxy sample beyond $z = 1$. The description is given of the FastSound redshift catalog, and based on this catalog, the $f\sigma_8$ measurement from the two-point correlation function is performed, giving $f\sigma_8 = 0.482^{+0.116}_{-0.116}$. This catalog can also be used for other studies related to star-forming galaxies at $z \sim 1.4$.

Contents

Chapter 1

Introduction

Understanding the Universe we live in has been a major concern for us for a long time and there have been repeated attempts to explain our Universe. Our view of the universe has evolved through experiencing many conceptual changes. The first object which people were interested in was the Sun, Moon, and five planets around us. In the ancient Greek, the model of Geocentrism was thought, where the Earth was placed at the center of the Universe and the motions of these objects were explained. This model was summarized by Ptolemy Claudius in 2nd century AD, and had survived for about 1500 years, because it succeeded in explaining the motion of the Sun and these planets reasonably well. However, it needed modifications in order to be consistent with observations later on, and as a result, Geocentrism became a rather complicated model. Geocentrism was displaced by a model proposed by Copernicus Nicolaus (1473–1543), where the Sun lay at the center with planets orbiting around it. He believed that he Universe should be simple, and this Heliocentrism model could reproduce the planetary motions naturally. Although he could explain the planetary motions no better than Geocentrism did because of the lack of the elliptical orbit in his theory, Kepler Johannes complemented it by analyzing the accumulated observational data of planetary motions finding that planetary motions are well explained by introducing elliptical motions, which is known as Kepler's laws. Kepler thought that some force exerted by the Sun governed the motion of planets, but was not able to clarify what it was. This idea was further examined by Newton, who applied his theories of gravitation and revealed that Kepler's laws can be explained by gravity, as well as the motion of objects on the ground. This justified the Heliocentrism model, and at the same time, it was demonstrated that the celestial and terrestrial laws were no longer separated and both are accountable by physics.

The modern cosmology was initiated by the progress of astronomical observations and the invention of General Relativity by Albert Einstein in 1915. A hundred years later today, the extremely accurate observational technology enables us to see the universe with an unprecedented precision, and some results imply that we may again need a radical change of our perspective of the Universe. In this chapter, we start with the fundamental equations of the basic model of the Universe based on General Relativity, review the current status of cosmological observation and newly emerged problem called "dark energy problem", and introduce the FastSound project and purpose of this thesis.

1.1 Equations of Homogeneous and Isotropic Universe

In General Relativity, the geometry of space-time and energy distribution are related by Einstein Equation

$$R_{\mu\nu} - \frac{1}{2}Rg_{\mu\nu} = \frac{8\pi G}{c^4}T_{\mu\nu} \tag{1.1.1}$$

where $R_{\mu\nu}$ is Ricci tensor and $R \equiv R_{\mu\nu}$ is Ricci scalar, both of which are functions of the metric $g_{\mu\nu}$, and $T_{\mu\nu}$ is energy-momentum tensor, specifying the source of energy. Metric relates 4-dimensional separation between events to the coordinates describing the position of the events

$$ds^2 = g_{\mu\nu}dx^\mu dx^\nu \tag{1.1.2}$$

and captures the structure of space-time. The cosmological solution for GR was first discovered by Friedman. The homogeneous and isotropic universe is described by the Friedmann-Robertson-Walker metric

$$ds^2 = -c^2dt^2 + a(t)^2\left(\frac{dr^2}{1-Kr^2} + r^2(d\theta^2 + \sin^2\theta d\phi^2)\right) \tag{1.1.3}$$

where r, θ, ϕ are spatial coordinates in the polar coordinates system, t is time, K is curvature, and $a(t)$, called scale factor, describes the expansion of the universe as a function of t. In this case, the explicit form of metric $g_{\mu\nu}$ is

$$g_{\mu\nu} = \begin{pmatrix} -c^2 & 0 & 0 & 0 \\ 0 & \dfrac{a(t)^2dr^2}{1-Kr^2} & 0 & 0 \\ 0 & 0 & a(t)^2r^2d\theta^2 & 0 \\ 0 & 0 & 0 & a(t)^2r^2\sin^2\theta d\phi^2 \end{pmatrix}. \tag{1.1.4}$$

Equation (1.1.3) can be re-expressed by setting $d\chi = dr/\sqrt{1-Kr^2}$,

$$ds^2 = -c^2dt^2 + a(t)^2[d\chi^2 + S_K(\chi)(d\theta^2 + \sin^2 d\phi^2)] \tag{1.1.5}$$

where

$$S_K(\chi) = \left\{ \begin{array}{ll} \dfrac{\sin\sqrt{K}\chi}{\sqrt{K}\chi} & (K>0) \\ \chi & (K=0) \\ \dfrac{\sinh\sqrt{-K}\chi}{\sqrt{-K}} & (K<0) \end{array} \right\}. \tag{1.1.6}$$

The physical separation between two points is $a(t)\chi$, rather than $a(t)r$.

In homogeneous and isotropic universe, energy-momentum tensor $T_{\mu\nu}$, the right-hand side of Einstein equation, is identified as

$$T_{\mu\nu} = (p+\rho)u_\mu u_\nu + pg_{\mu\nu} \tag{1.1.7}$$

where ρ is the total energy density and p is total pressure of all components.

From eqs. (1.1.1), (1.1.4), and (1.1.7), we obtain equations which describe how the cosmic scale factor $a(t)$ evolves:

$$\left(\frac{\dot{a}}{a}\right)^2 = \frac{8\pi G\rho}{3c^2} - \frac{Kc^2}{a^2}, \tag{1.1.8}$$

$$\frac{\ddot{a}}{a} = -\frac{4\pi G}{3c^2}(\rho + 3p). \tag{1.1.9}$$

Equation (1.1.8) is called Friedmann Equation.

From (1.1.8) and (1.1.9), we derive the fluid equation

$$\dot{\rho} = -3\frac{\dot{a}}{a}(\rho + p). \tag{1.1.10}$$

Note that we have only two independent equations (1.1.8) and (1.1.9) (or (1.1.8) and (1.1.10)), while there are three variables $a(t)$, ρ, and p. Therefore, we need another independent equation, which is the equation of state $p = p(\rho)$.

We consider the universe filled of radiation, matter, and cosmological constant (denoted by 'r', 'm', 'Λ' respectively). The state equations of each component are

$$\begin{cases} p_r = \dfrac{1}{3}\rho_r \\ p_m = 0 \\ p_\Lambda = -\rho_\Lambda \end{cases} \tag{1.1.11}$$

and they satisfy $\rho = \rho_r + \rho_m + \rho_\Lambda$.

The fluid equation (1.1.10) and state equation (1.1.11) gives the relation $\rho = \rho(a)$ for each component: $\rho_r \propto a^{-4}$, $\rho_m \propto a^{-3}$, and $\rho_\Lambda \propto a^0$.

To integrate the Friedman equation (1.1.8) to obtain the evolution of $a(t)$, we need suitable boundary conditions. The boundary conditions may be taken to be the value of a_0 and $\dot{a}_0$ where index 0 represents "today". However, it is conventional to set $a_0 = 1$ and specify Hubble constant

$$H_0 \equiv \left(\frac{\dot{a}}{a}\right)_0 \tag{1.1.12}$$

instead of $\dot{a}_0$. Hubble constant represents the expansion rate today, and is convenient for connecting to observations of the local Universe. Hubble constant is often normalized as $H_0 = 100h$ km s^{-1}Mpc^{-1}.

Using the Hubble constant, we can define the critical density, which is the mean density of today in the Universe corresponding to $K = 0$:

$$\rho_c = \frac{3c^2 H_0^2}{8\pi G}. \tag{1.1.13}$$

Then we rewrite the components ρ_r, ρ_m, ρ_Λ in the unit of the critical density

$$\begin{cases} \Omega_r \equiv \dfrac{\rho_{r0}}{\rho_c} \\ \Omega_m \equiv \dfrac{\rho_{m0}}{\rho_c} \\ \Omega_\Lambda \equiv \dfrac{\rho_\Lambda}{\rho_c} \end{cases} . \tag{1.1.14}$$

From (1.1.8), (1.1.12), (1.1.13) and (1.1.14), curvature K is understood to be determined by density parameters

$$K = \frac{H_0^2}{c^2}(\Omega_m + \Omega_r + \Omega_\Lambda - 1). \tag{1.1.15}$$

This equation connects the curvature of space-time and the total amount of energy.

Friedman equation (1.1.8) can be rewritten using cosmological parameters Ω_r, Ω_m, Ω_Λ, and H_0 without including K:

$$H^2 = H_0^2 \left(\frac{\Omega_r}{a^4} + \frac{\Omega_m}{a^3} + \frac{\Omega_m + \Omega_r + \Omega_\Lambda - 1}{a^2 H_0^2} + \Omega_\Lambda \right). \tag{1.1.16}$$

It can be found from the right-hand side that the different form of matter influence the dynamics of the universe at different epochs. In some cases, we can obtain the analytical solutions for $a(t)$.

(i) The radiation dominated universe: $\Omega_r = 1$

This situation is realized in the early universe and the Friedman equation is reduced to

$$\dot{a}^2 = \frac{H_0^2}{a_2} \Omega_r^{1/2} \tag{1.1.17}$$

and the solution is given by

$$a(t) = \sqrt{2H_0} \Omega^{1/4} \sqrt{t}. \tag{1.1.18}$$

(ii) The matter and radiation dominated but $K = 0$ **and** $\Omega_\Lambda = 0$

As the universe evolves, the matter density will catch up with the radiation density, because $\rho_r \propto a^{-4}$ and $\rho_m \propto a^{-3}$. The equality of matter and radiation occurs at $t = t_{\rm eq}$ with

$$\Omega_m \left(\frac{a_0^4}{a_{\rm eq}^4} \right) = \Omega_r \left(\frac{a_0^3}{a_{\rm eq}^3} \right) \tag{1.1.19}$$

$$\frac{a_0}{a_{\rm eq}} = \frac{\Omega_{\rm m}}{\Omega_{\rm r}} \cong 3.9 \times 10^4 (\Omega_{\rm m} h^2). \tag{1.1.20}$$

The Friedman equation becomes

$$H^2 = H_0^2 \left(\frac{\Omega_r}{a^4} + \frac{\Omega_m}{a^3} \right) \tag{1.1.21}$$

and the solution is given by

$$H_{\rm eq} t = \frac{2\sqrt{2}}{3} \left[\left(\frac{a}{a_{\rm eq}} - 2 \right) \left(\frac{a}{a_{\rm eq}} + 1 \right)^{1/2} + 2 \right] \tag{1.1.22}$$

where

$$H_{\rm eq}^2 \equiv 2H_0^2 \Omega_{\rm r} \left(\frac{a_0}{a_{\rm eq}} \right)^4 = 2H_0^2 \Omega_{\rm m} \left(\frac{a_0}{a_{\rm eq}} \right)^3. \tag{1.1.23}$$

In the limiting case of $t_{\rm eq} \ll t$ (matter dominated), we find

$$a(t) = \left(\frac{3}{2} H_0 \sqrt{\Omega_m} t \right)^{2/3}. \tag{1.1.24}$$

(iii) Cosmological constant dominated universe: $\Omega_\Lambda \neq 0$

If $\Omega_\Lambda > 0$ exists, eventually it will dominate other components at sufficiently large time, with

$$\dot{a}^2 = H_0^2 \Omega_\Lambda a^2 \tag{1.1.25}$$

The solution is given by

$$a(t) = C \exp\left[\sqrt{\frac{\Lambda}{3}} ct\right]. \tag{1.1.26}$$

In the absence of Ω_Λ, the expansion decelerates as we saw above. Generally, the equation of state is expressed by the parametrization $p = w\rho$, and the accelerated expansion happens when $w < -\frac{1}{3}$, which is called dark energy.

We must define some quantities which are related to our observations. In an expanding universe, the wavelength of light emitted from a distant object will be elongated. Redshift is defined as the shift in the wavelength of the light divided by the rest wavelength:

$$z \equiv \frac{\lambda_{\rm obs} - \lambda_{\rm rest}}{\lambda_{\rm rest}}. \tag{1.1.27}$$

Because the light travels following null geodesics $ds^2 = 0$,

$$ds^2 = 0 = -c^2 dt^2 + a(t)^2 d\chi^2 \tag{1.1.28}$$

Let us assume that light is emitted at $\chi = \chi_{\rm e}$ during $[t_{\rm e},\, t_{\rm e} + \delta t_{\rm e}]$, and observed at $\chi = 0$ during $[t_{\rm o},\, t_{\rm o} + \delta t_{\rm o}]$. Integrating equation (1.1.28) for the photon emitted at the moment of $t_{\rm e}$ and $t_{\rm e} + \delta t_{\rm e}$ (and observed at $t_{\rm o}$ and $t_{\rm o} + \delta t_{\rm o}$ respectively), we obtain

$$\int_{t_{\rm e}}^{t_{\rm o}} \frac{c}{a(t)} dt = \int_0^{\chi_{\rm e}} d\chi \tag{1.1.29}$$

and

$$\int_{t_{\rm e}+\delta t_{\rm e}}^{t_{\rm o}+\delta t_0} \frac{c}{a(t)} dt = \int_0^{\chi_{\rm e}} d\chi, \tag{1.1.30}$$

therefore,

$$\int_{t_{\rm o}}^{t_o+\delta t_{\rm o}} \frac{c}{a(t)} dt = \int_{t_{\rm e}}^{t_{\rm e}+\delta t_{\rm e}} \frac{c}{a(t)} dt. \tag{1.1.31}$$

Because $\delta t_{\rm e}$ and $\delta t_{\rm o}$ are small,

$$\frac{c}{a(t_{\rm o})} \delta t_{\rm o} = \frac{c}{a(t_{\rm o})} \delta t_{\rm e}. \tag{1.1.32}$$

Using the relation between the time interval and wavelength $\delta t_{\rm o} = \lambda_o / c$ and $\delta t_{\rm e} = \lambda_e / c$, we find

$$\frac{\lambda_{\rm o}}{\lambda_{\rm e}} = \frac{a(t_{\rm o})}{a(t_{\rm e})}. \tag{1.1.33}$$

From equations (1.1.27) and (1.1.33), the observable z and scale factor a when light was emitted is related:

$$1 + z = \frac{1}{a(t)}. \tag{1.1.34}$$

There are some different definitions of distance in an expanding universe. The luminosity distance d_L is defined by observed energy flux F and bolometric luminosity of an object L:

$$d_L = \left(\frac{L}{4\pi F}\right)^{\frac{1}{2}}. \tag{1.1.35}$$

Considering the total energy L distributed to the spherical shell with a radius of $S_K(\chi)$, we find

$$F = \frac{L}{4\pi S_K(\chi)^2(1+z)^2} \tag{1.1.36}$$

where $(1+z)^2$ means the loss of photon energy and change of time separation caused by cosmic expansion. Then we obtain

$$d_L = (1+z)S_K\left(\chi(z)\right) \tag{1.1.37}$$

The angular diameter distance is defined by observed separation $\Delta\theta$ and physical length D of an object:

$$d_A = \frac{D}{\Delta\theta}. \tag{1.1.38}$$

Because the observed angle $\Delta\theta$ is determined when the light is emitted at redshift z, we find

$$\Delta\theta = \frac{D}{S_K(\chi)a(z)}. \tag{1.1.39}$$

Then

$$d_A = \frac{S_K\left(\chi(z)\right)}{1+z}. \tag{1.1.40}$$

Especially in the case of flat universe,

$$d_L = (1+z)\chi(z) \tag{1.1.41}$$

$$d_A = \frac{\chi(z)}{1+z}. \tag{1.1.42}$$

These quantities $d_L(z)$ and $d_A(z)$ as a function of redshift represent the history of cosmic expansion and are dependent of cosmological parameters. Therefore, measuring $d_L(z)$ and

$d_A(z)$ at various redshifts puts constraints on these parameters. In these studies, we need an object whose luminosity L or physical size D is known, which are called "standard candle" or "standard ruler". Type Ia supernova can be used as a standard candle, while the characteristic scale seen in the galaxy redshift survey oand cosmic microwave background (CMB) serves as standard rulers. These observations have been carried out, revealing that our Universe currently undergoes an accelerated expansion, which may be attributed to an unknown form of energy with negative pressure, or the breakdown of General Relativity. In the next section, we review these observations.

1.2 Observational Probes of the Expanding Universe

1.2.1 Type Ia supernovae

As we saw in the previous subsection, the cosmic expansion should decelerate in the absence of Ω_Λ. However, in the late 1990s, two independent projects, which observed distant type Ia supernovae, obtained results suggesting that the expansion of the universe is accelerating.

Supernovae are classified by the presence or absence of typical features of their spectrum. Type Ia supernovae do not show an absorption line of hydrogen but exhibit SiII absorption feature (Filippenko 1997). There are two models explaining the formation of type Ia supernovae: single degenerate model and double degenerate model. In the former model, a white dwarf accretes material from a non-degenerate companion star and exceeds the Chandrasekhar mass limit of $\sim 1.4 M_\odot$, while the latter model involves the merger of two white dwarfs. Both of these two channels seems to be necessary to explain the observed diversity of type Ia supernovae (see Maoz & Mannucci 2012 and Wang & Han 2012 for a review) A favorable property of type Ia supernovae is that the luminosity and the decaying time scale are correlated. By observing the time variation of the luminosity, the absolute magnitude can be estimated, and combined with the observed magnitude and redshift, this gives the measured distance as a function of redshift $d_{\rm L}(z)$. Figure 1.1 is the Hubble diagram of type Ia supernovae from the two Nobel prize-winning programs, the Supernova Cosmology Project (Perlmutter et al. 1999) and the High-z Supernova Search Team (Riess et al. 1998). Distant ($z > 0.3$) supernovae become dimmer than they would be in the universe without Ω_Λ, implying the necessity of Ω_Λ and that the expansion is accelerating since $z \sim 0.5$.

We expect more stringent constraints coming from even large supernova surveys (Pan-

Staars; Kaiser et al. 2002, LSST; LSST Science Collaboration 2009) or a deeper survey which utilizes the magnification of strong lensing effect (Hubble Frontier Field; Coe et al. (2015)), although we need to better control the uncertainty, such as flux calibration error and corrections of dust extinction. Also, gamma ray burst (GRB) might be used to probe further distant Universe (Schaefer 2007), but the physical origin is even elusive so far.

1.2.2 The Anisotropy of Cosmic Microwave Background Radiation

Other independent observations also showed that there is non-zero component of Ω_Λ. Currently the stringent constraint on the cosmological parameters comes mainly from Cosmic microwave background (CMB) and baryon acoustic oscillation (BAO) in the large-scale structure of galaxies.

Cosmic Microwave Background was originally discovered in the midst of 1960s by Penzias and Wilson. This discovery was accidental because they originally intended to investigate the origin of unknown noise source found at a radio telescope, but following space and ground-based CMB experiments (COBE;Bennett et al. 1996, WMAP;Komatsu et al. 2011) have confirmed that our universe is filled almost uniformly with thermal black body radiation at the temperature of 2.7K. The tiny residual anisotropies of CMB shows a very specific pattern, encoding a lot of cosmological information.

Figure 1.2 and 1.3 is the most recent temperature map and angular power spectrum of CMB obtained by PLANCK space experiment. The horizontal axis is the angular scale $l = 180/\theta$ [deg^{-1}] and vertical axis shows the amplitude of the correlation of the intensity at the angle separation of θ [deg]. In greater l (small scale), the smearing of the power spectrum is seen. This is a result of the diffusion of photons due to an increased mean free path after recombination, called diffusion damping (Silk damping; Silk 1968). The magnitude and scale of this effect is mainly determined by the mean free path of photon traveling soon after the recombination, the baryon density Ω_b can be well determined. The peak at $k \sim 200$ shows the Baryon Acoustic Oscillation. This scale and amplitude is sensitive to Ω_m and Ω_b. The large scale is subject to the effect of the time-variance of gravitational potential. In the matter dominated universe, the fluctuation of gravitational potential $\delta\Phi \sim G\delta M/R$ stays constant, because both of the density fluctuation δM and R are proportional to $a(t)$. The radiation and dark energy slow down the evolution of gravitational potential, especially just

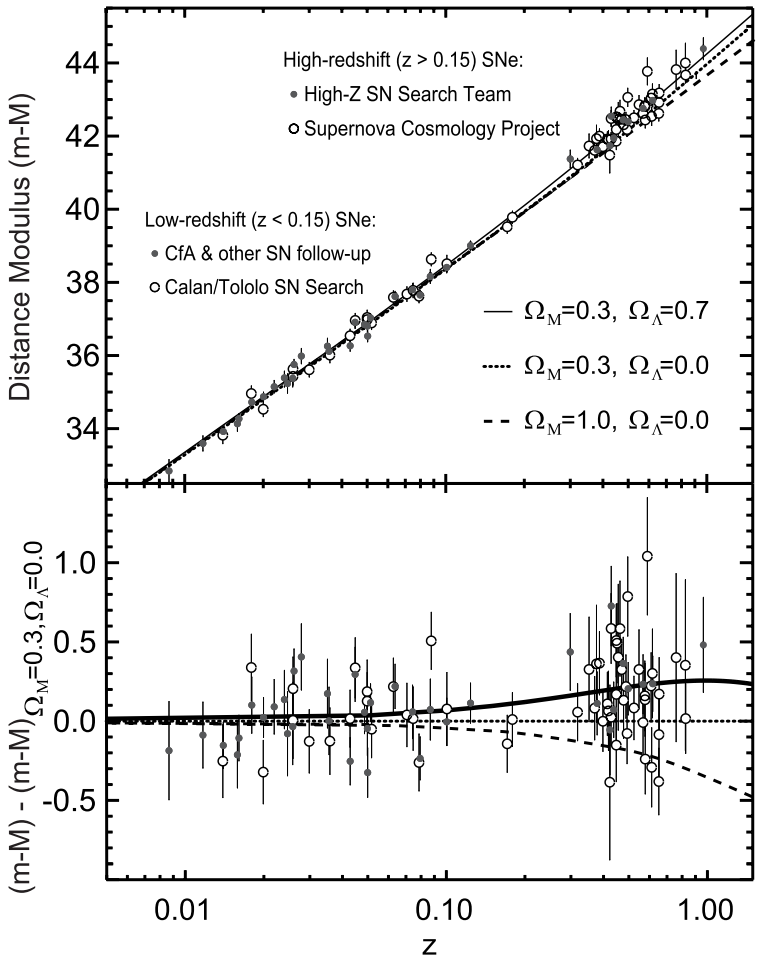

Figure 1.1: (Top) Hubble diagram of Type Ia SNe. The distance is indicated by distance modulus $m-M$ where m and M is apparent and absolute magnitudes respectively. (Bottom) The discrepancy of distance modulus as a function of redshift compared to that of a universe without cosmological constant. From Frieman & Huterer (2008).

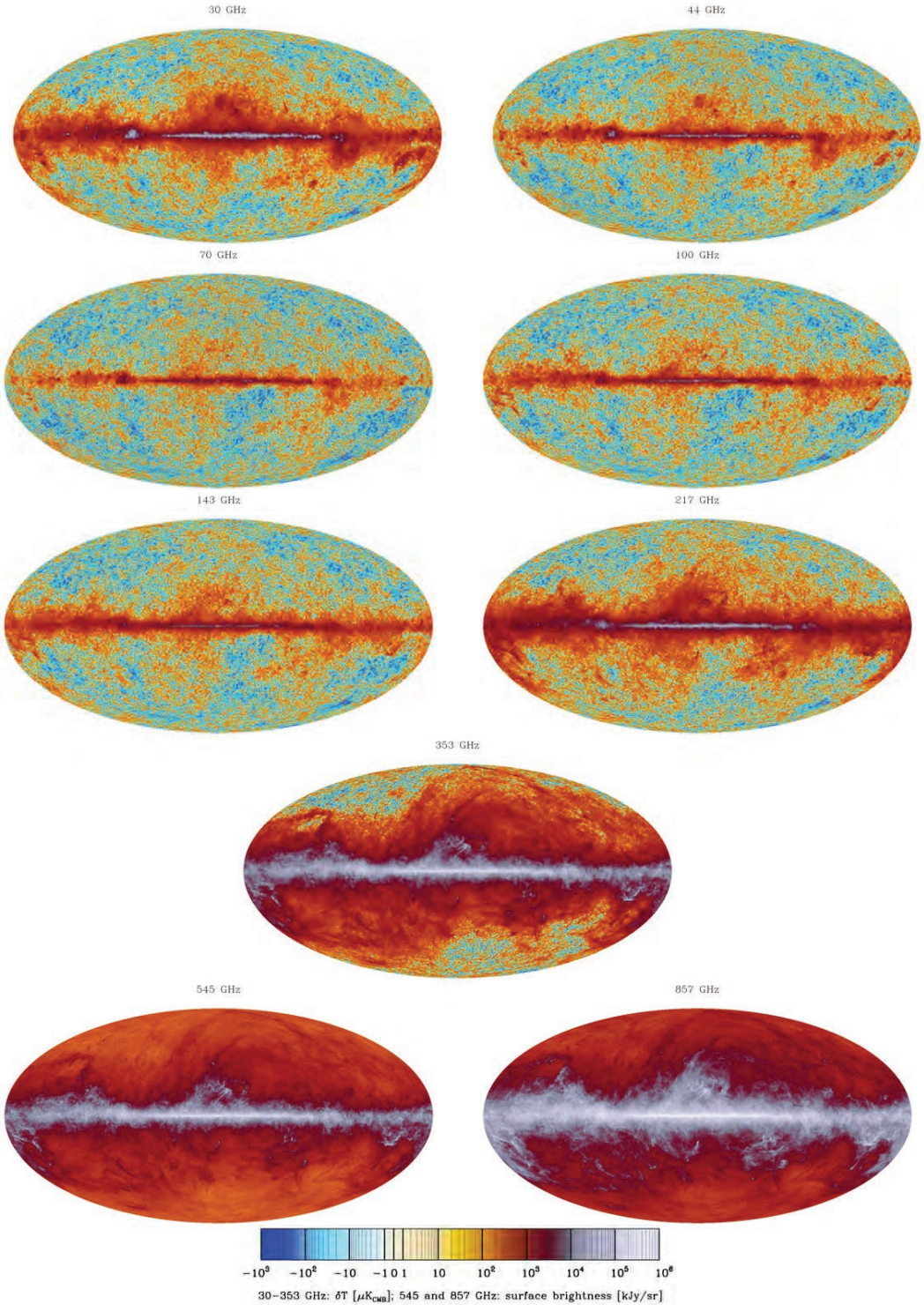

Figure 1.2: The nine Planck frequency maps. From Planck Collaboration et al. (2014).

after the recombination and the late-time. Photons from the last scattering surface change their own energy during passing through the changing gravitational potential, imprinting the horizon scale of recombination and recent universe on the angular power spectrum. This effect is called early and late integrated Sachs Wolfe effect (ISW; Sachs & Wolfe 1967), encoding the information of $\Omega_{\rm m}$ and Ω_Λ respectively.

Many cosmological parameters can be measured simultaneously by CMB observation by fitting the power spectra with cosmological models. although it is less powerful in constraining K and Ω_Λ because they have a similar effect on CMB anisotropy, i.e., change the apparent angular separation on the whole. According to the latest cosmological results presented by Planck Collaboration et al. (2015), Ω_Λ is estimated to be 0.6911 ± 0.0062.

Recently, the polarization of CMB is also actively probed as a new powerful way to put constraints on cosmological parameters. The small-scale B-mode induced by gravitational lensing has been detected by the cross-correlation between SPTpol experiment (Austermann et al. 2012) and Herschel cosmic infrared background (CIB) map (Pilbratt et al. 2010) by Hanson et al. 2013. A detection of the large-scale B-mode that would be created by the primordial gravitational wave, which should appear in some models of inflation, is reported by BICEP2 experiment (BICEP2 Collaboration et al. 2014), though systematics is being pointed out. Currently, POLARBEAR experiment (The Polarbear Collaboration: P. A. R. Ade et al. 2014) and LiteBIRD experiment (Matsumura et al. 2014) is ongoing to detect the large-scale B-mode with an improved accuracy.

1.2.3 Baryon Acoustic Oscillations

Before recombination ($z \sim 1100$), baryons and photons were so tightly coupled via Thomson scattering that the baryon-photon system behaved as a single fluid, creating pressure. In a overdense region containing dark matter, baryons, and photons, the pressure creates a sound wave of baryons and photons with a velocity of

$$c_s = \frac{c}{\sqrt{3}} \left(1 + \frac{3\Omega_b}{4\Omega_\gamma}\right)^{-\frac{1}{2}}. \tag{1.2.1}$$

Baryons and photons moved outwards together, while dark matter stayed in the central overdense region. After recombination time $t_{\rm rec}$, photon and baryons no longer interact with each other, leaving the baryonic structure with a radius of

$$r_s(t) \equiv \int_0^{t_{\rm rec}} \frac{c_s}{a} dt. \tag{1.2.2}$$

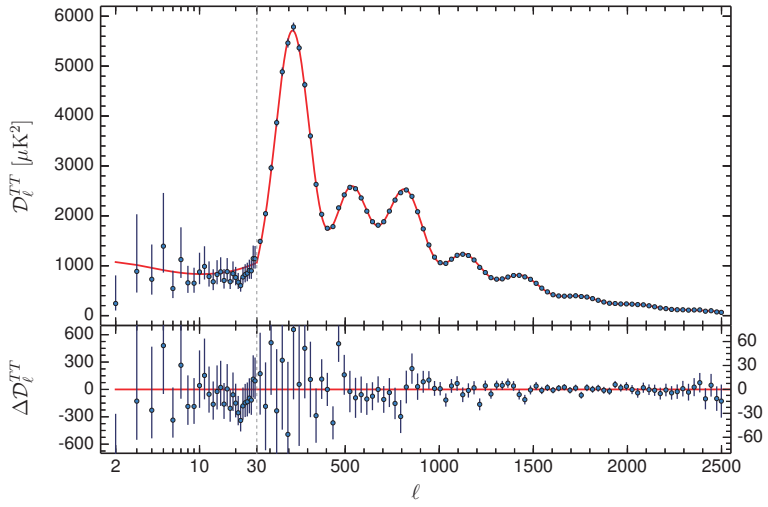

Figure 1.3: The angular power spectra of CMB temperature fluctuation obtained from Planck experiment (Planck Collaboration et al. 2015). The error bars show $\pm 1\sigma$ uncertainties. The solid line of the top panel is based on the best-fit ΛCDM model and the bottom panel shows the residuals.

This radius is called sound horizon.

The sound horizon scale r_s is $\sim$ 150Mpc in comoving, serving as a standard ruler. This feature at $\sim$ 150Mpc can be detected in the statistics of galaxies such as correlation function and power spectrum. The correlation function is defined as the covariance of overdensities at separation $r_{12} \equiv |\boldsymbol{r}_1 - \boldsymbol{r}_2|$

$$\xi(r_{12}) \equiv \langle \delta(\boldsymbol{r}_1)\delta(\boldsymbol{r}_2)\rangle. \tag{1.2.3}$$

Here overdensity $\delta(x)$ is defined by

$$\delta(\boldsymbol{r}) = \frac{\rho(\boldsymbol{r}) - \overline{\rho}}{\overline{\rho}} \tag{1.2.4}$$

where $\overline{\rho}$ is the mean number density and $\rho(\boldsymbol{r})$ is the density of galaxies at position r.

Equation (1.2.3) is expressed by the density field $\rho(\boldsymbol{r})$

$$\langle \rho(\boldsymbol{r}_1)\rho(\boldsymbol{r}_2)\rangle = \overline{\rho}^2(1 + \xi(r_{12})) \tag{1.2.5}$$

and it is understood that $\xi(r)$ gives a fractional excess of probabilities of finding galaxy pairs with separation of r.

In practice, the correlation function is derived from the 3-dimensional galaxy catalog by

$$\xi(r) = \frac{DD - 2DR + RR}{RR} \tag{1.2.6}$$

where DD is the number of pairs of galaxies at the distance of $[r, r+\Delta r]$, DR is the number of pairs between galaxies and random catalog which have the same number density as galaxies but no structures, and RR is the number of pairs of random catalog (Landy & Szalay 1993) Figure 1.4 shows the correlation function of luminous red galaxies (LRGs) of Sloan Digital Sky Survey (SDSS) (Eisenstein et al. 2005). We can see a clear bump at ~ 100 Mpc.

Many surveys have detected BAO signature (2dF;Cole et al. 2005, SDSS;Eisenstein et al. 2005, WiggleZ;Blake et al. 2011b, 6dF;Beutler et al. 2011, BOSS;Anderson et al. 2012) and ΛCDM model gives the best description of these data. Larger surveys are being planned such as PFS (Takada et al. 2014) and DESI (Levi et al. 2013) to measure BAO with even smaller uncertainties. BAO is considered to be one of the most promising probe of the nature of dark energy, because the intrinsic BAO scale is robust, determined by CMB experiments.

1.2.4 Redshift Space Distortions and FastSound project

While many observational results show that the universe is undergoing an accelerating expansion, the origin of this unexpected acceleration remains one of the greatest problems in physics and astronomy. It may be a result of an exotic form of energy with negative pressure, Λ being one example, but the problems of its smallness and fine tuning still remain unsolved. Another possibility of the accelerated expansion, i.e., modified gravity, has been proposed by many authors (e.g., DGP:Dvali et al. 2000, $f(R)$:Hu & Sawicki 2007). These models predict the same expansion history as that of the ΛCDM model, but different dynamical evolution of the universe. The growth rate of the large-scale structure, $f(z)$, varies according to the theory of gravity, which is well approximated by $f(z) \sim \Omega_m(z)^\gamma$ where γ is referred to as the growth index parameter and Ω_m is the dimensionless matter density (Linder 2005). Therefore, the measurement of f gives an alternative test of gravity theories, which complements the geometry test such as CMB and BAO.

Redshift space distortion (RSD) observed by a galaxy redshift survey is a powerful way for measuring the growth rate of the structure. Galaxy 3-D maps constructed using redshift-space distances are distorted with respect to those in real-space due to the line-of-sight component of the peculiar velocities of galaxies (see Figure 1.2.4 for a conceptual scheme). Isotropic statistics in real-space, such as the two-point correlation function or the power spectrum, develop an apparent quadrupole anisotropy in redshift space (see Figure 1.2.4), the magnitude of which is sensitive to the velocity power spectrum whose amplitude depends

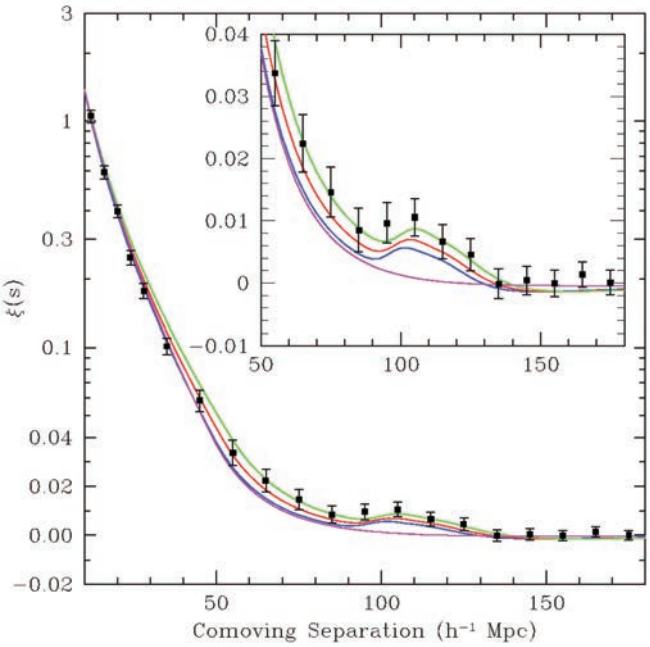

Figure 1.4: The two-point correlation function $\xi(r)$ for SDSS LRG sample. The solid lines show theoretical predictions corresponding to various values of $\Omega_m h^{-2}$. From Eisenstein et al. (2005).

on the quantity $f\sigma_8 = d\sigma_8/d(\ln a)$ where σ_8 is the rms amplitude of density fluctuations smoothed by a top-hat filter with a comoving radius of $8h^{-1}$ Mpc.

The power spectrum of large-scale structure is defined by

$$P(\boldsymbol{k}) = \langle|\delta(\boldsymbol{k})|\rangle^2 \tag{1.2.7}$$

where $\delta(k)$ is the Fourier transform of $\delta(\boldsymbol{x})$, and $\delta(\boldsymbol{x})$ is defined as the density fluctuation

$$\delta(\boldsymbol{x}) = \frac{\rho(\boldsymbol{x}) - \overline{\rho}}{\overline{\rho}}. \tag{1.2.8}$$

In real space, $P(\boldsymbol{k})$ is isotropic but the peculiar motions of galaxies along the line of sight adds an additional anisotropy. Redshift z_s and the comoving distance x is related by

$$x = \int_0^z \frac{cdz'}{H(z')}. \tag{1.2.9}$$

We measure the distance of a galaxy s, from observed redshift $z_{\rm s}$, derived from a certain feature of its emission. However, the peculiar motion of a galaxy $\boldsymbol{v}$ adds a Doppler shift component to its cosmological redshift z, resulting in the observed redshift z_s

$$z_s = z + \frac{v_3}{ca} \tag{1.2.10}$$

where 3-axis is along line-of-sight.

Substituting (1.2.10) into (1.2.9) and using a linear approximation, we find that the observed distance s_3 is shifted from its original position x_3 inferred from the pure cosmological redshift:

$$s_3 = x_3 + \frac{v_z}{aH}. \tag{1.2.11}$$

From the conservation of galaxy number in the volume elements of redshift space and real space, we get

$$n_s(\boldsymbol{s}) = J^{-1} n_x(\boldsymbol{x}) = \left[1 - \frac{\partial}{\partial x_3}\left(\frac{v_3}{aH}\right)\right] n_g(\boldsymbol{x}). \tag{1.2.12}$$

where J is the Jacobian determinant $J = |\partial \boldsymbol{s}/\partial \boldsymbol{x}|$. Taking an ensemble average of (1.2.12), we have

$$\overline{n}_s(\boldsymbol{s}) = \overline{n}_x(\boldsymbol{x}), \tag{1.2.13}$$

and with a linear approximation, we find

$$\delta_s(\boldsymbol{s}) = \delta_x(\boldsymbol{x}) - \frac{\partial}{\partial x_3}\left(\frac{v_3}{aH}\right). \tag{1.2.14}$$

If we assume that the survey area is not so large and aH is constant, (1.2.14) becomes

$$\delta_s(\boldsymbol{x}) = \delta_x(\boldsymbol{x}) - \frac{1}{aH}\partial_3 v_3(\boldsymbol{x}). \tag{1.2.15}$$

Here we replaced $\delta_s(\boldsymbol{s})$ with $\delta_s(\boldsymbol{x})$ according to linear approximation. Fourier transform of (1.2.15) is

$$\tilde{\delta}_s(\boldsymbol{k}) = \tilde{\delta}_x(\boldsymbol{k}) - \frac{ik_3}{aH}\tilde{v}_3(\boldsymbol{k}). \tag{1.2.16}$$

From the continuum equation, the velocity is related to the density:

$$v_3(\boldsymbol{k}) = aHf\frac{ik_3}{k^2}\delta(\boldsymbol{k}). \tag{1.2.17}$$

where $f = d\ln D/da$ and D is the growth factor.

With a commonly used ansatz that the overdensity of galaxy $\delta_{\rm g}$ traces that of matter δ by $\delta_{\rm g} = b\delta$, we obtain

$$\tilde{\delta}_s(\boldsymbol{k}) = (1+\beta\mu^2)\tilde{\delta}_g(\boldsymbol{k}) = b(1+\beta\mu^2)\tilde{\delta}(\boldsymbol{k}) \tag{1.2.18}$$

where $\beta = f/b$ is called anisotropy parameter and $\mu = k_3/k$ is the cosine of the vector $\boldsymbol{k}$ along the line-of-sight.

As a result, the observed power spectrum is related to the real space matter power spectrum:

$$P(k,\mu) = b^2(1+\beta\mu^2)^2 P(k) \tag{1.2.19}$$

which is called Kaiser formula (Kaiser 1987).

Because the matter power spectrum $P(k)$ is proportional to σ_8^2, the anisotropy and overall amplitude of the galaxy power spectrum gives measurements of β and $b\sigma_8$, and consequently $f\sigma_8$. This test has already been performed at $z < 1$ using data from a number of galaxy redshift surveys (Hawkins et al. 2003; Guzzo et al. 2008; Blake et al. 2011a; Samushia et al. 2013; Reid et al. 2012; Beutler et al. 2012; de la Torre et al. 2013; Beutler et al. 2014). The standard ΛCDM model is found to be consistent with the observed values of $f\sigma_8$ and its evolution as seen in Figure 1.7.

A next important step for this test is to reduce the statistical error on $f\sigma_8$ using larger galaxy surveys at $z < 1$, or to extend the $f\sigma_8$ measurements to even higher redshifts. At higher redshifts, nonlinearities on the physical scales of interest are smaller than they are today, which can result in a cleaner measurement of $f\sigma_8$. Moreover, at high redshifts, $f \sim 1$, and RSD is directly sensitive to σ_8, thus providing a baseline for lower redshifts

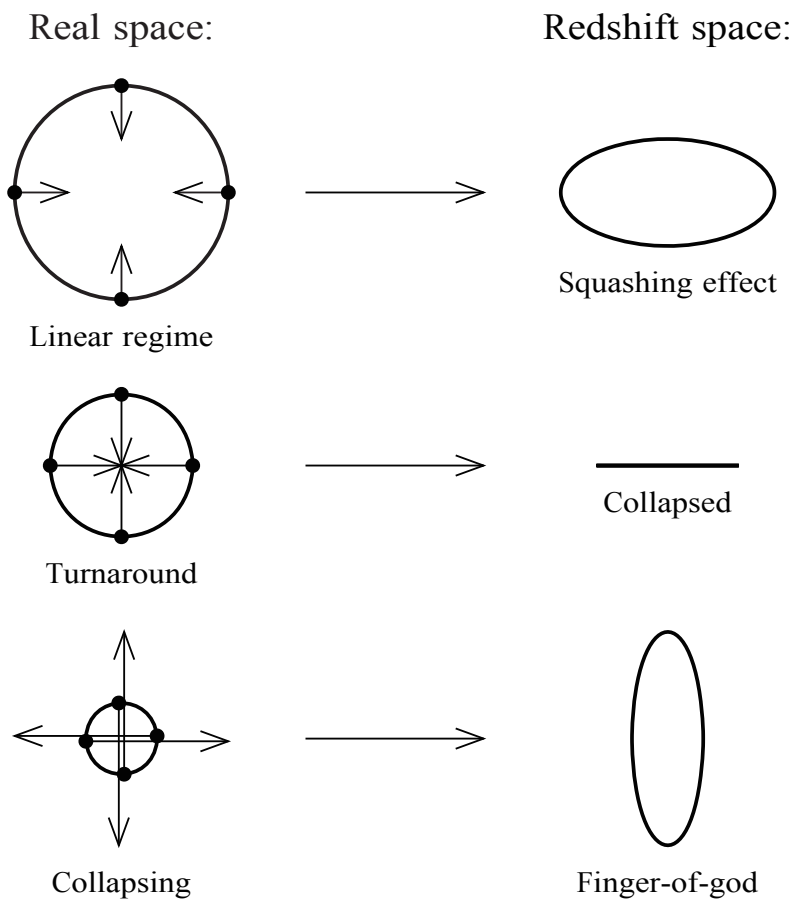

Figure 1.5: Detail of how peculiar velocities lead to the redshift distortions. The dots are galaxies undergoing infall towards a spherical overdensity, and the arrows represent their peculiar velocities. At large scales, the peculiar velocity of an infalling shell is small compared to its radius, and the shell appears squashed. At smaller scales, not only is the radius of a shell smaller, but also its peculiar infall velocity tends to be larger. The shell that is just at turnaround, its peculiar velocity just cancelling the general Hubble expansion, appears collapsed to a single velocity in redshift space. At yet smaller scales, shells that are collapsing in proper coordinates appear inside out in redshift space. The combination of collapsing shells with previously collapsed, virialized shells, gives rise to fingers-of-god. From Hamilton (1998).

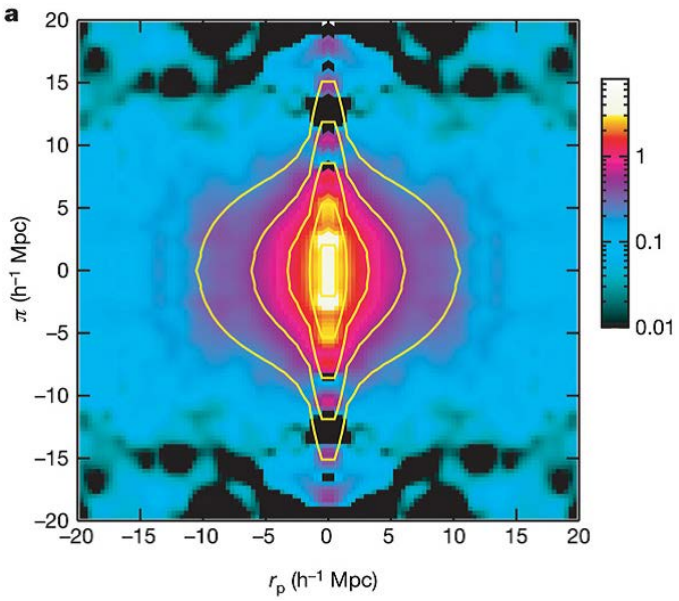

Figure 1.6: The two-point correlation function of galaxies obtained of VVDS survey. In the large scale, one can see the squash along line-of-sight while an elongation is seen in the small scale. From Guzzo et al. (2008).

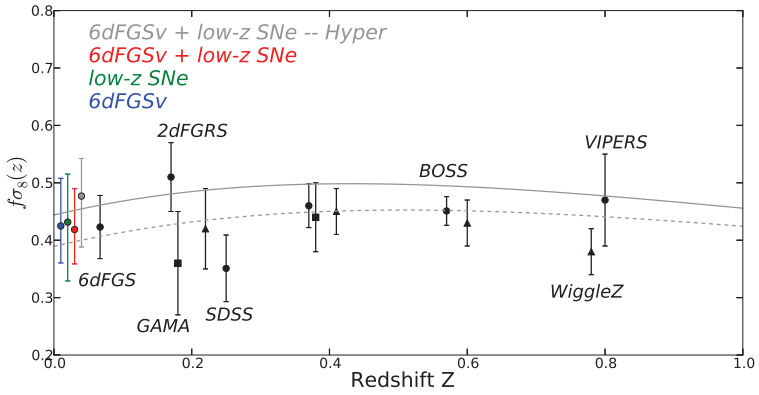

Figure 1.7: The growth rate constraints from spectroscopic redshift surveys. From Johnson et al. (2014). The solid and dashed lines shows the theoretical predictions from PLANCK and WMAP cosmology.

measurements. RSD has been detected at $z \sim 3$ using Lyman-break galaxies (Bielby et al. 2013), at the significance of $\sim 2\sigma$ level. The principal aim of the FastSound[1] galaxy redshift survey is to measure $f\sigma_8$ at $z \sim 1.18$–1.54 for the first time by detecting RSD using the near-infrared Fiber Multi-Object Spectrograph (FMOS) mounted on Subaru Telescope.

At high-redshift exceeding $z = 1$, it is necessary to use bright emission line such as Hα (6563Åin rest frame) to efficiently trace the 3D distribution of galaxies. However, this line is only accessible in the near-infrared: FMOS can access it exceeding $z = 1$. Furthermore, FMOS is equipped with OH airglow suppression (OHS) mirror optically blocking OH airglow which is bright in NIR and time-variable, being the source of noise.

The FMOS instrument has 400 fibers in a 30-arcmin diameter field-of-view, and covers the wavelength range 0.9–1.8 μm in its low-dispersion mode; for FastSound we use the higher-throughput higher dispersion mode working in the H-band and covering 1.43–1.67μm. This allows us to reach the $z > 1$ universe by detecting bright Hα λ6563 emission lines from star-forming galaxies. FMOS uses a novel fiber positioning system, called "Echidna", which is driven by a saw-tooth voltage pulse sent to the piezoelectric actuator, in order to populate 400 fibers in a limited space of 15 cm diameter. The atmospheric OH emission lines are hardware-blocked using an OH mask mirror, thus eliminating a dominant noise source in the near-infrared region.

1.3 Purpose of this thesis

The purpose of this thesis is to present the details of FastSound, including survey design, target selection, spectroscopic observation by FMOS, data reductions, catalog production, and $f\sigma_8$ measurement. We carried out a test observation of FMOS and examined for the best target selection method using CFHTLS Wide optical photometric data. We tested several selection methods, e.g., color-based selections versus photometric-redshift-based selections, and pure optical-band selections versus adding UKIDSS near-infrared bands. In parallel with the observation, we developed an software algorithm for automated emission line detection. In the case of FMOS, residual OH airglow lines just outside the OH mask regions and cosmic rays often show spectral shapes similar to those of real emission lines. Bad pixels

[1]The name is composed of two acronyms: one a Japanese name "FMOS Ankoku Sekai Tansa" (FMOS 暗黒世界探査, meaning FMOS dark Universe survey), and the other an English name "Subaru Observation for Understanding the Nature of Dark energy".

on the detectors and pixels affected by cosmic-rays were efficiently removed by using the information obtained from the FMOS analysis pipeline, and the flat-field images was used to suppress noise around the mask regions, resulting in the false detection rate of $\sim 5\%$ above $S/N = 4.5$. The FastSound observations have been completed using 35 nights from March 2012 to July 2014, covering the total survey area of 20.6 deg^2 [121 FMOS field-of-views (FoVs)]. About $4,000$ emission line galaxies were detected using the detection algorithm, and the redshift catalog was created. Using this redshift catalog, the two-point correlation function was measured and the growth rate $f\sigma_8$ was derived via RSD (Okumura et al. 2015), which is the first constraint beyond $z = 1$. In chapter 2, I present the photometric catalogs which is used for FastSound project, the study of target selection method, and final observation strategy of FastSound. The observation was described in chapter 3, followed by the data reduction of FastSound data using FMOS image reduction pipeline and the dedicated algorithm for emission line detection in chapter 4. The statistical properties of FastSound sample and production of redshift catalog are given, followed by the measurement of the two-point correlation function and $f\sigma_8$ in chapter 5. Finally, I summarize my works in chapter 6.

Chapter 2

FastSound Survey Design and Strategy

2.1 Parent Photometric Catalog

The first prerequisite for a redshift survey is the parent photometric catalog from which we select the spectroscopic target based on target selection criteria. The estimated survey field of FastSound was ~ 30 square degrees, thus we needed a photometric data set which covers more than ~ 30 deg^2. Canada-France-Hawaii Telescope Legacy Survey (CFHTLS) is an optical imaging survey with MegaCam on Canada-France-Hawaii Telescope (CFHT), composed of CFHTLS deep, CFHTLS wide, and CFHTLS very wide. Because CFHTLS Wide had a total survey area of ~ 170 deg^2 and the uniform catalog with a deep limiting magnitudes was achieved, we determined to use this CFHTLS Wide catalog. CFHTLS Wide is divided into four sub-field W1–W4 corresponding to four seasons. The location and sky coverage of each sub-field are displayed in Table 2.1. All sub-field have at least ~ 20 deg^2 and this enables us to do observation throughout the year. CFHTLS catalogs produced by MegaPipe at TERAPIX[1] were split by band and pointing, but the unified version had been created by Gwyn (2012), so we used the MAG_AUTO magnitudes of u^*, g', r', i', and z' in the z'-selected catalog of Gwyn (2012) in order to cut out the need of merging and removing the redundant sources. The limiting magnitudes of this catalog are 26.0, 26.5, 25.9, 25.7, and 24.6 respectively for 50% completeness level for point sources.

In ~ 3 deg^2 of the CFHTLS W1 field and ~ 7 deg^2 of the W4 field, near-infrared J

[1] http://terapix.iap.fr

Table 2.1: Overview of the CFHTLS Wide fields. The RA (J2000) and DEC (J2000) columns show the center of each field. Sky coverage is expressed along RA and DEC axes.

Field	RA (J2000)	DEC (J2000)	Sky coverage[deg^2]
W1	02:18:00	-07:00:00	8.5×7.5
W2	08:57:49	-03:19:00	4.8×4.7
W3	14:17:54	+54:30:31	6.7×6.6
W4	22:13:18	+01:19:00	23.3

band data were also available from the UKIDSS deep Extragalactic Survey (UKIDSS DXS: Lawrence et al. 2007) DR8, whose limiting magnitude was 22.3 (5σ, point-source). We tried to use these data to test the usefulness of adding NIR data to the selection criteria, but we finally decided not to include J data in our target selection, because there was no significant improvement by adding J band data within the statistical scatter. This will be detailed in the next subsection.

In the following sections, we use magnitudes corrected for the Galactic extinction using the $E(B-V)$ map of Schlegel et al. (1998):

$$u^* = u^* - 4.716 \times E(B-V) \tag{2.1.1}$$

$$g' = g' - 3.634 \times E(B-V) \tag{2.1.2}$$

$$r' = r' - 2.691 \times E(B-V) \tag{2.1.3}$$

$$i' = i' - 1.998 \times E(B-V) \tag{2.1.4}$$

$$z' = z' - 1.530 \times E(B-V) \tag{2.1.5}$$

$$J = J + 0.870 - 0.877 \times E(B-V). \tag{2.1.6}$$

Here, 0.870 in the J band means the conversion factor from Vega magnitudes provided in the UKIDSS catalog to AB magnitude. The extinction maps in the FastSound survey regions are displayed in Figure 2.1. The W4 field has higher extinction ($E(B-V) = 0.065$ on average) than the other fields ($E(B-V) = 0.012$–0.024 on average).

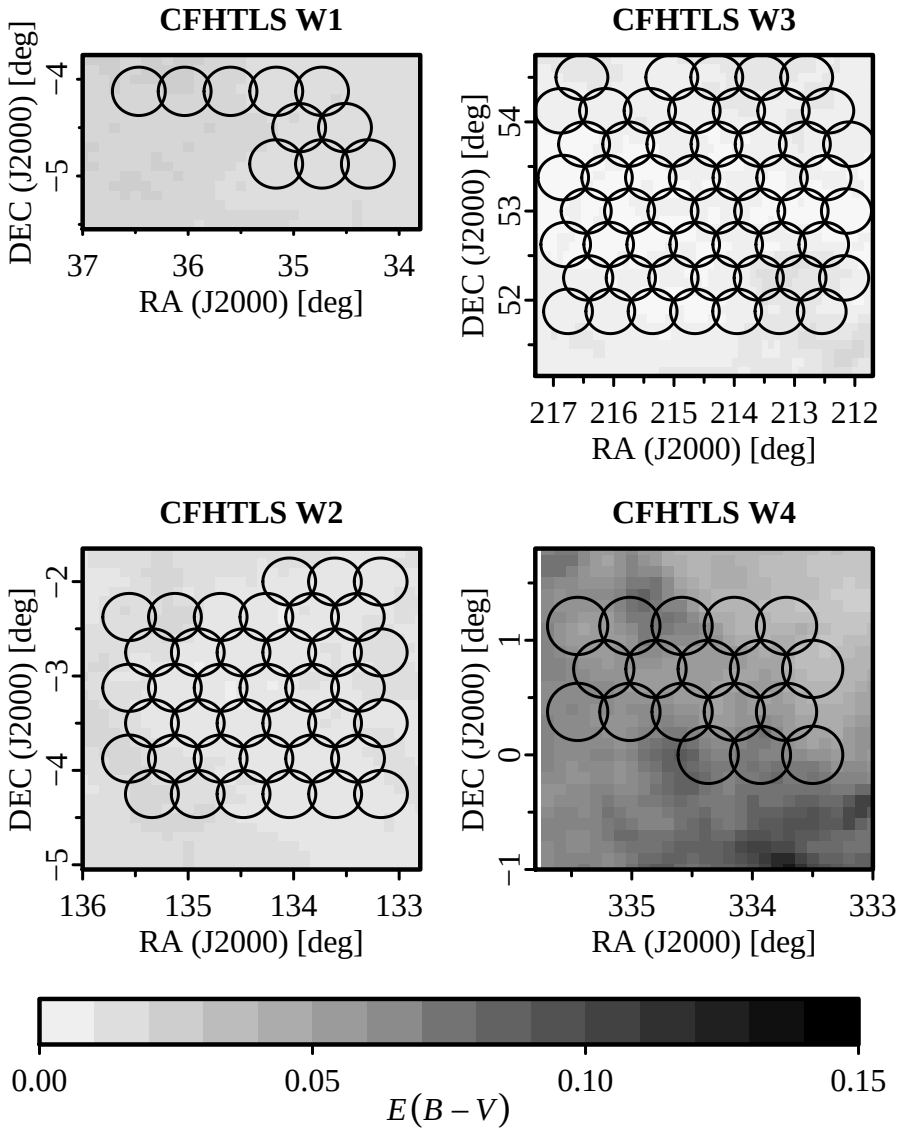

Figure 2.1: The Galactic extinction map [$E(B-V)$ from Schlegel et al. (1998)] in each of the four FastSound survey fields. The circles show the observed FoVs by the FastSound project.

2.2 A Study of Target Selection Methods

An efficient selection of target galaxies using photometric data from the parent catalog is an essential key for spectroscopic surveys. In the FastSound, we used the high-resolution (HR) mode of FMOS, whose wavelength coverage and detection limit were 1.43–1.68 μm and $\sim 2 \times 10^{-16}$ erg cm^{-2}s^{-1}. Our target was Hα emitting galaxies (λ6563 in the rest frame), which are more detectable than continuum light in the distant universe, hence we must efficiently select target galaxies at $z \sim 1.18$–1.54 which possess bright Hα line detectable by FMOS.

To finalize the target selection method for FastSound, we carried out test observations using FMOS in September/October, 2011, where we tested several selection methods, e.g., color-based selections versus photometricredshift- based selections, and pure optical-band selections versus adding near-infrared bands. In this section, I will show the tested selection method, the pilot observation, and its results.

2.2.1 Color-based Selection

The first simple method that we test is a selection by galaxy colors. We empirically determined the color selection criteria to select galaxies whose Hα fluxes are expected to be strong, based on Hα flux estimates from SED fittings and photometric redshift calculations using deep optical+NIR photometry of galaxies in the Subaru deep Field and the Subaru XMM-Newton deep Field (Sumiyoshi et al. 2009). For this observational study we test the following color selection criteria. In the case of selection using only optical photometry of CFHTLS wide, we adopt: $0.0 < (r' - z') - 1.4(g' - r') < 0.8$, $0 < g' - r' < 0.6$, $(i' - z') - 0.6(g' - i') > -0.1$. These conditions are shown in color-color diagrams of Figure 2.2. In addition to these color conditions, we also adopt a magnitude range of $22.0 < g' < 23.8$, which is empirically determined from past FMOS observations. In this figure the galaxies are color-coded according to photometric redshifts described in §2.2.2. Approximately one third of galaxies with $z_{\rm ph} = 1.2$–1.5 that we want to observe are populated in the regions of the above conditions, while more than 90% of the galaxies outside this redshift range are rejected. We varied the magnitude thresholds of z' in a range of $z \sim 22.6$–23.0 so that $\sim$400 target galaxies are available for a FoV (see Table 2.2 for values in each field).

For the test of color selection using the NIR J band, we further added a condition of $i' - J > 0.5$, to account for the redshifted 4000 Å break falling between i' and J. However,

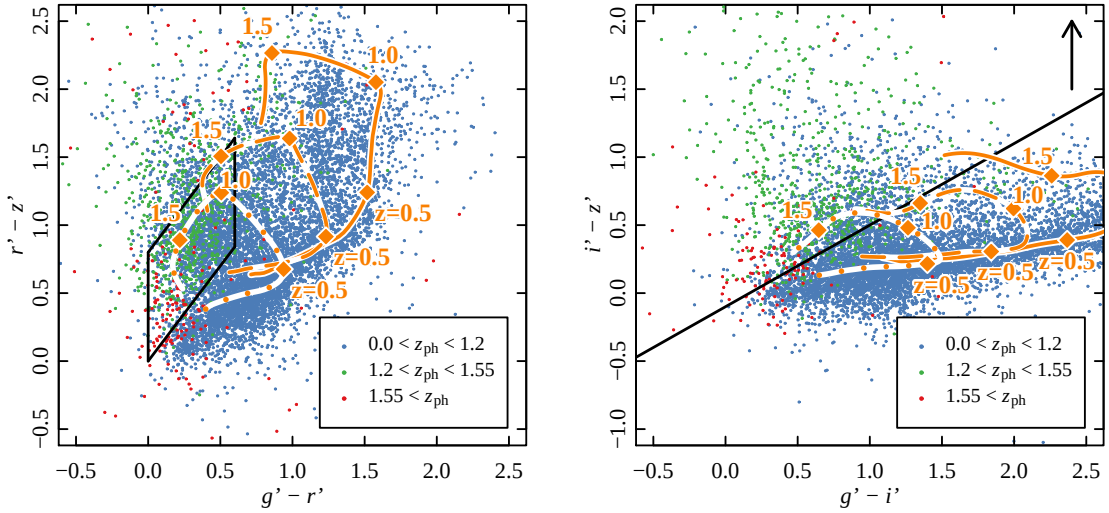

Figure 2.2: CFHTLS wide galaxies on the $g'r'z'$ and $g'i'z$ diagrams. The plots are color-coded according to the photometric redshifts, as indicated in the legend. The black lines indicate the color selection criteria of $0.0 < (r'-z') - 1.4(g'-r') < 0.8$, $0.0 < g'-r' < 0.6$, and $(i'-z') - 0.6(g'-i') > -0.1$. Magenta lines show the color tracks of unreddened elliptical galaxies (dotted), Sbc galaxies (dashed), and Scd galaxies (solid) at $0.0 < z < 2.0$. These expected colors are based on SEDs from Coleman et al. (1980).

we found that this condition was too strong to retain ~ 400 targets in the FMOS FoV for the W4 field, and hence the condition was relaxed to $i' - J > 0.0$.

2.2.2 Photo$z$-based Selection

The second method we tested is based on photometric redshift estimates and Hα flux estimates from SED fitting. For galaxies brighter than $i' = 24$, the CFHTLS T0006 official photometric redshifts are available (Ilbert et al. 2006, Coupon et al. 2009), and we use these. The redshift accuracy $\sigma_{\Delta z/(1+z_s)} \equiv 1.48 \times \mathrm{median}(|\Delta z|/(1+z_s))$ is around 0.035 at $i' < 21.5$, 0.042 at $21.5 < i' < 22.5$, and 0.070 at $22.5 < i' < 23.5$. However, no photometric redshift estimate is provided for galaxies fainter than $i' = 24$ due to the poor reliability estimates of the photometry. Here, since we wished to increase the chance of observing $z > 1$ galaxies, we computed photometric redshifts for galaxies at $i' > 24$ by ourselves using the public code *LePhare* (Arnouts et al. 1999, Ilbert et al. 2006) according to the description of Coupon

et al. (2009). This code computes the best fit SED through a χ^2 minimization procedure by comparing theoretical magnitudes obtained from SED templates or SED models to observed magnitudes. Another commonly used code is *Hyperz* (Bolzonella et al. 2000), but this code does not support the zero-point calibration, so we used *LePhare* for our photo-z calculations. When a galaxy is not detected in one of the band filters, the band was simply not used in the photo-z calculation.

Photometric zero-point calibration using galaxies with known spectroscopic redshifts is important for the accuracy of photometric redshift calculation. Since the spectroscopic data of the VVDS (VIMOS-VLT Deep Survey: Febre et al. 2005; Garilli et al. 2008)[2] deep and wide survey data are available on the area of CFHTLS W1 and W4 respectively, we used them to perform the zero-point calibration of CFHTLS wide photometry, although they are outside the redshift range of our survey. The VVDS survey depths are $17.5 \leq I_{AB} \leq 24.0$ for VVDS deep and $17.5 \leq I_{AB} \leq 22.5$ for VVDS wide. We used galaxies with flags of 2–4 ($\sim$ 80–99% secure redshifts), 9 (one secure spectral feature in emission), 12–14, or 19 (similar to 2–4, 9 but flags for broad line AGNs) for both VVDS deep and wide to assure secure redshift determination. Galaxies from VVDS deep and wide public data with z' magnitudes brighter than 23.0 are matched with CFHTLS W1 and CFHTLS W4, respectively, and used for the derivation of photometric calibrations. The sample sizes of VVDS-CFHTLS are 5,054 (CFHTLS W1) and 8,445 (W4), and the redshift medians are 0.69 and 0.56, respectively.

These photometric redshifts are based on empirical SED templates of Ell, Sbc, Scd, Irr (CWW; Coleman et al. 1980), 60 interpolated SEDs from CWW, and two starbursts from Kinney et al. (1996). Hα fluxes cannot be estimated simply from these results, because the empirical templates do not include any details on the physical galaxy properties such as stellar mass or star formation rate. Therefore, we further performed fitting with theoretical SED templates from PEGASE2 (Fioc 1999), Scalo IMF (Scalo 1986) and solar abundance, fixing the redshifts at those estimated using the empirical SED templates. We use 13 models of exponentially declining star formation histories with the exponential time scales ranging 0.1–20 Gyr, and a constant SFR model. The dust extinction is taken into account assuming the Calzetti law (Calzetti et al. 2000) in the range of $E(B-V) = 0$–0.35. Then we calculate the intrinsic Hα flux from SFR by the conversion factor which is based on Kennicutt (1998) and of which the offset is calibrated using SDSS galaxies (Brinchmann et al. 2004, Sumiyoshi et al. 2009).

[2]http://cesam.oamp.fr/vvdspub/

$$\begin{aligned}\log\left(L_{\mathrm{H}\alpha}/[\mathrm{erg/s}]\right) &= 40.93 + \log\left(\mathrm{SFR}/[\mathrm{M}_\odot/\mathrm{yr}]\right) \\ &\quad -0.4A_{\mathrm{H}\alpha}. \end{aligned} \tag{2.2.1}$$

The conversion factor 40.93 was derived by comparing the spectroscopic Hα line luminosities of the SDSS galaxies with those estimated by photometric fittings, using the method of Sumiyoshi et al. (2009). The value is different from that of Kennicutt (1998) and Sumiyoshi et al. (2009), because of the use of the Scalo IMF rather than the Salpeter IMF.

An extinction A at a wavelength λ is related to the color excess:

$$A_\lambda = k(\lambda)E(B-V). \tag{2.2.2}$$

where $k(\lambda)$ is an extinction curve.

The most common extinction curve for high-redshift star-burst galaxies is the law empirically derived by Calzetti et al. (2000):

$$k(\lambda) = \begin{cases} 2.659\left(-2.156 + \frac{1.509}{\lambda} - \frac{0.198}{\lambda^2} + \frac{0.011}{\lambda^3}\right) + R_V & (0.12\mu\mathrm{m} \leq \lambda \leq 0.63\mu\mathrm{m}) \\ 2.659\left(-1.857 + \frac{1.040}{\lambda}\right) + R_V & (0.63\mu\mathrm{m} \leq \lambda \leq 2.20\mu\mathrm{m}) \end{cases} \tag{2.2.3}$$

and in the case of H$\alpha\lambda$6563, we have $k(\lambda 6563) = 3.328$.

The observable Hα flux is calculated taking into account extinction using the $E(B-V)$ value obtained from the SED fitting. Here, we followed the prescription of Cid Fernandes et al. (2005) to take into account that the extinction of Hα flux (from hot ionized gas region) is generally higher than that of stellar radiation estimated from SED fittings.

$$E(B-V) = 0.060 + 1.81 \times E(B-V)_{\mathrm{stellar}} \tag{2.2.4}$$

For the photo-z selection using optical bands, first we selected target galaxies at $1.18 < z_{ph} < 1.54$, $z' < 23.0$ and $g' - r' < 0.7$. The constraints on z' magnitude and color are added empirically, since we learned from the past FMOS observations that bluer galaxies have higher probability of detectable emission lines, and that galaxies fainter than $z' = 23$ are not usually detected at our survey limits.

Then we select galaxies with bright estimated Hα fluxes, with a flux threshold determined to keep ~ 400 target galaxies for one FMOS field. The typical threshold flux is $\sim 0.75 \times 10^{-16}$ [erg/cm^2/s] (see Table 2.2 for the values in each field). In the case of photo-z selection

using NIR J band, we repeated the same procedures as above, except that we calculated photo-z's for all the galaxies because the CFHTLS official photometric redshifts are based only on the optical bands.

It should be noted that only about 70% of all the CFHTLS Wide galaxies are detected in the UKIDSS J band, and the fraction in the galaxies selected as the FMOS target is also similar. Photo-z's of the galaxies not detected in J are calculated only with the optical bands, and this may limit the improvement of the line detection rate by adding a NIR band.

Finally, it should also be noted that our target selection does not include particular conditions to remove AGNs. Therefore, we expect a contamination of AGNs in our sample, but examination of line widths of detected galaxies by our FMOS observation indicates that the fraction is not large.

2.2.3 Test Observation and Comparison of Success Rate

We observed four FMOS fields for each of CFHTLS W1 (hereafter we call them W1_001–004) and W4 (W4_001–004) in the test observation on the nights of September 22–25$^{\rm th}$, 2011. The four different combinations of the used photometric bands (optical only or optical+NIR) and selection methods (color or photometric redshift) are applied to the four fields in each of the two CFHTLS wide fields. The corresponding selection parameters are summarized in Table 2.2.

The test observation was carried out with Subaru/FMOS. In this test observation, we used the normal beam-switching mode (NBS mode) of FMOS, with the total exposure time of 90 min in one FoV for each of the object and sky frames (See §3 and Kimura et al. 2010 for the detail of FMOS instrument). FMOS has two different spectral resolution modes, and the original FastSound plan uses the high-resolution (HR) mode ($R \sim 2200$) with 30 min exposures covering the wavelength of 1.43–1.68μm, since the throughput in HR mode is higher than in the low-resolution (LR) mode by a factor of about two, due to losses in the low resolution (LR) mode arising from the additional Volume-Phase Holographic grating used to decrease spectral resolution (Tamura et al. 2012). However, in this observing run, the HR mode was not available for IRS1 spectrograph due to a mechanism failure, and hence the IRS1 observation was done with the LR mode covering 0.9 μm–1.8 μm ($R \sim 500$). For this reason, only the results from IRS2 spectrograph will be given here, i.e., $\sim$200 galaxies in one FoV. The exposure time was set to be three times longer than that for the original

FastSound project, because the background of IRS2 was ~ 2 times higher than usual. In the full FastSound observation, the mechanical failure was corrected, and we used HR mode with 30 min exposure for both IRS1 and IRS2, as planned.

For IRS2, the wavelength coverage of the HR mode was set to be at the blue-end of H band, 1.43 μm–1.66 μm (corresponding to Hα at $z = 1.19$–1.53), and the pixel scale was 1.07 [Å/pix]. This range was chosen to be optimal, considering the balance between the maximal scientific value of FastSound (i.e., higher redshifts) and a sufficient number of emission line galaxies detectable by FMOS, based on the results of previous preliminary observations.

The weather condition was good, with mean seeing of $0.8''$. The FMOS image data was reduced by the reduction pipeline (*FIBRE-pac*: Iwamuro et al. 2012), and emission lines were searched for by automated emission line detection software (*FIELD*; see §4.2). We measured redshifts and Hα fluxes by fitting a Gaussian profile of 1-D reduced spectra. The effect of fiber losses is estimated from the relation between the covering fraction (of light falling within the $1.2''$ diameter fiber aperture) and half-light radius of galaxies used in Yabe et al. (2012). This estimate was made for FMOS fields in which the NIR data was available (i.e., W1_002, W1_004, W4_002, W4_004), and the half-light radius was estimated from the intrinsic radius of UKIDSS DXS galaxies in J-band filter and the typical seeing size of our observation ($0.65''$ for W1 and $0.8''$ for W4, FWHM). The intrinsic radius was estimated by subtracting WFCAM seeing ($0.8''$ FWHM) from the observed size (mean of the major and minor axis sizes) in quadrature. The median of covering fraction are 0.48 for W1 and 0.46 for W4, respectively, and all line fluxes of detected objects are uniformly corrected by these values. In the full FMOS observations, the fiber loss was corrected for each FoV from the measured seeing values. The detail of the data reduction will be described in §4 again.

A comparison between the line S/N and the observed Hα flux is displayed in Figure 2.3. The Hα flux corresponding to $S/N \sim 5$ is $\sim 2.0 \times 10^{-16}$ [erg/cm^2/s].

The emission line detection rates among the galaxies observed by FMOS (hereafter the "success rate" or "SR") for the four selection methods are summarized in Table 2.2. The error bars are put based on Poisson statistics. The typical success rate is $\sim$10–20%, and a general tendency of higher detection rate by the photo-z selections, relative to the color selections, can be seen. On the other hand, we can see no clear increase of the success rate, within the statistical uncertainties, due to adding NIR data. An increase of the success rate with added NIR data can be seen for the case of color selection in the W1 field, but it cannot

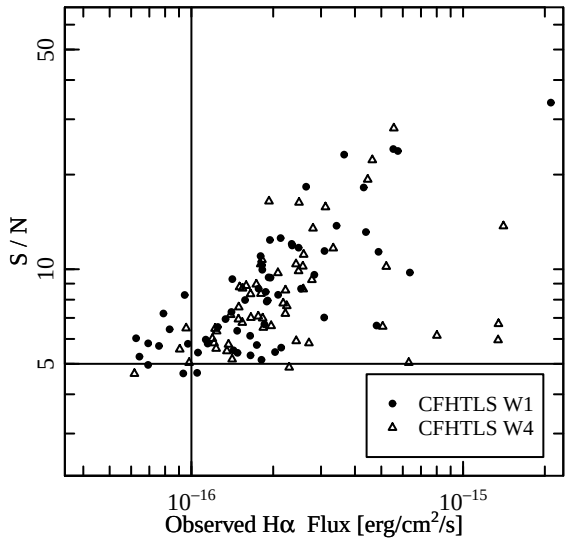

Figure 2.3: The signal-to-noise ratio of emission line detection plotted against the observed Hα line fluxes. The observed fluxes are corrected for the effects of fiber aperture loss.

be seen in the W4 field or in the cases of photo-z selections. It was expected that NIR data would be useful because of the inclusion of redshifted 4000Å breaks in photo-z calculations, but this effect may not be large for blue, star-forming galaxies having rather weak breaks.

The thresholds of $z' < 22.6$ (color selection) or $F_{\mathrm{H}\alpha,\mathrm{est}}$ (photo-z selection) are different for different fields, to keep ∼400 objects in each FMOS FoV. In order to examine whether the lower success rate (such as W4_002) is a result of a fainter z' mag or $F_{\mathrm{H}\alpha,\mathrm{est}}$ threshold in a field, we limit the statistics by taking the tightest ones of $z' < 22.65$ or $F_{\mathrm{H}\alpha,\mathrm{est}} > 0.85 \times 10^{-16}$ [erg/cm^2/s] uniformly for all fields, which is also summarized in Table 2.2. The success rates are almost unchanged, showing that the lower success rates are not caused by taking fainter targets. Also, even if we limit the $i' - J$ condition of W4_002 ($i' - J > 0.0$) to that of W1_002 ($i' - J > 0.5$), the success rate of W4_002 remains constant ($11/119 = 9.2\%$). A more strict color selection of $g' - r' < 0.5$ instead of $g' - r' < 0.7$ for the photo-z selections increases the overall success rate from 16.7% to 19.1%, though the target number density drops to ~ 290 per FoV.

The observed spectroscopic redshifts are compared with photometric redshifts in Figure 2.4. For comparison, the VVDS data used for the photometric calibration of the redshift estimation are also plotted in gray dots. $\sigma_{\Delta z/(1+z_s)}$ for galaxies observed by FMOS is larger

Table 2.2: Success rate statistics in each FoV. See §2.2 for the detailed criteria. (Note that the $i' - J$ condition is different for W1_002 and W4_002.) In addition to our baseline statistics with variable z' or $F_{\mathrm{H}\alpha,\mathrm{est}}$ thresholds to keep ∼400 targets in one field, we also show the supplementary statistics when the uniform thresholds are adopted to all the fields. The error bars on success rates are based on Poisson statistics.

FoV	Method	Band	Target	Emitters	SR (%)	z' threshold	$F_{\mathrm{H}\alpha,\mathrm{est}}$ threshold [erg/cm^2/s]
all observed objects							
W1_001	color	opt	179	20	11.2 ± 2.5	22.65	–
W1_002	color	opt+NIR	178	32	18.0 ± 3.2	22.90	–
W1_003	photo-z	opt	171	29	17.0 ± 3.1	22.90	–
W1_004	photo-z	opt+NIR	172	27	15.7 ± 3.0	23.05	–
W4_001	color	opt	174	20	11.5 ± 2.6	–	0.85×10^{-16}
W4_002	color	opt+NIR	174	16	9.2 ± 2.3	–	0.80×10^{-16}
W4_003	photo-z	opt	181	32	17.7 ± 3.1	–	0.75×10^{-16}
W4_004	photo-z	opt+NIR	164	24	14.6 ± 3.0	–	0.65×10^{-16}
uniform threshold of $z' < 22.65$ (for color-selection)							
W1_001	color	opt	179	20	11.2 ± 2.5	22.65	–
W1_002	color	opt+NIR	123	22	17.9 ± 2.6	22.65	–
W4_001	color	opt	171	29	17.0 ± 3.1	22.65	–
W4_002	color	opt+NIR	161	25	15.5 ± 2.9	22.65	–
uniform threshold of $F_{\mathrm{H}\alpha,\mathrm{est}} > 0.85 \times 10^{-16}$ [erg/cm^2/s] (for photoz-selection)							
W1_003	photo-z	opt	116	15	12.9 ± 2.2	–	0.85×10^{-16}
W1_004	photo-z	opt+NIR	90	9	10.0 ± 1.7	–	0.85×10^{-16}
W4_003	photo-z	opt	173	31	17.9 ± 3.1	–	0.85×10^{-16}
W4_004	photo-z	opt+NIR	134	20	14.9 ± 2.7	–	0.85×10^{-16}

(~ 0.8) than that for VVDS galaxies (~ 0.6). Note that $\sigma_{\Delta z/(1+z_s)}$ for FMOS galaxies is underestimated due to the selection effect (i.e., we select target galaxies within the limited range of $z_{\rm ph}$). It should be noted that in our samples, adding NIR data does not improve the redshift estimation nor decrease the number of outliers, as discussed above.

The observed Hα flux versus the estimated Hα flux from SED fittings is shown in Figure 2.5, which shows a large scatter between the observed and estimated Hα fluxes. We examined the effects of fiber loss variations for individual galaxy sizes ($\sim$ 50%) and by the positional error of fiber allocation (typically less than 10%, Yabe et al. 2012), and found that these are not large enough to account for the scatter. Therefore, this is most likely to be caused by the uncertainties in the photometric Hα flux estimates. The observed fluxes tend to be larger than that of estimated fluxes, especially for those having large observed fluxes. This is likely because of the selection effect around the FMOS detection limit; most of galaxies are around the selection threshold of the estimated flux, and some of them having large observed fluxes have high probabilities of being detected.

In right panels of Figure 2.5 we also plot the Hα fluxes estimated by fixing redshifts in the SED fitting at the measured spectroscopic values, rather than at the photometric redshifts. There is still a large scatter, indicating that the theoretical SED fitting has a large uncertainty, even if we use the correct redshifts.

We tested whether the success rate increases when K-band data are included. All of the fields of W1_004 and W4_004 (NIR, photo-z selection) are covered also by the K band, and about 60% of CFHTLS Wide galaxies are detected both in the J and K band. We then repeated the same target selection procedures given by §2.2.2 but with the K band newly added. Note that a complete test of adding K is impossible because the FMOS observation is not available for galaxies that were not selected as targets by the $u'g'r'i'z'J$ photo-z selection, though some of them would have been selected if we used also the K band. Therefore, we simply examine the line detection rate in the FMOS-observed galaxies that are also selected by the criteria including K. The success rate averaged over the W1 and W4 fields then changes from 15.2% to 15.6%, i.e., almost no improvement.

2.2.4 Comparison with the HiZELS Data

In order to determine which of the processes are mainly limiting the success rate of emission line detection, we examine our selection processes, using the data for emission line galaxies

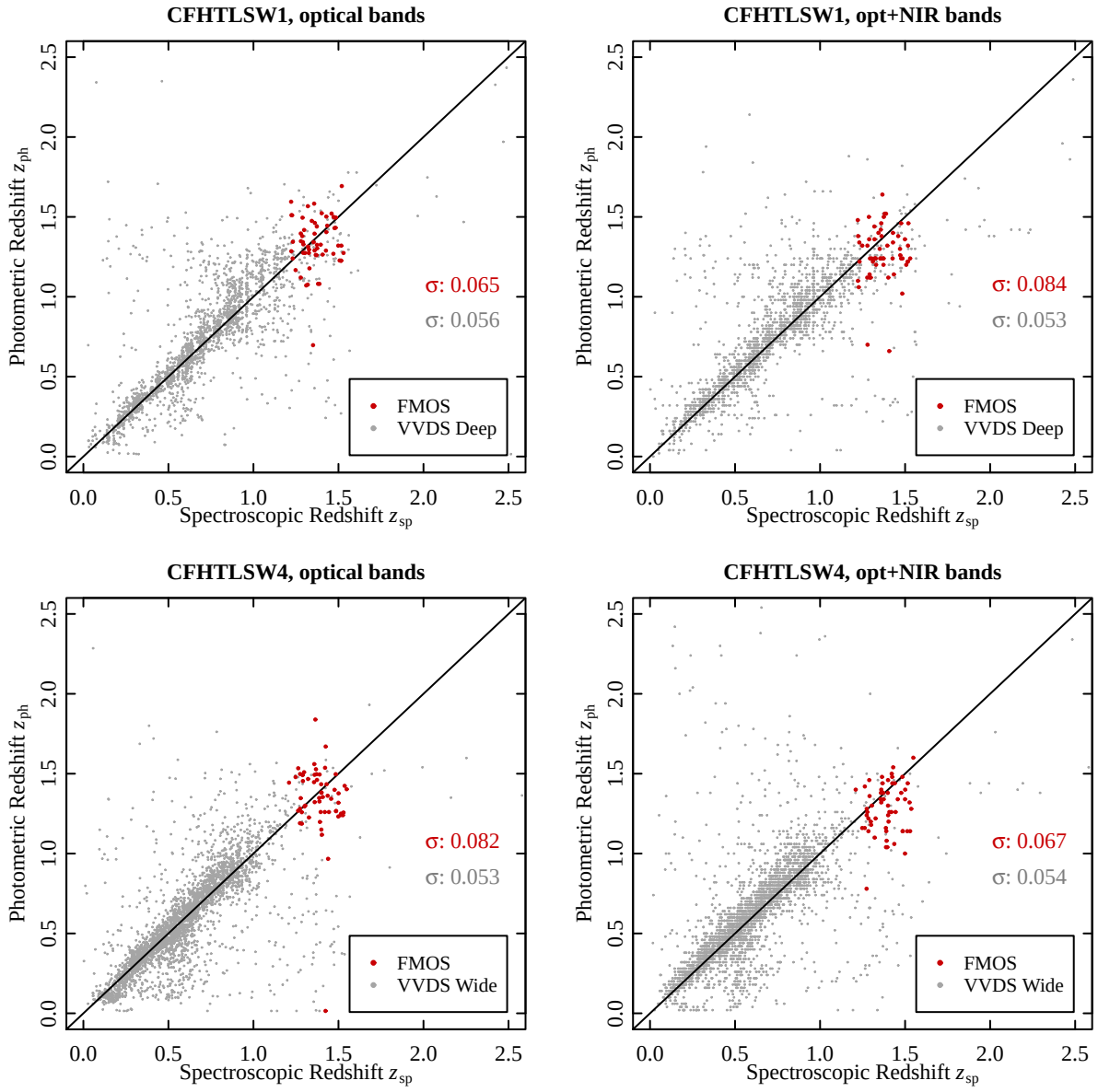

Figure 2.4: Comparison between spectroscopic and photometric redshifts for galaxies with detected emission lines (red circles) in the fields using the photo-z selection (W1_003 and 004, and W4_003 and 004). VVDS galaxies are also plotted for comparison. σ is the redshift accuracy calculated by $1.48 \times \mathrm{median}(|\Delta z| / (1 + z_s))$.

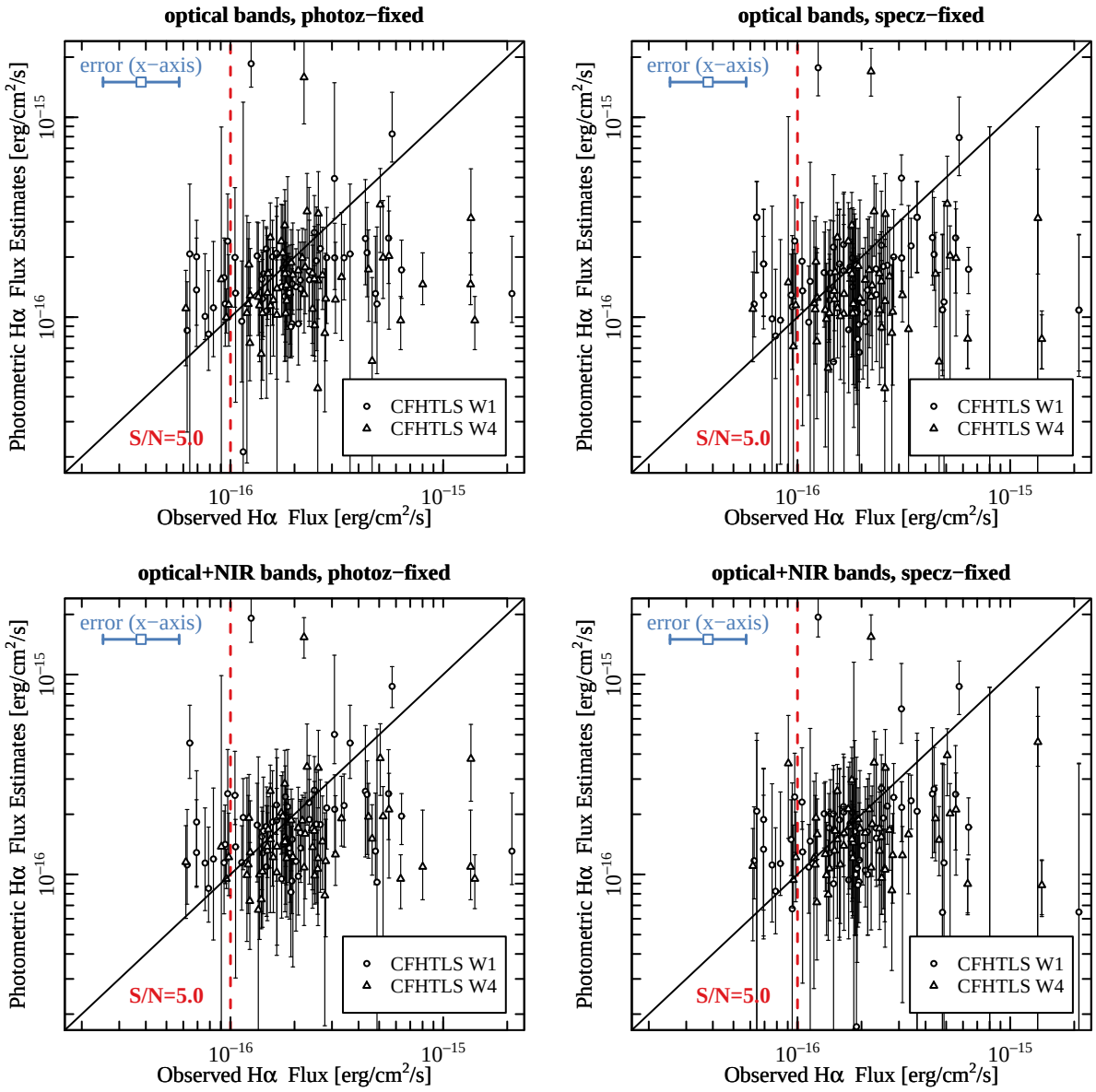

Figure 2.5: Comparison between the observed Hα fluxes from FMOS and the fluxes estimated from photometric SED fitting. Only galaxies in the FMOS fields with photo-z selection (W1_003, 004, W4_003, 004) are shown. The observed fluxes are corrected for the effect of fiber aperture loss. The photometric Hα flux estimates were made using optical bands *(top panels)* or optical+NIR bands *(bottom panels)*. In the left panels, redshifts are fixed at those estimated using SED fits to empirical SED templates, while in the right panels the redshifts were fixed at those determined spectroscopically. A typical error size along the x-axis by the fiber aperture loss (see §4.2) is shown in the upper-left corner, and the flux level corresponding to $S/N = 5$ is also shown. The y-axis errors are 1σ statistical errors derived by the *LePhare* code.

detected by the NBH narrow-band filter of the High Redshift(Z) Emission Line Survey (HiZELS: Geach et al. 2008; Sobral et al. 2009), corresponding to Hα at $z = 1.47$. Although the redshift interval corresponding to the narrow band filter is small ($z = 1.466 \pm 0.016$), the redshift is within the FastSound spectroscopic coverage, and all the Hα emitters brighter than the detection limit are included in the HiZELS sample. Therefore, we can estimate how many Hα emitters are missed by considering the effects of the FastSound target selection criteria for the HiZELS galaxies. Note that this is entirely a calculation and we do not have FMOS observations of HiZELS targets.

We use the HiZELS catalog in a 0.63 deg^2 region where the UKIDSS UDS, SXDS, and CFHTLS W1 data are available, since the color and photo-z information from SXDS and the HiZELS NB921 narrow-band imaging data in SXDS are crucial to classify HiZELS NBH emitters into Hα and others (Sobral et al. 2013). There are 192 NBH emitters having counterparts in the SXDS and CFHTLS W1 catalogs, while there are 56,576 galaxies in the same region in the CFHTLS wide catalog. The NBH line flux limit is 7.0×10^{-17} [erg/cm^2/s] (3σ), which is close to the FMOS line detection limit.

Among the 192 objects, 114 objects are identified to be Hα emitters at $z \sim 1.47$ by the [OII]+Hα double-line selection using the HiZELS NB921 (0.9196μm corresponding to [OII] λ3727 at $z = 1.47$) and HiZELS NBH (1.617μm corresponding to Hα at $z = 1.47$ data. Since the NB921 observation is deep enough to detect galaxies with small emission line ratios of [OII]/Hα $\sim$ 0.08, more than 98% of Hα emitters can be selected by this criteria (Sobral et al. 2012). Considering the FMOS redshift coverage (OH mask regions removed) that is 8.6 times wider than the HiZELS NBH width and the area of FMOS FoV (0.19 deg^2), we expect 292 Hα emitters per FMOS FoV, which is close to the number of FMOS fibers, indicating that we need an almost perfect target selection method in order to achieve $\sim$100% line detection efficiency.

NBH emitting objects that were not detected in NB921 should be emission lines other than Hα, and these are useful to estimate the contamination rate of non-Hα emitters in the target selection of FastSound. Here we classify these into the following two categories. One is the non-Hα lines that are close to Hα, such as [NII] (6548, 6583) and [SII] (6716, 6731). Although Hα emissions of these objects are outside the NBH filter window, the redshift is almost the same as Hα emitters, and hence they can be detected as Hα emitters by FastSound. Therefore, these should not be included in the contamination rate estimate. Note that we do not have to count these as Hα emitters either, since this population should

be effectively included in the above expected number of 375 Hα emitters in the FastSound redshift range. The other category is the lines whose redshifts are completely different, such as Hβ(4861), [OIII] (4959, 5007), and [SIII] (9069, 9532), which would cause a redshift mis-identification and lead to a systematic error in $f\sigma_8$.

We classify the non-Hα objects into these two categories according to whether they satisfy photo-z and color selection criteria for Hα identification of the NBH emitters adopted by the HiZELS team (Sobral et al. 2013). Since the color/photo-z criteria does not discriminate between Hα and the close lines, the objects without NB921 emission but satisfying color/photo-z criteria are considered to be the former category. There are 24 and 54 objects in the two categories, respectively, and we use only the latter for the non-Hα contamination rate estimate for FastSound. Note that the actual contamination rate may be smaller than this estimate, because we can identify Hβ(4861)+[OIII] (4959, 5007) double-emitters and remove them in the actual FMOS spectra.

We examine the color selection described in §2.2.1 using optical data, i.e., (1a) the $g'r'i'z'$ color conditions, (2a) the g' magnitude condition, and (3a) the z' magnitude condition. Here we adopt the z' magnitude threshold of $z' < 23.0$, so that there are ~ 400 target galaxies in one FMOS field. After adopting the selection criteria, 1,100 target galaxies remain in the region of the HiZELS data set, and there are 17 HiZELS Hα emitters and 1 non-Hα object. This means an Hα detection rate of 13.3% if the redshift range is scaled to that of FMOS (8.6 times larger), which is roughly consistent with the actual FMOS observation reported in §2.2.3. In table 2.3, we also show the change of galaxy numbers by adopting each step of the target selection of (1a)–(3a). The success rate (i.e., the number of Hα emitters in selected galaxies) increases by a factor of two using the color condition and three using magnitude conditions, indicating that conditions of color and magnitude are comparably important.

There is only one non-Hα emitter in the final targets selected, indicating that the contamination of non-Hα in emission lines of color selection is less than 10%, although the statistical uncertainty is large.

We also examine the optical photo-z-based selection, i.e., the conditions on (1b) photometric redshift, (2b) estimated Hα flux, (3b) $g' - r'$ color, and (4b) z' magnitude. For this region we set $F_{\mathrm{H}\alpha,\ \mathrm{est}}$ threshold to be 1.0×10^{-16} [erg/cm^2/s] to have an appropriate number of targets ($\sim$400) in one FMOS field. After these conditions have been adopted, 1,428 CFHTLS galaxies and 16 HiZELS Hα emitters are selected, yielding a success rate of 9.6% scaled into the FastSound redshift range, which is again roughly consistent with the FMOS

Table 2.3: The statistics of HiZELS and CFHTLS galaxies after selection using optical colors described in §2.2.1. The numbers in parentheses are scaled to the expected number in one FMOS field (0.19deg^2) and in the FastSound redshift coverage (z =1.19–1.53).

Selection	HiZELS Hα	HiZELS non-Hα	CFHTLS	Success Rate
without selection	114 (375)	54 (178)	56,576 (17,063)	1.7%
1a (color)	21 (69)	7 (23)	4,742 (1,430)	3.8%
2a (1a + g' mag)	18 (59)	2 (6.6)	1,179 (356)	13.1%
3a (2a + z' mag)	17 (55)	1 (3.3)	1,100 (332)	13.3%

Table 2.4: The same as Table 2.3, but for the case of optical photo-z selection described in §2.2.2.

Selection	HiZELS Hα	HiZELS non-Hα	CFHTLS	Success Rate
without selection	114 (375)	54 (178)	56,576 (17,063)	1.7%
1b ($z_{\rm ph}$)	42 (138)	11 (36)	11,993 (3,560)	3.0%
2b (1b + Hα flux)	22 (72)	4 (13)	1,943 (586)	9.7%
3b (2b + $g'-r'$ color)	21 (69)	4 (13)	1,599 (482)	11.3%
4b (3b + z' magnitude)	16 (53)	4 (13)	1,428 (431)	9.6%

observations. The change of the success rate by each step of the selection (1b)–(4b) is also shown in Table 2.4. This result indicates that the most efficient selection process is obtained by adopting the Hα threshold, followed by the selection using photometric redshifts. The empirically introduced conditions of $(g'-r')$ color and z' magnitude are not very important at least for this sample.

The distribution of photometric redshifts and photo-z based estimates of Hα fluxes for HiZELS Hα emitters are displayed in Figure 2.6, in comparison with those for general CFHTLS galaxies. It is indeed seen that the fraction of HiZELS Hα emitters in general CFHTLS galaxies increases by choosing galaxies at $z_{\rm ph} \sim 1.5$ and with strong estimated Hα fluxes. However, considerable fraction of HiZELS Hα emitters are rejected by the adopted selection criteria, because of the uncertainties in the estimated redshifts and Hα fluxes of HiZELS Hα emitters which are at $z = 1.47$ and brighter than $F_{\rm H\alpha} \sim 0.7\times10^{-16}$ [erg/cm^2/s]),

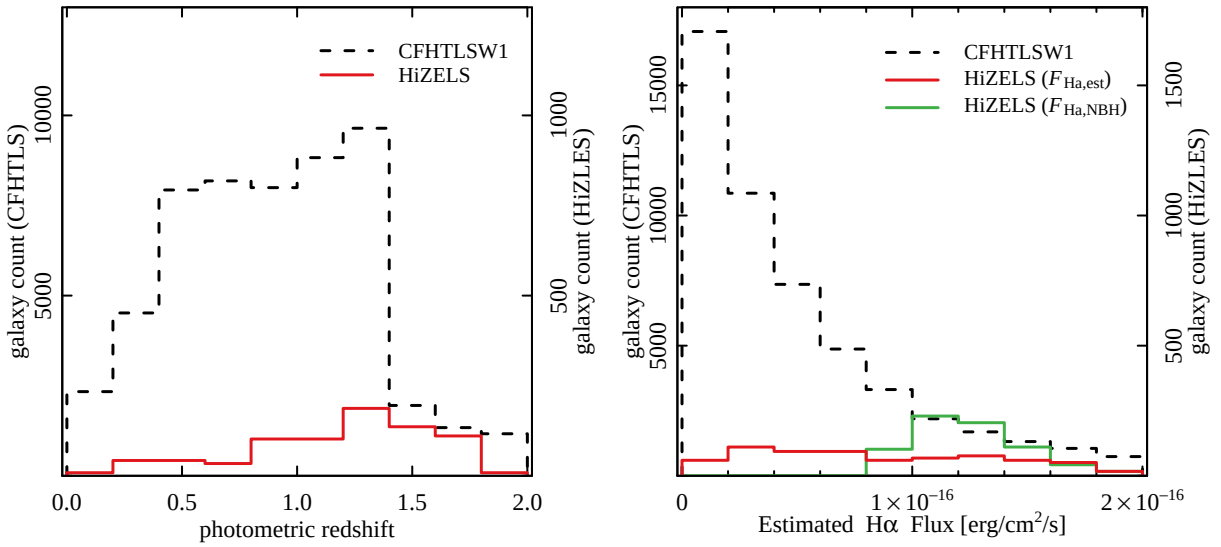

Figure 2.6: The distribution of photometric redshifts and photo-z based estimates of Hα fluxes, for the HiZELS galaxies identified as Hα emitters at $z = 1.47$ (Hα fluxes brighter than 7.0×10^{-17} [erg/cm^2/s]) and general CFHTLS galaxies. The number of HiZELS galaxies is multiplied by 8.6 to convert into the expected number in the FastSound redshift range. The actual Hα fluxes measured by the HiZELS NBH band data are also shown by green blocks.

as seen in §2.6. The accuracy of redshift estimation against the correct value (i.e., $z = 1.47$) is $\sigma_{\Delta z/(1+1.47)} \sim 0.13$, which is ~ 2 times worse than those reported for CFHTLS galaxies (Ilbert et al. 2006; Coupon et al. 2009; see also §2.2.2). This is because the objects at $z \sim 1.47$ are faint ($i' > 22.0$) in the CFHTLS wide catalogue, and because the accuracy is generally worse for blue (Hα emitting) galaxies than for red galaxies.

The number of non-Hα emitters in the final selected targets is relatively high: 4 against 16 Hα emitters, implying a contamination rate of 20% that is considerably higher than that for the color selection in the previous section. However, by examining the colors of the four non-Hα objects, we found that three of them are close to the border between Hα and non-Hα of the HiZELS criteria in the color diagrams, and furthermore we can remove Hβ(4861)+[OIII](4959, 5007) double-emitters using FMOS spectra, hence the actual contamination may be reduced.

2.3 FastSound Survey Field and Strategy

Figure 2.7 shows the FastSound footprints in the four fields. The FastSound observation regions were chosen so as to maximize its legacy value (i.e., overlap with existing data). In CFHTLS W1, the survey data of HiZELS (Geach et al. 2008; Sobral et al. 2013), SXDS (Furusawa et al. 2008), UKIDSS-DXS and UDS (Lawrence et al. 2007), VVDS Deep (Febre et al. 2005) and Wide (Garilli et al. 2008), VIPERS (Guzzo et al. 2014), and CFHTLS Deep 1 Field overlap with FastSound. Similarly, the FastSound region in W3 overlaps with the DEEP3 (Cooper et al. 2011) field, and that in W4 overlaps with the UKIDSS-DXS and VVDS Wide fields.

For FastSound, we adopted a gapless tiling pattern of hexagons inscribed in the FMOS circular FoV of 30 arcmin diameter, as illustrated in Figure 2.7. The differences of RA and DEC between two neighboring hexagons satisfy $\Delta(\mathrm{RA})\cos(\mathrm{DEC}) = \sqrt{3}r$ and $\Delta(\mathrm{DEC}) = (3/2)r$, where $r = 0.25$ deg is the radius of the FMOS FoV. The FastSound FoV-ID is related to the central point coordinates by the running integers i and j such that

$$\text{FoV ID number} = A_k i + j + B_k \tag{2.3.1}$$

$$\mathrm{DEC} = d_k - \frac{3}{2} r i \tag{2.3.2}$$

$$\mathrm{RA}' = r_{1,k} + \sqrt{3} r j \pm \frac{\sqrt{3}r}{2}\delta_i \quad (+\text{:W1,W4, } -\text{:W2,W3}) \tag{2.3.3}$$

$$\mathrm{RA} = r_{2,k} + \frac{\mathrm{RA}'}{\cos(\mathrm{DEC})} \tag{2.3.4}$$

where $\delta_i = 0$ (for even i) or 1 (for odd i), A_k and B_k are integers, while d_k, $r_{1,k}$, and $r_{2,k}$ are non-integers. These are defined in Table 2.5 for the k-th field of CFHTLS-W ($k = 1$–4). The ranges of i and j are also given in the Table 2.5. Because A_k means the number of grids in j (i.e., $j_{\max,k} - j_{\min,k} + 1$), one can calculate RA and DEC if the field ID number is given, by finding i and j as the quotient and remainder of (ID $-B_k$) divided by A_k. The FastSound FMOS FoVs are then specified by the field ID (W1–4) and the FoV ID; for example, the W1_030 FoV has $i = 1$ and $j = 9$, and its central coordinates are (RA, DEC) = (34.5137, -4.5000) in degrees.

The survey was originally planned to cover approximately the same area for the four fields of W1–4, but because of weather conditions and/or telescope/instrument problems, there is a considerable difference in the areas actually observed in each of the fields: 10, 39,

Table 2.5: The parameters relating the FMOS FoV ID numbers and the central coordinates. The parameters d_k, $r_{1,k}$, and $r_{2,k}$ are in units of degrees.

k	A_k	B_k	d_k	$r_{1,k}$	$r_{2,k}$	$i_{\rm min}$	$i_{\rm max}$	$j_{\rm min}$	$j_{\rm max}$
1	20	1	-4.125	-4.1	34.5	0	14	0	19
2	11	1	-1.25	-2.19	134.5	0	11	0	10
3	14	1	57.5	-2.72	214.5	0	16	0	13
4	6	6	1.5	0.0	333.5	0	6	-1	4

54, and 18 FoVs in the W1–4 fields, respectively. The footprints of FastSound observations are indicated in Figure 2.7, with different colors for different FastSound observing runs.

As we have seen in §2.2.3, it was found that the selection from photometric redshifts tends to give a better efficiency than color-based methods. However, there is no significant improvement by adding near-infrared band data within the statistical scatter, and UKIDSS did not cover all the FastSound survey area of 30 deg^2, which would cause systematics in the clustering analysis caused by the inhomogeneity of selection criteria. Considering these factors, we determined to select target galaxies for FastSound by photometric redshifts using only optical bands.

We selected galaxies at $1.1 < z_{\rm ph} < 1.6$, according to the redshift range of Hα ($1.18 \leq z \leq 1.54$) corresponding to the observing wavelength range of FastSound (1.43–1.67 μm using the high resolution mode of FMOS). The range $1.1 < z_{\rm ph} < 1.6$ is slightly different from that of the test observation and wider than the wavelength coverage of FMOS, because we intended to allow the $z_{\rm ph}$ range to span the wavelength coverage, including the uncertainties in $z_{\rm ph}$.

The additional conditions of optical magnitudes were $20.0 < z' < 23.0$ and $g' - r' < 0.55$. The lower limit of z' magnitude was added to avoid the contamination from stellar objects. The threshold for the estimated Hα flux, is set so that the number of target galaxies within FMOS FoV is about ~ 500, slightly more than the number of FMOS fibers, allowing for dropouts due to the fiber collision or the density contrast of galaxies. A fixed threshold flux is adopted within one of the four CFHTLS Wide fields, but it is different for different fields: 1.0×10^{-16} erg cm^{-1} s^{-1} for W1/W2, 1.1×10^{-16} erg cm^{-1} s^{-1} for W3, and 0.9×10^{-16} erg cm^{-1} s^{-1} for W4. The $u^* g' r' i' z'$ magnitude distributions of the target galaxies and fiber-allocated galaxies compared to all CFHTLS-Wide objects in the survey

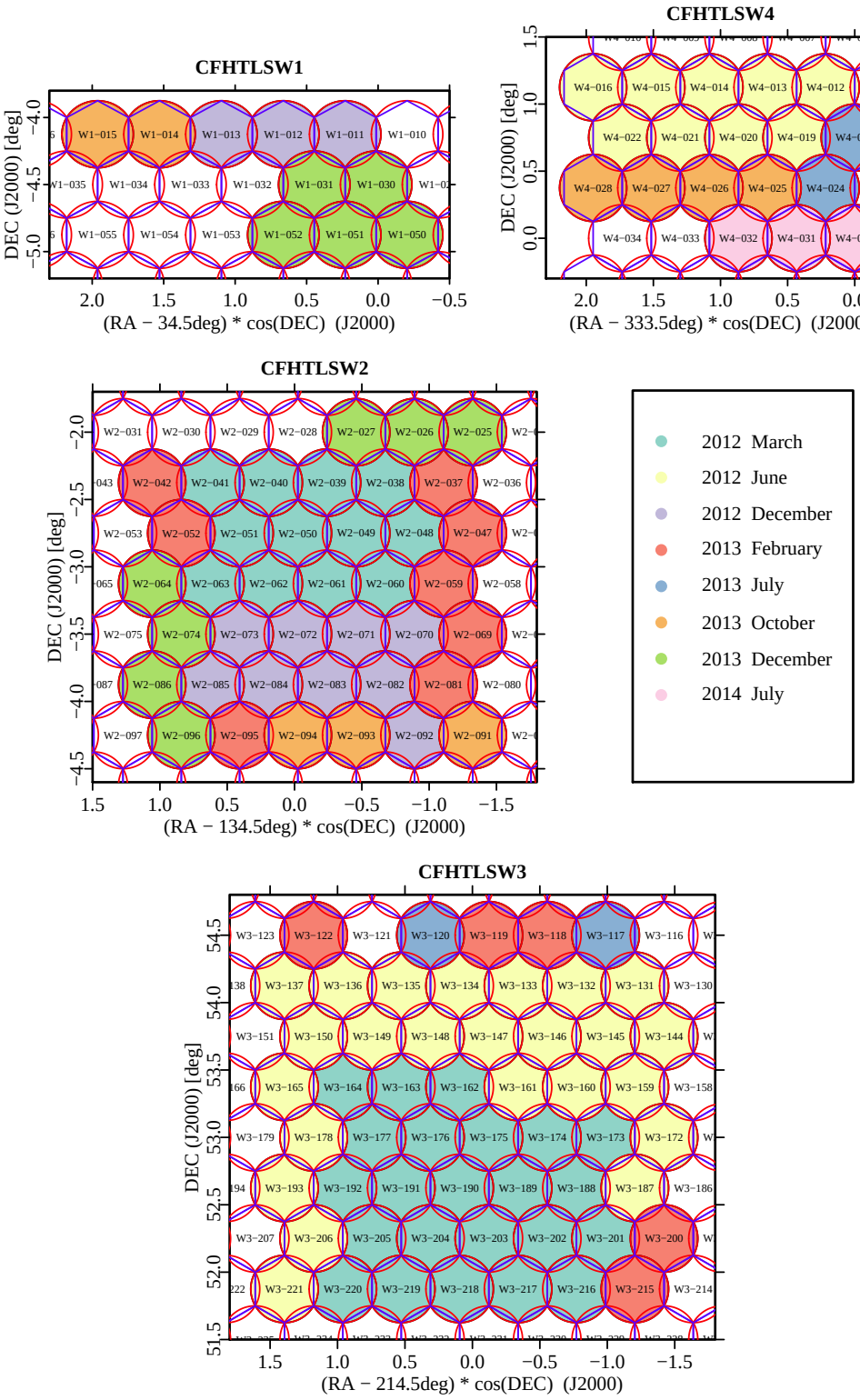

Figure 2.7: The footprints of the observed FastSound field-of-views (FoVs). FMOS FoVs (shown by red circles, 30 arcmin diameter) are arranged in a continuous hexagonal tiling. The FMOS FoV field IDs are indicated in each FoV. FoVs actually observed by FastSound are filled by different colors corresponding to different observing periods, as indicated in the figure, while the white FoVs were not observed.

footprint are displayed in Figure 3.7. Our target selection is biased towards blue star-forming galaxies, but this is not a serious problem for $f\sigma_8$ measurement within the linear regime.

Chapter 3

Observations

FMOS is a fiber-fed spectrograph capable of observing 400 simultaneous near-infrared spectra from within a 30 arcmin diameter field-of-view (FoV). It is composed of the prime focus unit for IR (PIR), 400 seventy-meter light fibers, and two spectrographs called IRS1 and IRS2 (Figure 3.1). PIR is attached to the center of the top ring of the prime focus and equipped with the fiber positioning system called Echidna, which is 15cm square and 400 fibers are populated in. These fibers are tilted by saw-tooth pulses sent from a piezo actuator with 10 micron accuracy corresponding to ~ 0.12 arcsec positioning error in the sky. The 400 light fibers connect PIR and the two spectrographs located on the floor above the Nasmith platform. Spectrographs are developed by Japan (IRS1) and UK (IRS2). They accept 200 fibers respectively and produces spectra in NIR wavelength using 2k$\times$2k detectors (Figure 3.2 for IRS2 spectrograph). Focal plane imager (FPI) is inserted around the Echidna system, and FPI has two cameras: the sky camera and the fiber camera. The fiber camera looks toward the Echidna and checks each fiber's position by the back-illumination system where each fiber illuminates the fiber camera during the fiber positioning. The sky camera is used for the focusing of a FoV before exposure and to measure the atmospheric seeing.

FMOS has two modes for fiber configuration: the normal-beam switch (NBS) mode and the cross-beam switch (CBS) mode. In NBS mode, all the 400 fibers are allocated to target objects in an on-source exposure, and then the FoV is offset to observe the off-source sky background, with the same fiber configuration. In CBS, on the other hand, the fibers are split into two groups of 200 fibers, and one observes targets while the other observes the sky background. Two exposures are taken for one target set, exchanging the role of two fiber groups. The CBS mode has the advantage of shorter observing time required to achieve a

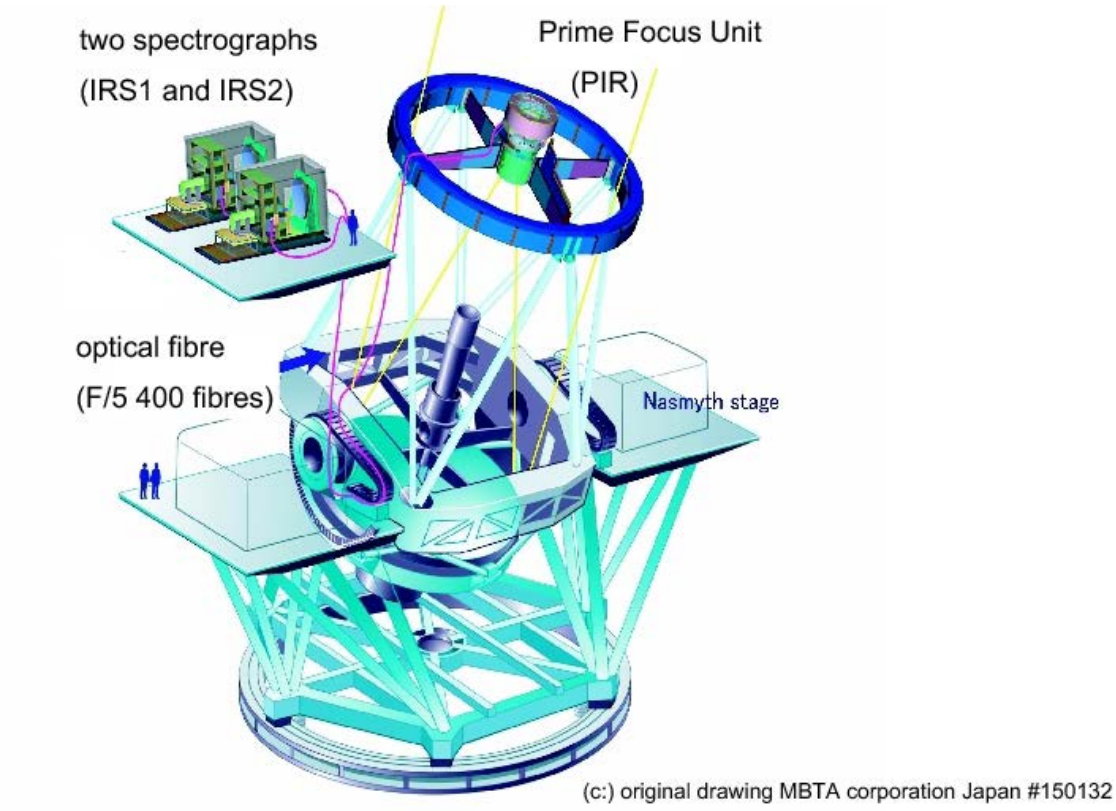

Figure 3.1: The overview of FMOS instrument. The light is collected in the PIR at the prime focus, and sent to the two spectrographs located on the dedicated platform above the Nasmith platform.

fixed S/N when targets are less than 200 in a FoV. However, CBS has the disadvantage of more complicated fiber configuration, resulting in a smaller number of allocated spines than NBS. Therefore, we chose NBS for the FastSound project.

FMOS provides two different spectral resolution modes: the low-resolution (LR) mode and the high-resolution (HR) mode. The LR mode covers 0.9–1.8 μm with a typical spectral resolution of $R \sim 500$, while HR covers a quarter of the wavelength range covered by LR with $R \sim 2200$ where $R = \lambda/\Delta\lambda$ and $\Delta\lambda$ denotes FWHM. The HR mode was chosen for FastSound because in LR the additional volume-phase holographic (VPH) grating used to anti-disperse spectra decreases the instrumental throughput by a factor of about two (Kimura et al. 2010). Figure 3.3 shows the response function of FMOS instrument. The total throughput is $\sim 5\%$ for HR mode and $\sim 2.5\%$ for LR mode. The wavelength range for FastSound was set to be $\lambda = 1.43$–1.67 μm (called H short+), corresponding to Hα λ6563

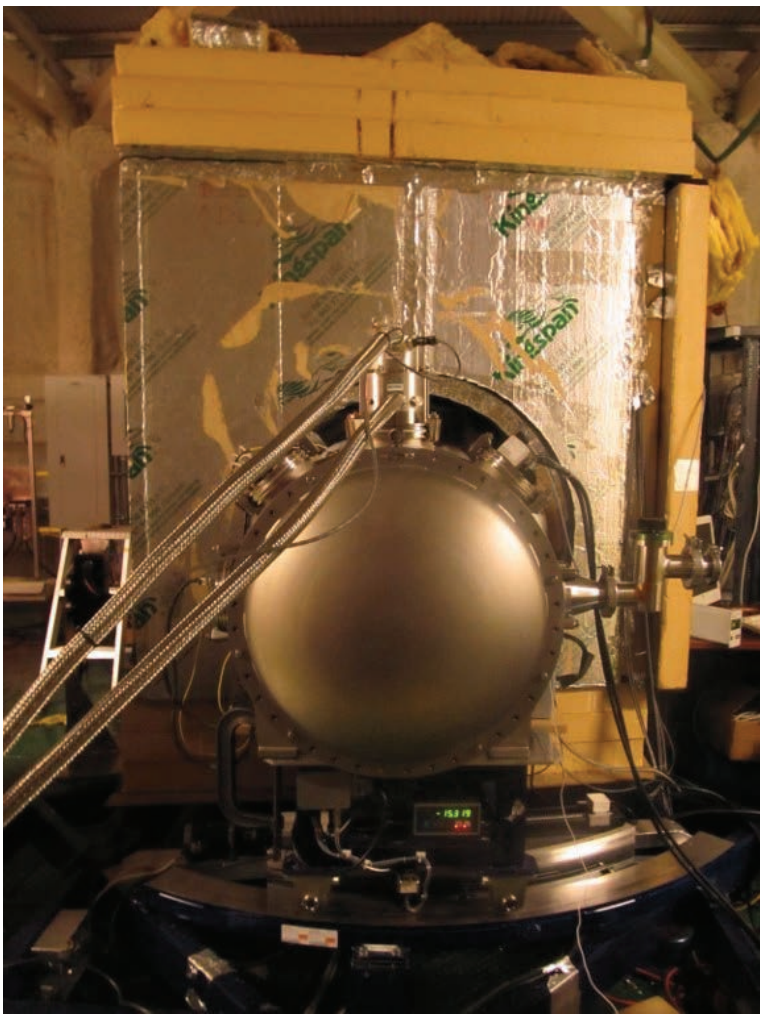

Figure 3.2: The IRS2 spectrograph. The detector is installed in the ball-like structure, which is connected to a dewar and moves to right and left, changing the wavelength coverage.

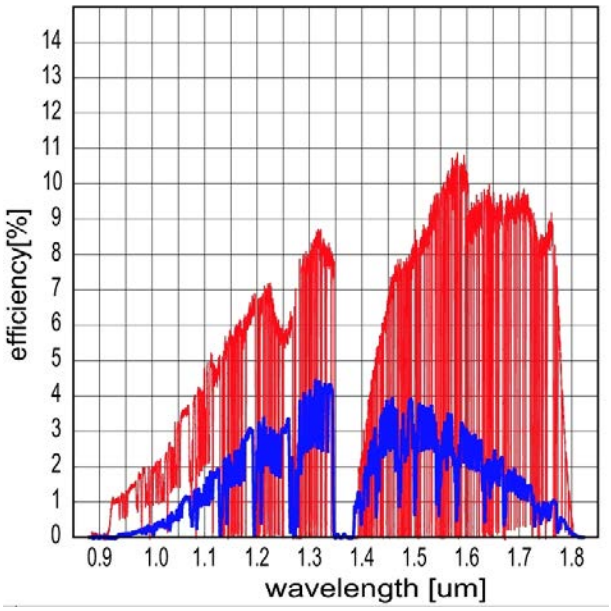

Figure 3.3: The total throughput of FMOS as a function of wavelength. The red line shows the efficiency of HR mode and blue line shows LR mode. LR mode uses VPH grating whose transparency is $\sim 50\%$. From Kimura et al. (2010).

at $z = 1.18$–1.54. In the H short+ wavelength range, the spectral resolution changes within the range of $R \sim 2000$–2700, with the typical value of 2400. The detector size is 2k×2k, and hence the pixel scale is ~ 1.1 Å/pix.

A feature of FMOS is the suppression of bright OH-airglow emission lines using OH mask mirrors (Figure 3.4), which reduce the OH-airglow emission lines by more than 90% (Iwamuro et al. 2012). Since these airglow lines are the largest noise source in the NIR region, the OH suppression allows FMOS to perform NIR spectroscopic observations with a substantially reduced background level. On the other hand, we should be careful about systematics such as the change of line detection efficiency near OH mask region or contamination from residual OH lines into emission line sample. An example of the correction for the detection efficiency is given by Okumura et al. (2015) and 5.3, and the contamination will be examined in §4.2.

The FastSound survey observed each FMOS FoV with a single set of fiber configuration including ~ 400 targets, selected by the procedures described in the previous section. The light from the targets collected by the 400 fibers of FMOS is sent to the two spectrographs, IRS1 and IRS2, each of which produces about 200 spectra. For each FoV we observed two sets of 15 min on-source and 15 min off-source, i.e., total 30 min on source. Fibers need

Figure 3.4: The mask mirror of IRS1 spectrograph. From Kimura et al. (2010).

re-configuration in the long exposures because they shift from the original position by the time. In the FastSound, one FoV is observed by the following procedure:

`Fiber configuration (15 min)` $\rightarrow$ `on-source exposure (15 min)` $\rightarrow$ `off-source exposure (15 min)` $\rightarrow$ `fiber re-configuration (15 min)` $\rightarrow$ `on-source exposure (15 min)` $\rightarrow$ `off-source exposure (15 min)`

Hence the observation efficiency is 66% and each FoV typically took about 90 min, allowing us to observe about 6 FoVs per night. Sometimes three or more source frames were taken in one FoV, depending on the quality of the data affected by weather conditions.

Seeing was measured during the observing time for each FoV, using an optical image of coordinate calibration stars (described below) taken by the sky camera in the FPI. The seeing in the FastSound data ranges from ~ 0.6 to 1.6 arcsec with a mean of ~ 1.0 arcsec in FWHM, as seen in Figure 3.5.

Fibers were allocated to the selected targets using the software Spine-to-Object (S2O, version 20101007). S2O takes ".fld" files prepared by users with the coordinate list of science targets as input and produces ".s2o" files as outputs containing the allocation results. In addition to science targets, several types of stars need to be included in the .fld files: guide stars , coordinate calibration stars (CCS), and flux calibration stars (FCS). We used the Two-Micron All-Sky Survey (2MASS) point sources catalog (Cutri et al. 2003) with available NIR

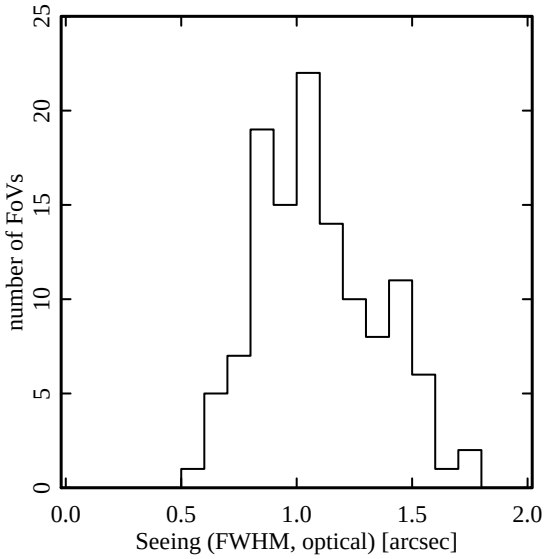

Figure 3.5: The histogram of seeing (FWHM) for all the FMOS FoVs in the FastSound survey.

magnitudes for these stars. To reduce the systematic uncertainties about the coordinates given in 2MASS and CFTHLS, we examined the cross-matched objects between the two, and found systematic offsets (typically ~ 0.07 arcsec, depending on the four fields of W1–4) between the coordinates reported by these two surveys. These offsets reduce the number of cross-matched stars, and hence this offset was corrected for each of the four fields, and the cross-match was taken again. The random errors for individual objects between the two systems are typically ~ 0.2 arcsec. We used these cross-matched objects as the star sample for all FastSound observations, using the CFHTLS coordinates for them to be consistent with target galaxies. Vega magnitudes of 2MASS catalog were converted into AB magnitudes (Tokunaga 1980):

$$J_{\rm AB} = J_{\rm Vega} + 0.870 \tag{3.0.1}$$

$$H_{\rm AB} = H_{\rm Vega} + 1.348 \tag{3.0.2}$$

$$K_{\rm AB} = K_{\rm Vega} + 1.858. \tag{3.0.3}$$

In the following, the magnitudes are given by AB magnitudes.

There are 7×2 fibers in the rightmost and leftmost of the FoV which are assigned to guide stars. They are used for the positioning of the FoV. FMOS requires at least three guide stars

near the edge of the FoV for the stable FoV guiding, and they should be bright in optical bands. We selected guide stars which satisfy the following conditions: (i) $11.5 < z' < 15.4$, (ii) $11.5 < R < 15.5$, and (iii) located at 0.22–0.30 deg from the center of a FoV. Typically, 3–6 guide stars were selected in the final s2o output. Guide stars are observed by the dedicated guide fibers of FMOS, and they do not affect the number of scientific targets. However, we avoid to use more than 6 guide stars because a large difference in magnitudes of guide stars sometimes results in the reduced accuracy of FoV guiding. Note that currently #125, 210, 252 fibers are unusable, but these can be omitted in the S2O software.

Coordinate calibration stars (CCS) were used to correct the rotational offset of FoV. We selected ~ 5 CCSs close to the center of FoV and ~ 10 distant from the center. CCSs in the outer regions provide an efficient rotational calibration, while CCSs near the FoV center are used for focusing. The sky camera of PIR takes the image of CCSs and hence no fibers need to be reserved for these stars. The selection criteria for the CCSs were (i) $11.5 < z' < 15.4$ and (ii) $11.5 < R < 15.5$. Although there is no limitation of the number of CCSs in the FoV, too many CCSs can slow down the processing speed, therefore, we selected five CCSs at 0–0.07 deg and ten CCSs at 0.10–0.23 deg randomly from the CCS candidates satisfying the conditions (i) and (ii). During the observation, we chose one of the five CCSs and measured seeing from the image taken by the sky camera.

Faint stars (15–18 mag in JH bands) are needed as flux calibration stars (FCS) for spectral calibration of science targets. We allocated about eight fibers to FCSs (i.e., four stars for each of IRS1 and IRS2), which are the same fibers as those for scientific targets. Because the light of too bright stars leaks into the neighboring pixels of the detector for other objects while too faint stars can not provide a sufficient S/N ratio at the stage of flux calibration, the selection criteria were set to be (i) $0.3 < g' - r' < 0.5$, (ii) $16.5 < r' < 18.0$, and (iii) $H > 16.25$. These conditions were also driven by the desire to select G type stars for calibration as they have flat spectra and do not have strong absorption lines in H band. Because the irregular time variation of throughput was reported for fiber # 67, 143, 148, 156, 160, 165, 216, 225, 229, 232, 239, 408 (IRS1), 362, 364, 365 (IRS2),[1] we did not use these fibers for FCSs. The correspondence of these fiber numbers and the object numbers on the detector is provided by `irs1_slit_spine.tbl` and `irs2_slit_spine.tbl` in the image reduction package (FIBRE-pac; see §4).

The parameters adopted in the S2O software are as follows. The beam-switch offset was

[1] http://www.naoj.org/Observing/Instruments/FMOS/characteristics.html#wave

Table 3.1: The selection conditions for target galaxies and calibration stars. Magnitudes denoted by small letters are from CFHTLS catalog while capital letters mean 2MASS magnitudes.

Object Name	Priority	Selection	Distance from center
Science Object	3	$1.1 < z_{\rm ph} < 1.6$, $F_{\rm H\alpha,est} \gtrsim 1.0 \times 10^{-16}$	0–0.30 deg
Guide stars	1	$11.5 < z' < 15.4$, $11.5 < R < 15.5$	0.22–0.30 deg
Coordinate Calibration Stars (Focusing)	3	$11.5 < z' < 15.2$,$11.5 < R < 15.5$	0–0.10 deg
Coordinate Calibration Stars (Rotation)	3	$11.5 < z' < 15.2$,$11.5 < R < 15.5$	0.15–0.25 deg
Flux Calibration Stars	3	$0.3 < g' < 0.5$,$16.5 < r < 18.0$,$16.25 < H$	0–0.30 deg

set to be $(10, 0)$ arcsec in the Echidna system coordinates. The target priority ("1"=highest and "9"=lowest) was set to "1" for guide stars and "3" for other objects. Another important parameter for fiber allocation is position angle (PA) of FoV relative to the celestial sphere. For each FoV, we tried various PAs to find the best one, for stable guiding (i.e., a sufficient number of guide stars) and to maximize the number of science target galaxies. Although the rotator system allows the PA of 180 ± 90 deg (0 ± 90 deg) for northern FoVs (W3) and southern FoVs (W1,W2,W4), we preferably chose the PA in the range of 180 ± 45 deg (0 ± 45 deg) for safety. For each FoV we checked that roughly equal numbers of FCSs were included for IRS1 and IRS2 fibers, and that the FCS fibers were not at edge of the detectors, to avoid a decrease of flux calibration accuracy. We accepted redundant observations and we did not omit galaxies at the edge of FoV from our target list, even if they were already observed by an adjacent FoV. The selection conditions for each type of objects are summarized in Table 3.1

Typically, we allocated ~ 360 fibers to objects, although there are ~ 400 fibers and ~ 500 targets within a FoV, which is mainly due to the fiber collision and non-uniform distribution of galaxies on the sky. This is illustrated in Figure 3.6 as a histogram of the fiber allocation percentage relative to the number of target galaxies selected by the FastSound selection condition (§2.3). The home positions of FMOS fibers are in a regular triangular lattice pattern with the fiber spacing of $84''$, and there is no inaccessible area in the FoV because

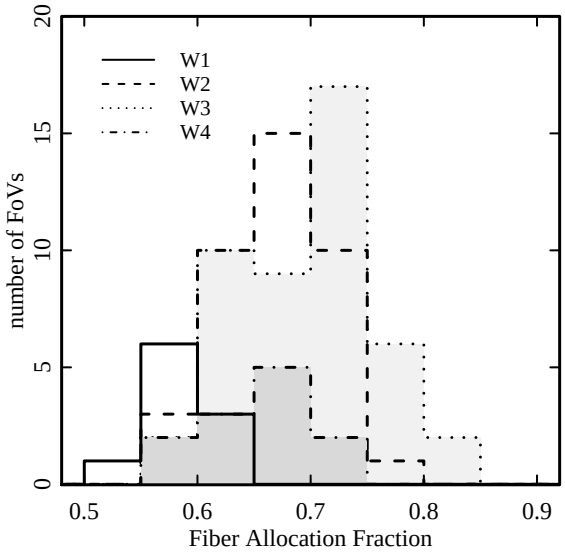

Figure 3.6: The histogram of the fraction of fiber-allocated galaxies to the FastSound target galaxies selected in §2.3.

the patrol area of the fibers is 87″ arcsec in radius. However, the minimum allowed separation between neighboring fibers is 12″ arcsec. Therefore, spines cannot be allocated to a pair of galaxies if they are closer than $\sim 12''$ arcsec. This effect will be taken into account in the clustering analysis reported by Okumura et al. (2015).

The $u^*g'r'i'z'$ magnitude distributions of the target galaxies and fiber-allocated galaxies compared to all CFHTLS-Wide objects in the survey footprint are displayed in Figure 3.7.

Figure 3.8 shows the accuracy of fiber allocation to targets, derived as the difference between input fiber positions in the ".s2o" files and those recorded during observations. The offset is within 0.12 arcsec for almost all targets, which is consistent with the designed performance of the Echidna system (Kimura et al. 2010). Figure 3.9 shows an example of GUI of S2O software after the fiber allocation was done.

The OH mask mirrors are an important feature of FMOS and are used to suppress the strong OH airglow in the near-infrared bands. When the FastSound observations started (Mar. 2012), two different mask mirrors were used for IRS1 and IRS2, made by different techniques: thin stainless steel wires were placed at the positions of OH airglow lines for IRS1, while the mirror of IRS2 was directly coated with reflective gold. There was also a difference of the masked wavelength regions between the two; the mask mirror of IRS2 masked fewer

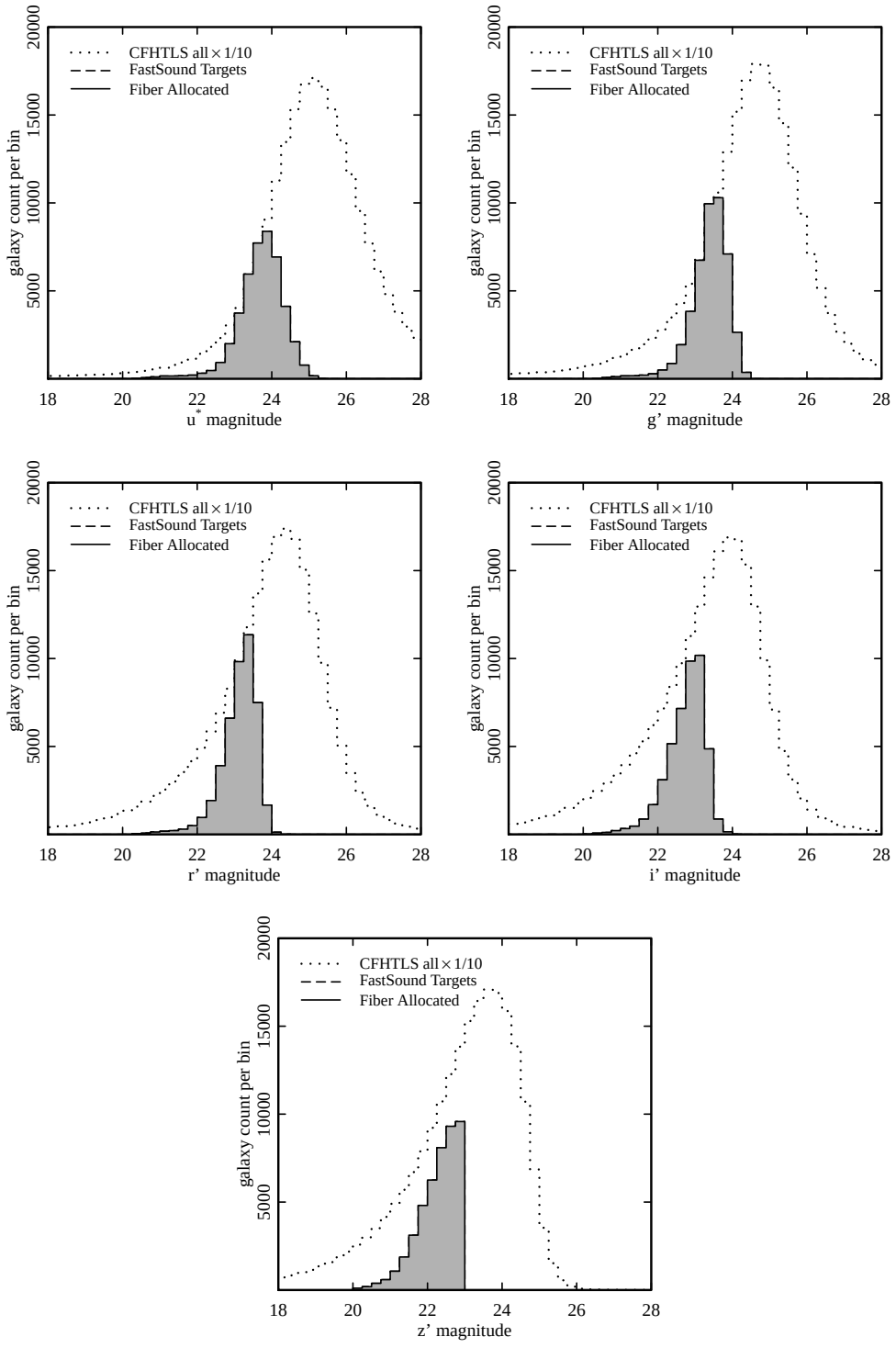

Figure 3.7: The histogram of $u^*g'r'i'z$ magnitudes of all CFHTLS Wide galaxies in the FastSound footprints (dotted), FastSound target galaxies (dashed), and galaxies that the fibers were actually allocated to (solid). The cutoff of z'-magnitude at 23.0 is due to our selection condition.

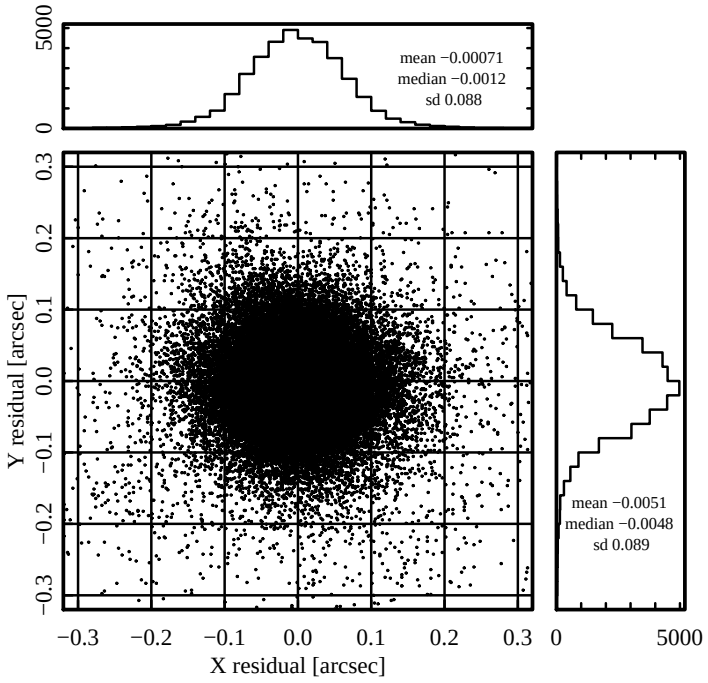

Figure 3.8: The fiber pointing accuracy for the FastSound scientific target galaxies, showing the residual between the actual fiber positions and input coordinates of targets.

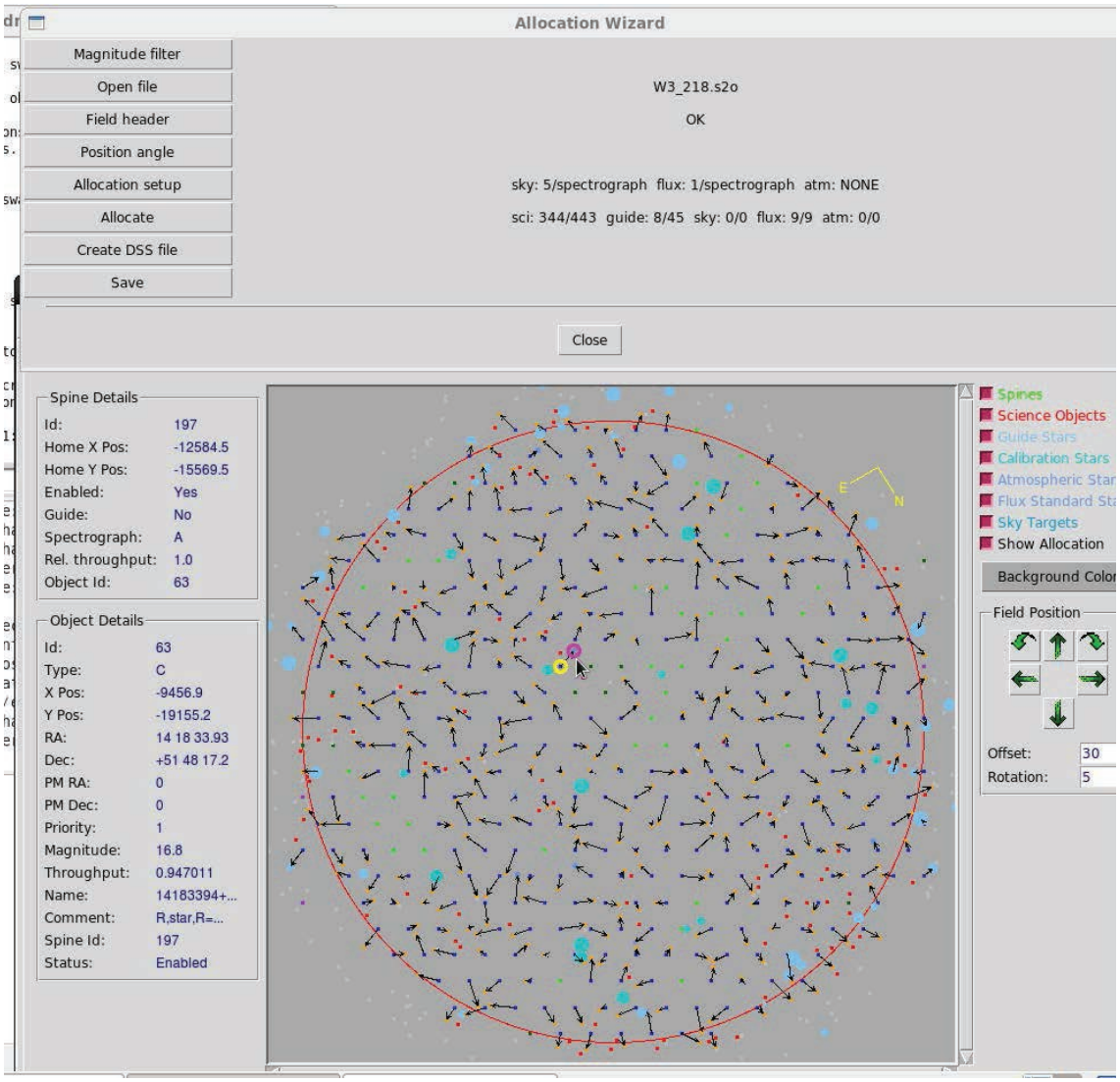

Figure 3.9: The GUI of S2O software. The configuration after the fiber allocation is shown. The arrows show the direction of fibers from the original positions to object positions.

OH lines than that of IRS1, because the former did not cover some faint OH lines. It was found that the IRS2 mask worked better and was more stable than IRS1, because the steel metal was sensitive to minute-scale changes of temperature in the refrigerator. Therefore, the IRS1 mask mirror was replaced with that masking the same wavelength regions and made by the same technique as IRS2 in an engineering run conducted in Sep 7–9 2012, i.e., during the 2-year FastSound observation campaign. This change will be appropriately taken into account in the galaxy clustering analysis. The proportion of the masked wavelength region for IRS1 decreased from 22% to 10% in the whole FMOS wavelength range in LR, and from 27% to 16% in the HR wavelength range (H short+) used for FastSound, by this upgrade.

Chapter 4

Data Reduction

The FastSound data were reduced with the FMOS data reduction pipeline (*FIBRE-Pac*: Iwamuro et al. 2012), followed by an automated emission-line search by the dedicated algorithm (*FIELD*: Tonegawa et al. 2014b).

4.1 Image Reduction of FMOS Image Data

The FMOS data are reduced with FMOS data reduction pipeline (*FIBRE-pac*). Since the detailed description of the data reduction process is presented by Iwamuro et al. (2012), here we summarize the process briefly.

The sky subtraction is performed using an object image A_i and a sum of sky image $wB_{i-1} + (1-w)B_i (0 < w < 1)$. In order to trace the time-variance of sky background, A_i is subtracted by the linear combination of immediately previous (B_{i-1}) and next sky (B_i) image. After the sky subtraction, the correction of cross talk, bias difference, bad pixel, distortion, and residual sky subtraction is made. Then, the images for each exposure are combined into one image.

The bad pixel map is made by *FIBRE-pac* during the bad pixel correction. This map indicates the quality of each pixel by a value between between 0 (bad) and 1 (normal). Those pixels on the detector flagged as non-functioning by *FIBRE-pac* and temporally prominent pixels appearing in one exposure (by cosmic ray events in most cases) are rejected and replaced in the science frames, by an interpolated value from surrounding pixels (Iwamuro et al. 2012). These pixels are stored as a bad pixel map for each exposure of 15 min. Our exposure time is 30 min, and hence we have two bad pixel maps for each field-of-view. When

these two maps are combined, true defects of the detector are presented as the value 0 on the bad pixel map because they appear in both of two bad pixel maps, while cosmic rays have a value of 0.5 because they affect only one of the two science sub-frames.

The square-noise map is also created. The square-noise map gives the square of noise level of each pixel, which is measured using 200 pixels around each pixel along the y-axis with a 3σ clipping algorithm iterated ten times. These additional maps play an important role in the automated emission line detection (§4.2) to reduce the false detections. Examples of a reduced image, bad pixel map and square-noise map is shown as Figure 4.1, 4.2 and 4.3. These images are used in the process of automated emission line detection in order not to detect cosmic rays as candidates of emission lines.

The wavelength calibration is applied by making a correlation between x-axis and physical wavelength using images of a Th-Ar lamp. The relative flux calibration is performed using a flux calibration star ($\sim$ 16.5 mag in H-band) allocated in each FoVs. The spectral type of the flux calibration star is determined by observed values at $\lambda = 1.21\mu$m and $\lambda = 1.55\mu$m, at which the throughputs of the system are same (see Figure 3.3). According to the slope of these two points, the spectral type and the expected spectrum of the flux calibration star is assumed. The line flux reported in the FastSound catalog is calculated from the observed counts of the final spectral data produced by *FIBRE-Pac*, where the counts are normalized so that 1 count per pixel corresponds to 1μJy. It should be noted that this absolute flux normalization is not calibrated by FCSs, but by assuming a fixed total throughput of 5% (in the HR mode) obtained in good observing conditions (Iwamuro et al. 2012).

The 1D spectrum of each object is extracted from the flux-calibrated image with a user-defined mask of 9 pixels. The examples of 2D image and the extracted 1D spectrum of some objects are shown in Figure 4.4. The physical properties of the lines such as line width and central wavelength are derived by 1D fitting using a standard χ^2 minimization by Levenverg-Marquart algorithm. The emission line is modeled by four parameters

$$F(\lambda) = a \exp\left[-\frac{(\lambda - b)^2}{2c^2}\right] + d \tag{4.1.1}$$

and the initial value of b and c are taken from the central wavelength and the dispersion along x-axis of the outputs of the automated emission line detection algorithm (§4.2). The initial values of a and d are set to be 1.0×10^{-16}ergcm^{-2}s^{-1}. The fitting region is confined to $\pm 10\sigma$ where σ is the line width as an output of *FIELD*. The line flux is obtained by integration over all wavelengths of the best-fit Gaussian $\sqrt{2\pi}ac$.

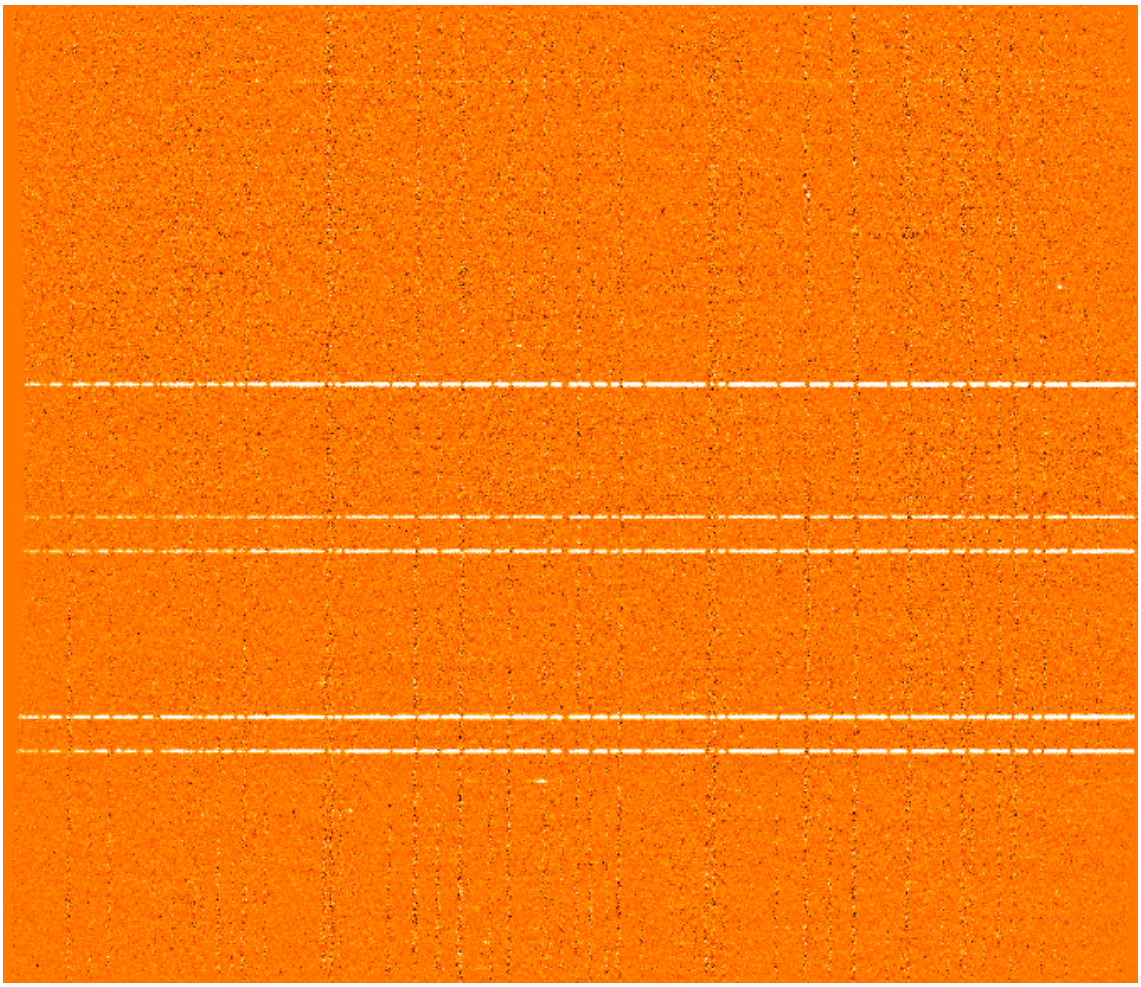

Figure 4.1: The 2-D image of FMOS produced by the reduction pipeline *FIBRE-pac*. This image is used for the automated emission line search. The image size is 2085×1800 [pix^2]. The horizontal axis represents the wavelength (1.43–1.68μm), while 9 pixels in the vertical direction are assigned to each of the 200 objects. The white lines are the continuum emission from the flux calibration stars.

Figure 4.2: A square-noise level map drawn from an IRS2 image of FMOS. White regions represent higher noise level. Vertical high noise patterns trace the residual OH airglow emission lines.

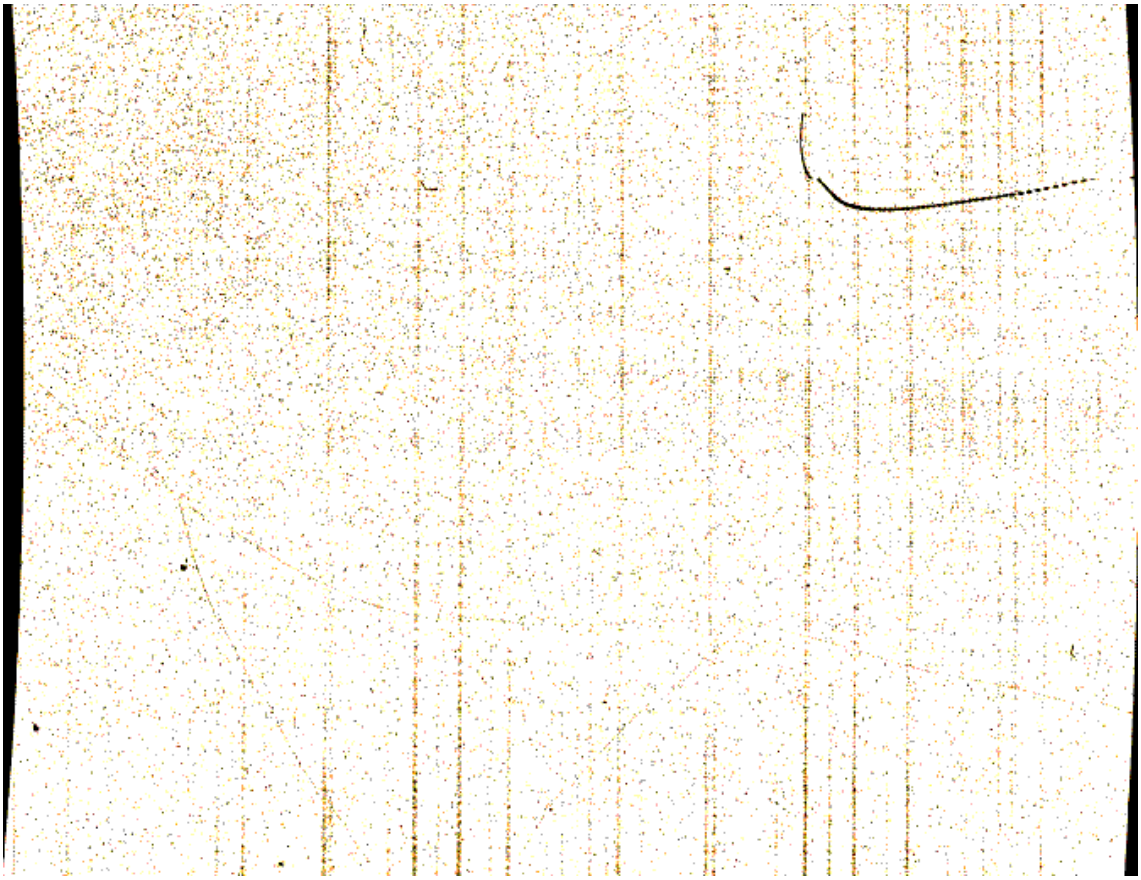

Figure 4.3: A bad pixel map drawn from an IRS2 image of FMOS. White, orange, and black pixels represent the map values of 1 (normal pixels), 0.5 (mostly cosmic ray events), and 0 (registered bad pixels), respectively. The curved feature in the top right quadrant is a scratch on the detector of the IRS2 spectrograph.

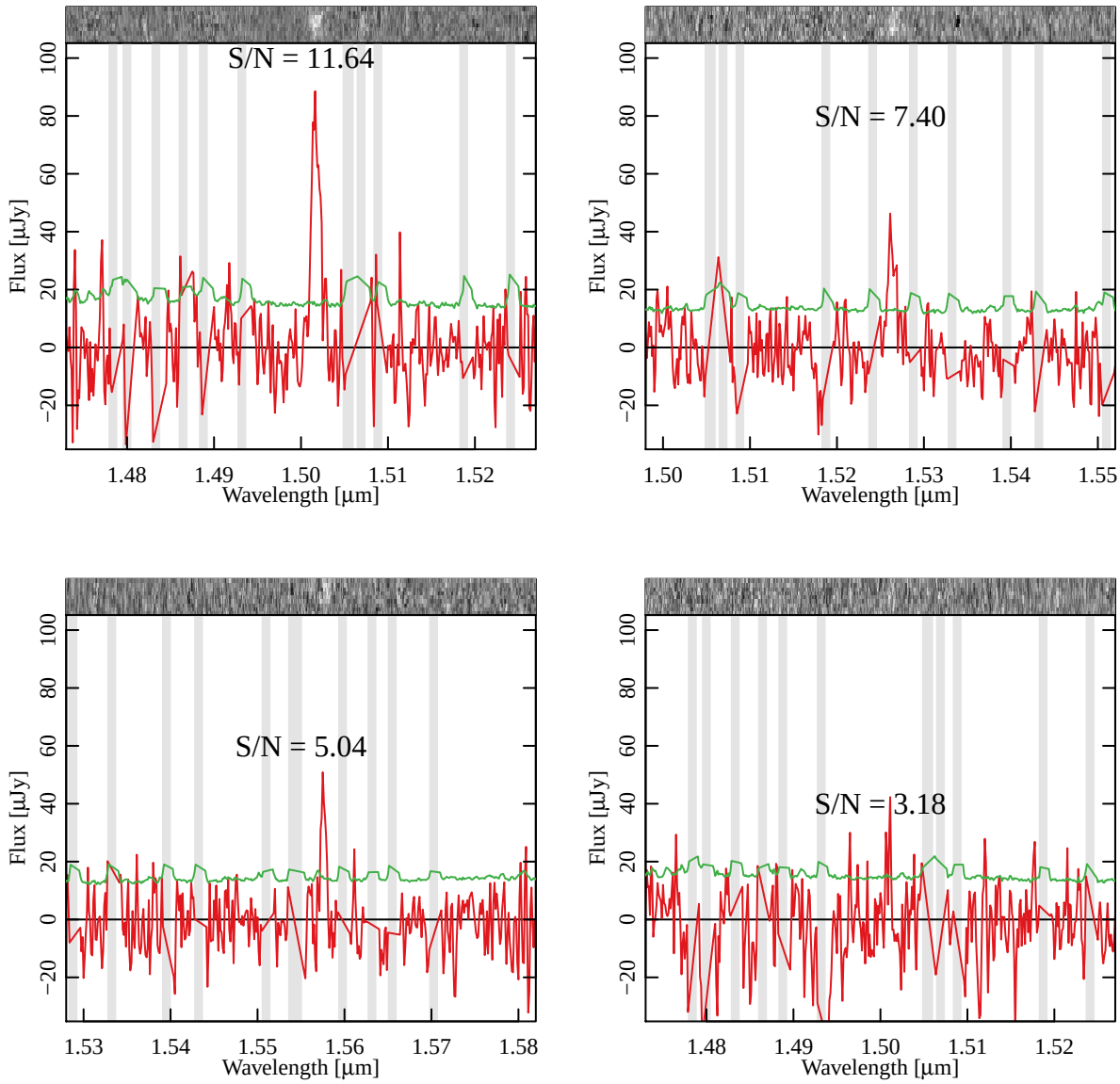

Figure 4.4: Examples of 2D images (at the top-end of each panel) and 1D spectra (main figures of each panel) of four emission line candidates with different S/N values. Gray vertical stripes indicate the positions of OH-airglow suppression mask. Green lines show the noise level, multiplied by a factor of 5 for presentation purposes. These objects were examined by eye and judged to be the correct identifications for these objects, with the exception of the lowest S/N object in the lower right panel, which was rejected.

Varying observational conditions and the fiber aperture effect against point sources can be corrected by the quantity $f_{\rm obs}$, which is defined as the ratio of the flux calculated by *FIBRE-Pac* for a FCS to that reported in the 2MASS catalog (Figure 4.5). There is typically $\sim 20\%$ scatter in $f_{\rm obs}$ for individual FCSs within a FoV, caused mainly by fiber positioning errors and chromatic and/or instrumental aberrations. The average of $f_{\rm obs}$ within each FMOS FoV ($\langle f_{\rm obs} \rangle$) was calculated and included in the FastSound catalog. In Figure 4.6, we show the distribution of $\langle f_{\rm obs} \rangle$ of all the FastSound FoVs, whose average is ~ 0.6. The total flux from a point source can be estimated by dividing the line flux in the FastSound catalog by $\langle f_{\rm obs} \rangle$, but for extended sources, an additional correction for the fiber aperture effect would be required to estimate the total flux. It is more difficult to correct the flux of extended sources (i.e. galaxies) than point sources, and there will be an uncertainty due to the correction scheme, but we provide the simplest correction in the FastSound catalog as follows.

First, the measured (observed) flux of galaxies $F_{\rm raw,gal}$ is considered to be reduced from the true flux $F_{\rm true,gal}$ because of two effects: the fiber gain for galaxies ($f_{\rm fib,gal}$) and the transparency of the atmosphere ($f_{\rm trans}$)

$$F_{\rm raw,gal} = F_{\rm true,gal} \times f_{\rm fib,gal} \times f_{\rm trans}. \tag{4.1.2}$$

Similarly, the gain of the flux for point sources is the product of the fiber gain for point sources ($f_{\rm fib,point}$) and the transparency of the atmosphere ($f_{\rm trans}$)

$$\langle f_{\rm obs} \rangle = f_{\rm fib,point} \times f_{\rm trans}. \tag{4.1.3}$$

If we assume the PSF of point sources to be Gaussian, the flux gain for point sources within the fiber aperture $1.2''$ can be derived

$$f_{\rm fib,point} = \int_0^{2\pi} d\theta \int_0^{0.6''} r dr \frac{1}{2\pi\sigma} \exp(-\frac{r^2}{2\sigma^2}) = 1 - \exp(-\frac{x^2}{2}) \tag{4.1.4}$$

where x is the ratio between the radius of fiber aperture and 1-σ seeing $x = 0.6''/\sigma$. Therefore,

$$f_{\rm trans} = \frac{\langle f_{\rm obs} \rangle}{1 - \exp(-\frac{x^2}{2})}. \tag{4.1.5}$$

Finally, as of $f_{\rm fib,gal}$, we adopted 0.47 as the value at a typical seeing and the image size of FastSound galaxies (Yabe et al. 2012; Tonegawa et al. 2014a; Tonegawa et al. 2015). We ignored the variation of $f_{\rm fib}$ among FoVs due to the change of seeing, because this effect is

small for the extended sources. As a result,

$$F_{\rm true,gal} = \frac{F_{\rm raw,gal}}{0.47} \times \frac{1-\exp(-\frac{x^2}{2})}{\langle f_{\rm obs}\rangle} \tag{4.1.6}$$

is listed in the FastSound catalogs.

As well as the normal science frame, we also create an "inverted" science frame by exchanging object and sky frame in the *FIBRE-pac* procedures. The line detection algorithm is also applied to this inverted science frame. Any candidates detected in this inverted frames will not be genuine features, because real emission lines are negative in the frame and absorption lines are usually below the detection limit of FMOS for galaxies beyond $z \sim 1$. Therefore, we can reduce the overall false detection rate by tuning the software to minimize the detection rate in the inverted frames.

4.2 Development of Line Detection Software

A key for studies treating many emission line galaxies in a large data set is to automatically search and detect emission lines. Using automated emission line search instead of eye inspection allows us to save time and to avoid false detections. In the case of FMOS, residual OH airglow lines just outside the OH mask regions and cosmic rays often show spectral shapes similar to those of real emission lines. If such spurious line detections are included into a statistical sample of emission lines, they will cause a systematic error in, e.g., measurements of galaxy clustering power spectra. Therefore, an efficient automatic line detection software with minimized probability of false detection is highly desirable. In the FastSound project, emission lines were searched for automatically using the software algorithm, FMOS Image-based Emission Line Detection (*FIELD*), developed for the FastSound project (Tonegawa et al. 2014b). We briefly summarize the algorithm here.

4.2.1 Line Candidate Selection by Convolved Signal-to-Noise Ratio

Our algorithm is based on a convolution of the FMOS 2-D spectral images weighted by a detection kernel that is similar to the typical emission line profile (see, e.g., Gilbank et al. 2010 for similar approaches). We do not use the flux-calibrated 1-D spectra for emission line detection because they do not retain the 2-D shape of the PSF, which is useful to filter

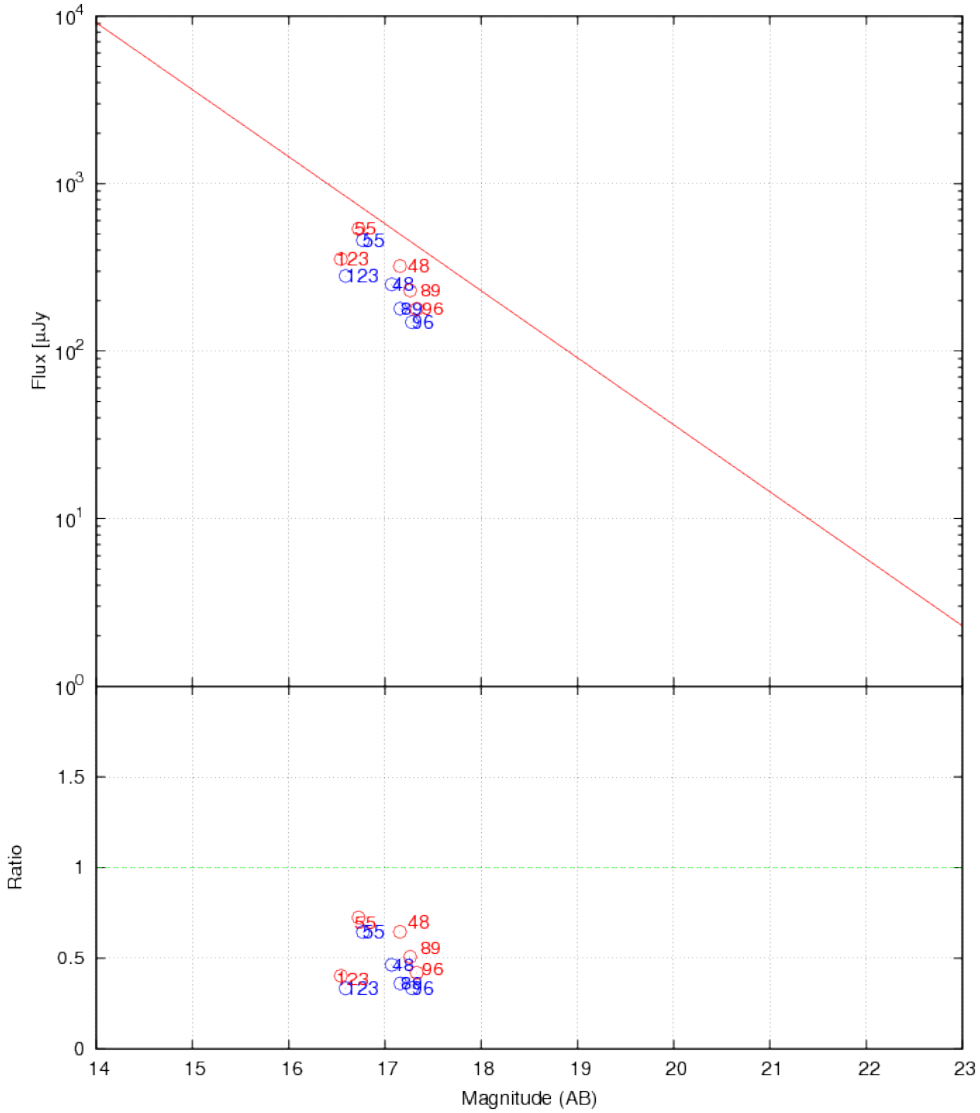

Figure 4.5: The ratio between photometric magnitudes and observed flux of W2_085 field. The dotted line shows the 100% efficiency (corresponding to $f_{\rm obs} = 1$). Blue points and red points represent J and H magnitude respectively.

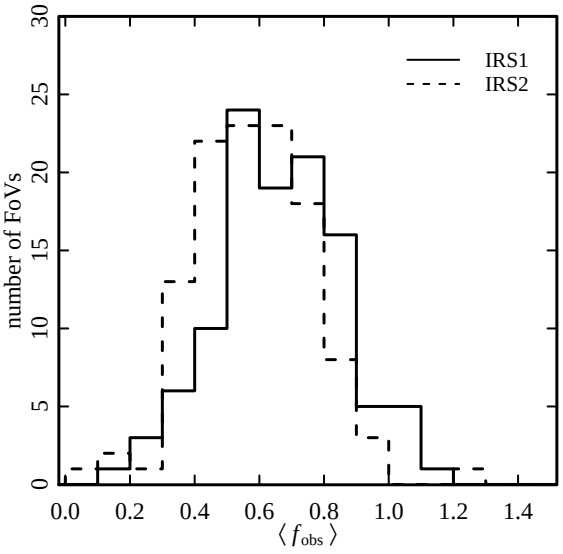

Figure 4.6: The distribution of $\langle f_{\rm obs} \rangle$ within each FoV.

out false detections. 1-D spectra are used for the measurement of emission line fluxes (§4.1). This algorithm also uses a flat-field image, square-noise map and bad pixel map as well as the science frame. The science frame and square-noise map are both convolved with the kernel, producing an effective signal-to-noise (S/N) ratio of a line centered at each pixel along the wavelength direction. The flat-field image and bad pixel map are used to remove the OH mask regions or bad pixels from the calculation of S/N, so that the false detection rate is minimized.

An important feature of the FMOS spectra in the NIR is the hardware suppression of the the OH airglow. Inclusion of the masked regions does not improve the line detection efficiency, and the noise level is often particularly high at the border of OH masks, which would have a negative effect for efficient line detection. To remove such regions, we utilize the dome-flat image. The dome-flat image is divided by the detector-flat image to correct for different quantum efficiency between pixels (Iwamuro et al. 2012). After normalization, the flat-field image have values of ~ 1 at normal pixels, while ~ 0 at OH mask regions. We then make a new square-noise map by dividing the original square-noise map by this flat image. This operation increases the noise level inside and around OH mask regions by a large factor, making such regions ineffective in the line S/N calculation. This approach is better than, e.g., simply removing OH mask regions by wavelength information, because

the detailed performance of the OH mask depends on the temperature of FMOS instrument that changes with time. However, the effect of noisy regions around the border of OH masks cannot be completely removed by this operation, and hence we further remove the pixels whose original noise level (before dividing by the flat image) is higher than the mean by more than 2σ, from the line S/N calculation.

In order to decrease the chance of detecting cosmic rays and detector defects, we make use of the bad pixel map (Figure 4.3). Since the bad pixel map has values of ~ 1 at good pixels, ~ 0 at defects, and ~ 0.5 at pixels hit by cosmic rays, we exclude the pixels having values lower than 0.7 in the bad pixel map from the line S/N calculations.

Because the continuum component of galaxies may affect the detection efficiency of emission lines, the continuum component of each spectrum in the object frame is subtracted by applying fit1d task of IRAF with a 5th-order Chebyshev polynomial along the wavelength direction. This procedure is adopted separately for each pixel along the vertical direction perpendicular to wavelength.

We define the detection kernel by a two-dimensional Gaussian that imitates the typical shape of an emission line:

$$g(x, y) \equiv \exp\left[-\frac{1}{2}\left(\frac{x^2}{\sigma_x^2} + \frac{y^2}{\sigma_y^2}\right)\right]. \tag{4.2.1}$$

where σ_x and σ_y are the typical dispersion of emission lines along x-axis (corresponding to wavelength) and y-axis (corresponding to the fiber aperture) on the detector.

Although σ_x and σ_y are adjustable, we fix $\sigma_x = 4.26$ [pix] as the quadratic sum of the spectral resolution of FMOS (6.375 Å FWHM at $\lambda = 1.53$ μm in the HR mode) and the typical velocity dispersion of galaxies (175 km/s FWHM), and $\sigma_y = 2.5$ [pix] as representative of the FMOS fiber profile on the detector. Because FMOS is a fiber-fed spectrograph, σ_y is just an instrumental spread of light from fibers without spatial information of target objects.

For each pixel (x_c, y_c), we define the signal S of a supposed line centered at the pixel (x_c, y_c) as:

$$S(x_c, y_c) = \alpha \sum_{(x_i, y_i) \in D} g(x_i - x_c, y_i - y_c), \tag{4.2.2}$$

which is an integration over pixels (x_i, y_i) around (x_c, y_c) confined within the region D. This region is an ellipse whose center is (x_c, y_c) and the radii along the major and minor axis are $2\sigma_x = 8.52$ [pix] and $2\sigma_y = 5.0$ [pix]. The parameter α is the best-fit flux normalization of this kernel to the observed count c_i in the pixels in D:

$$\alpha = \frac{\sum_{(x_i,y_i)\in D} c_i \frac{g(x_i-x_c,y_i-y_c)}{n_i^2}}{\sum_{(x_i,y_i)\in D} \frac{g(x_i-x_c,y_i-y_c)^2}{n_i^2}} \ , \tag{4.2.3}$$

which can be derived by minimizing χ^2, where

$$\chi^2 \equiv \sum_{(x_i,y_i)\in D} \frac{[c_i - \alpha g(x_i - x_c, y_i - y_c)]^2}{n_i^2} \ , \tag{4.2.4}$$

where n_i is 1σ noise at i-th pixel from the square-noise (n_i^2) map. From the expression for α, it can be understood that the signal S (Equation 4.2.2) is a convolution of the count c_i with the detection kernel, weighted by $1/n_i^2$. We then define the noise N for the line; since S is a linear combination of c_i whose noise is n_i, its statistical error can be calculated as:

$$N(x_c, y_c) = \frac{\sum_{(x_i,y_i)\in D} g(x_i - x_c, y_i - y_c)}{\sqrt{\sum_{(x_i,y_i)\in D} \frac{g(x_i-x_c,y_i-y_c)^2}{n_i^2}}} \ . \tag{4.2.5}$$

Then the signal-to-noise ratio S/N is simply calculated from S and N (Figure 4.7).

The S/N is calculated along the wavelength direction, with y_c fixed at the central pixel ($y_c = 0$) among the 9 pixels for one fiber. When a certain pixel has a local peak of S/N map, the pixel is likely to be the center of an emission line feature. Therefore, we select emission line candidates by extracting pixels with S/N values higher than a threshold and locally greatest within the range of ± 20 pixels from x_c along the wavelength direction. The latter condition is introduced to avoid multiple detections of the same line-like feature. Although the use of ± 20 pixels as the minimum separation is a simplistic approach, it suffices for FastSound, because the closest lines (H$\alpha\,\lambda 6563$ and [NII] $\lambda\lambda 6548, 6483$) at $z \sim 1.3$ are separated by $\gtrsim 40$ [pix] on the image. The S/N threshold can be changed by the user: if one increases the threshold, the number of false detections decreases but the number of real lines would also be reduced. The false detection rate and its dependence on the threshold are discussed in §5.1.

4.2.2 Further Selection by Image Shape Parameters

The image shape of each candidate line includes important information that allows discrimination between real and false lines. We measure the following shape parameters:
(1) center along y-axis:

$$\overline{y} = \sum_{(x_i,y_i)\in D} y_i c_i \Big/ \sum_{(x_i,y_i)\in D} c_i. \tag{4.2.6}$$

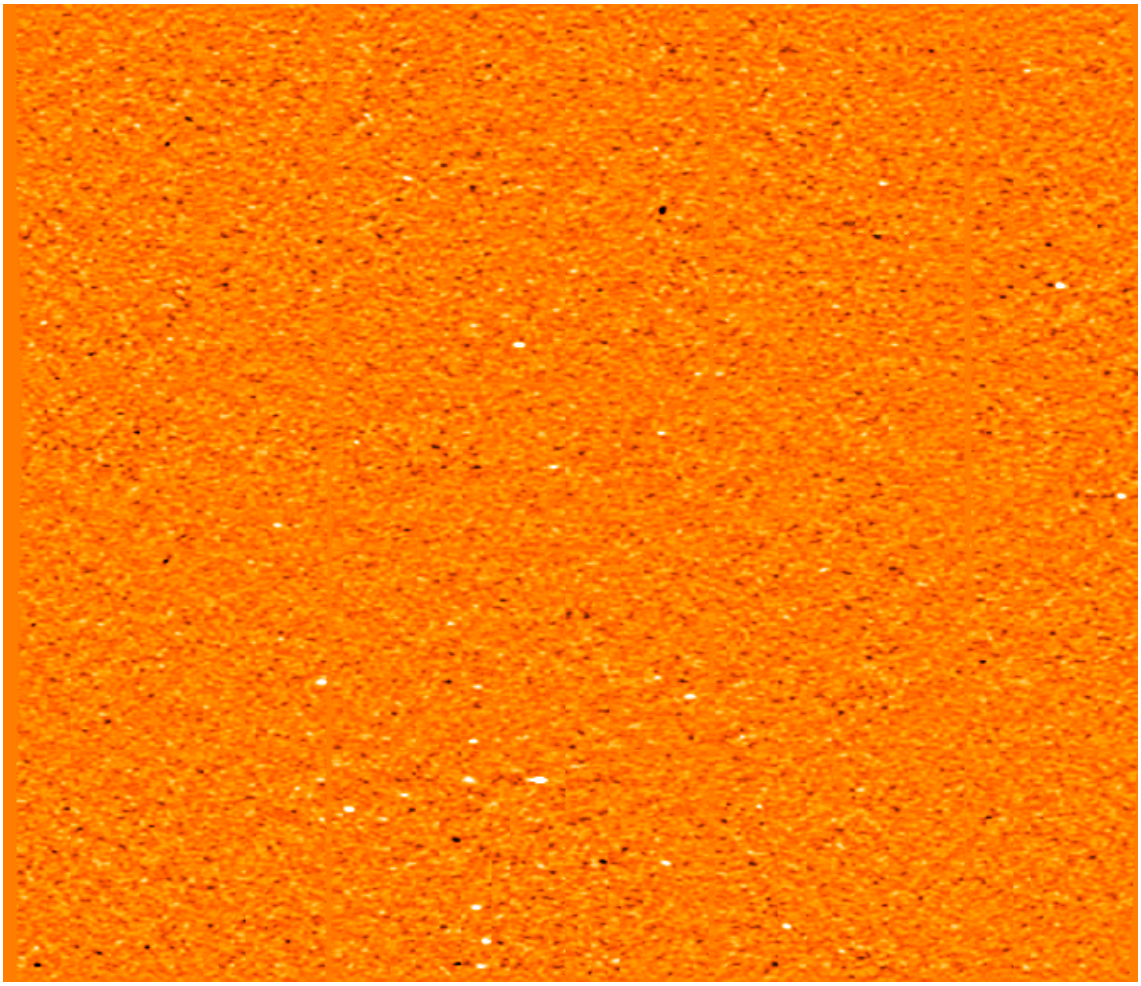

Figure 4.7: The convolved S/N map calculated by the description of §4.2. White pixels represent that the convolved S/N value is high there.

(2) dispersion along y-axis:

$$\sigma_y{}^2 = \sum_{(x_i,y_i)\in D} (y_i - \overline{y})^2 c_i \Big/ \sum_{(x_i,y_i)\in D} c_i. \tag{4.2.7}$$

(3) fraction of positive pixels:

$$f_p = \sum_{(x_i,y_i)\in D} H(c_i) \Big/ \sum_{(x_i,y_i)\in D} 1 \ , \tag{4.2.8}$$

where $H(x)$ is a step function (1 for $x > 0$ and 0 otherwise).
(4) position angle of the major axis of an elliptical fit:

$$\theta = \frac{1}{2} \arctan\left(2\frac{\overline{xy}}{\overline{x}^2 - \overline{y}^2}\right) \tag{4.2.9}$$

(5) axis ratio of the elliptical fit:

$$\frac{b}{a} = \frac{\frac{\overline{x^2}+\overline{y^2}}{2} - \sqrt{\left(\frac{\overline{x^2}-\overline{y^2}}{2}\right)^2 + \overline{xy}^2}}{\frac{\overline{x^2}+\overline{y^2}}{2} + \sqrt{\left(\frac{\overline{x^2}-\overline{y^2}}{2}\right)^2 + \overline{xy}^2}} \tag{4.2.10}$$

where a and b are semi-major and minor axes, respectively.
(6) signal-to-noise fluctuation per pixel:

$$\sigma_{\rm SNR} = \left\langle \frac{c_i^2}{n_i^2} \right\rangle - \left\langle \frac{c_i}{n_i} \right\rangle^2 \ , \tag{4.2.11}$$

We applied our algorithm to an "inverted" science frame, obtained by running the FMOS image reduction pipeline with the object and sky frames exchanged, as well as the "normal" science frame. Because the sensitivity of FMOS is not enough to capture the continuum line from our target galaxies, all the candidates in the inverted frames must be spurious. Also, their statistical nature should be the same as the spurious features in the normal frames, because the analysis procedures are exactly the same except for swapping the object/sky frames. For example, residual OH emission lines in the science frame can be positive or negative at the same probability depending on the observing conditions, and cosmic rays fall randomly both on the object and sky frames. Note that an emission line galaxy can accidentally fall in a fiber during the sky exposures, but we did not take these cases into account, because the possibility should be small.

Eight FoVs W2_041, 062, 063, W3_162, 163, 164, 177, and 192 are selected as a representative of FastSound data in normal observing conditions, and W2_042, W3_173, 206 and 221 was selected as bad observing conditions, where there were unusual dark patterns on the edge of detector, likely because of the instability of detector resulting from overexposures by dome-flat lamp. Figure 4.8 shows the distribution of the shape parameters defined above, as a function of S/N, both for the normal and inverted frames of normal 8 FoVs and unusual 4 FoVs.

It is found that in some regions (especially for the data in the 4 FoVs at the bad condition in the plots of σ_y^2, θ, b/a, and $\sigma_{\rm SNR}$ plots) the number of inverted-frame objects is relatively large compared with the normal-frame objects, and the numbers in normal/inverted frames are similar. False lines are expected to be dominant over real lines in such regions, and hence we introduce event cuts as shown by the solid curves in the figure. These conditions are expressed as:

$$\sigma_y > 4.210 + 6.868\left(\frac{S}{N}\right)^{-1} + 36.413\left(\frac{S}{N}\right)^{-2} \tag{4.2.12}$$

$$|\theta\ [\mathrm{deg}]| > 15.00 + 94.79\left(\frac{S}{N}\right)^{-1} + 26.30\left(\frac{S}{N}\right)^{-2} \tag{4.2.13}$$

$$\sigma_{\rm SNR} > 7.701\times10^{-3} + 3.609\times10^{-3}\left(\frac{S}{N}\right)^{-1} + 0.5416\left(\frac{S}{N}\right)^{-2}. \tag{4.2.14}$$

It should be noted that the region of many inverted-frame objects is also found in the plot of minor/major axis ratio. We did not include a condition on this quantity, because we found that almost all of the false objects in this region were effectively removed by the other three conditions. We also examined the spectral images of the rejected events by eye, and confirmed that false detections did indeed dominate. These events mainly arise from unusual dark patterns appearing in the bad-condition four FoVs, when the detector was in an unstable state.

The completeness of detection, i.e., the probability of successful detection for a given real emission line is also an important statistic to evaluate the performance of the software. To estimate this we ran a simulation by placing artificial objects and then applying our detection algorithm. The completeness against input brightness (S/N) is displayed in Figure 4.9, for some different values of detection S/N thresholds. The completeness does not reach 100%

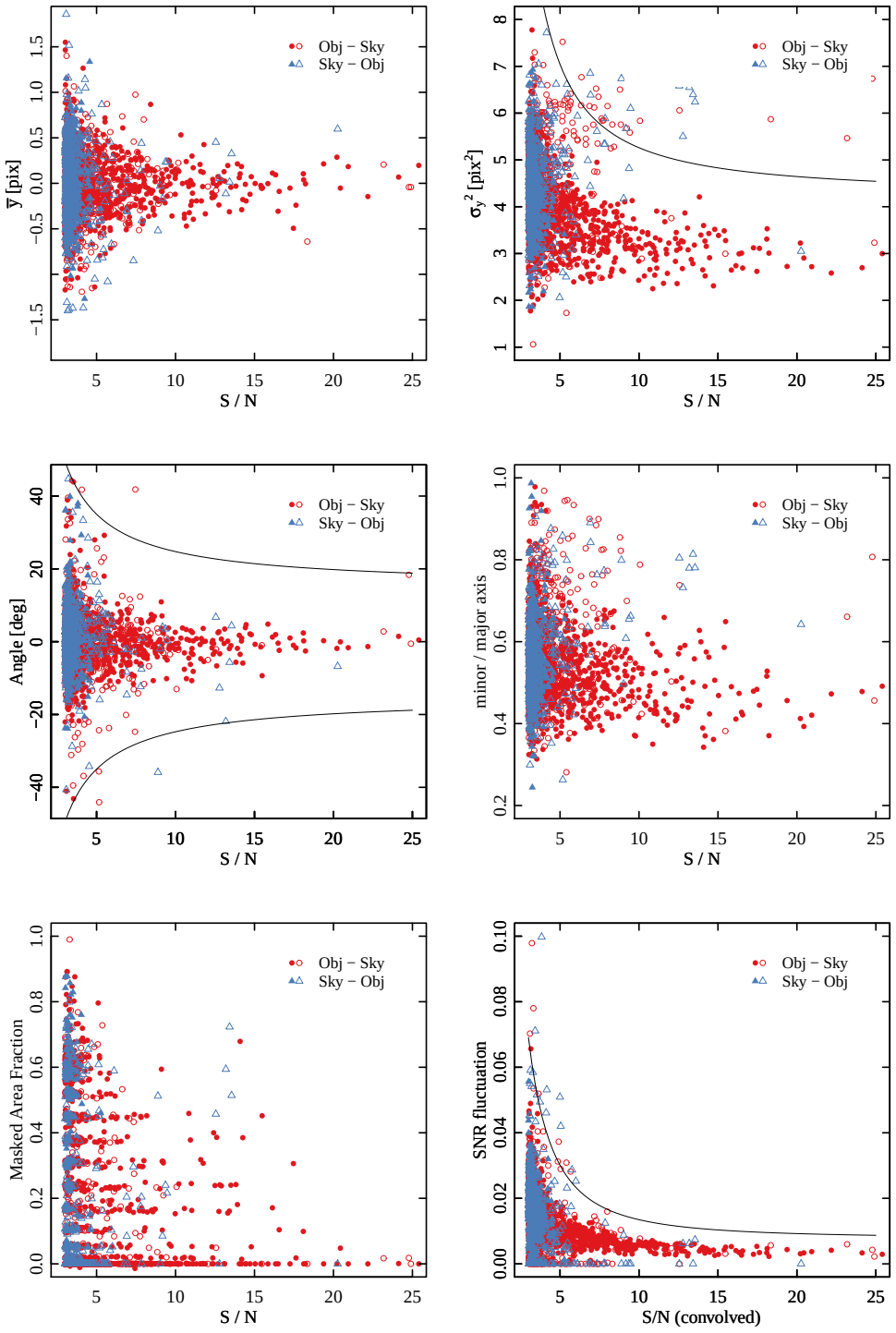

Figure 4.8: The six shape parameters as a function of S/N, for the normal (red circles) and inverted (blue triangles) frames. Filled symbols are used for line candidates in the eight FMOS FoVs taken in normal conditions and open symbols for the four FoVs taken in the bad condition. The solid curves show the parameter cuts adopted to remove false-detections. In the top-left panel, the zero-point of y is set at the midst of the nine pixels for each fiber.

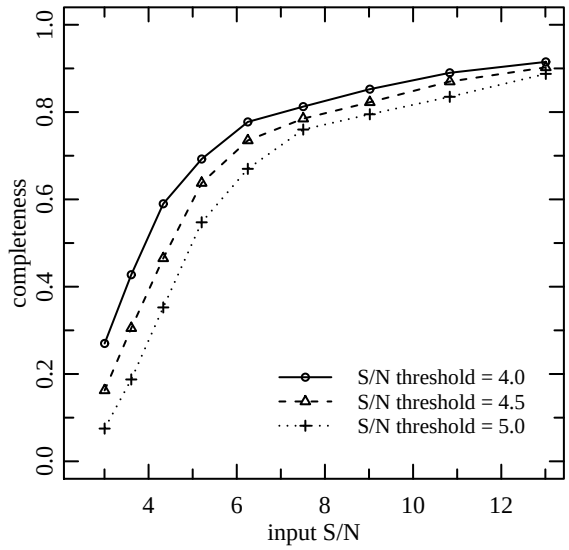

Figure 4.9: The detection completeness as a function of input object brightness (in terms of S/N computed with the noise level) for the three different values of the detection threshold S/N indicated in the figure.

but stays lower than 90% at large input S/N, and this can be explained by the effect of OH masks that cover about 20% of the observed wavelength range. Indeed, we confirmed that the completeness became close to 100% when we carried out the same simulation excluding the OH mask regions. The completeness is about 40% for the input S/N same as the adopted S/N threshold, which is a reasonable result expected from statistical fluctuation and the OH mask effect.

Chapter 5

The FastSound Spectroscopic Sample

5.1 Statistical Properties of the Emission-line sample

We detected 4,797 emission line candidates at $S/N \geq 4.0$ in all the FastSound data set. It should be noted that the number of galaxies hosting these candidates is 4,119, because ~ 200 galaxies are detected with more than two different lines (see Okada et al. 2015), and ~ 400 galaxies are detected in two different FastSound FoVs because they were observed twice in the regions of two overlapping FMOS FoVs. Typically, the number of detected emission line galaxies in one FMOS FoV is about 10% of the 400 fibers. This relatively low success rate is consistent with that obtained in our pilot observations reported in §2.2.4. The main reasons were the uncertainty in the photometric redshift estimates, which is large relative to the FastSound redshift coverage, and the uncertainty in the Hα estimates. There are about 380 Hα emitters in one FMOS FoV whose Hα fluxes are detectable by FMOS, and hence a detection efficiency close to 100% should be possible, if the target selection is perfect. However, only about 1/3 of them remain after the photo-z cut, and another $\sim 1/3$ remain after the Hα flux and color cuts, resulting in $\sim 10\%$ detection efficiency.

Not all the 4,797 line candidates cannot be guaranteed to be real emission lines, as the false line detection rate cannot be reduced to zero. The false detection rate increases with decreasing threshold of the line S/N. The number of false detections is estimated by applying *FIELD* to inverted images, which are obtained by exchanging object and sky frames in the reduction process. It is expected that the rate of false detection of spurious objects should be the same for the normal (Obj.−Sky) and inverted (Sky−Obj.) frames, because the analysis procedures are exactly the same except for swapping the object/sky frames. (Absorption

Table 5.1: The statistics of the detected line candidates in all the FastSound data set. Statistics for both the normal (Obj.−Sky) and inverted (Sky−Obj.) images are presented. The inverted frames should include only spurious objects.

	Obj.−Sky (1)	Sky−Obj. (2)	Contamination (2)/(1)
$S/N \geq 5.0$	3,080	72	2.3%
$S/N \geq 4.5$	3,769	170	4.5%
$S/N \geq 4.0$	4,797	441	9.2%
$S/N \geq 3.5$	6,805	1,510	22.2%
$S/N \geq 3.0$	12,795	6,279	49.1%

lines may appear as emission lines in the inverted frames, but the continuum emission is hardly detected for most of FastSound galaxies and absorption lines are under the detection limit.)

The numbers of detected line candidates in all the FastSound data in normal and inverted frames are summarized in Table 5.1 and shown as a cumulative histogram of S/N in Figure 5.1. The contamination of spurious objects is about 10% above $S/N = 4$, and sharply increases for a lower S/N threshold. The increase in number of line candidates in the normal frames and that in the inverted frames below $S/N = 4$ are similar, implying that few lines are real in low S/N. The number of real emission lines detected by FastSound can be estimated to be about $4,300$ at $S/N \geq 4$. The 441 lines at $S/N \geq 4$ in the inverted frames are hosted by 398 galaxies, and hence the number of galaxies with real emission lines above this S/N should be $4,119 - 398 \sim 3,700$. More than 90% of these lines are expected to be Hα (Tonegawa et al. 2014a; Okada et al. 2015). The distribution of detected objects found in the normal and inverted frames on the celestial sphere is presented in Figure 5.2.

The wavelength of the detected objects in normal and inverted frames are presented against S/N in Figure 5.3. Here, the wavelengths were derived by 1D Gaussian fits with a velocity dispersion as a free parameter for detected lines. When an OH mask region is overlapping with a line, the line center may be on the mask region. The number of fake lines on the inverted frames rapidly increases below $S/N = 5.0$, indicating that one should adopt some S/N threshold not to include spurious objects into analysis.

The flux distribution of emission line candidates detected by *FIELD* is presented in figure 5.4, for normal frames and inverted frames, and for different S/N thresholds. Fluxes

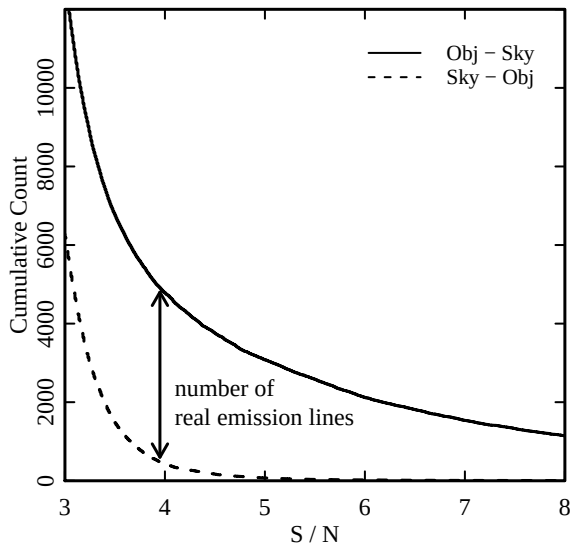

Figure 5.1: The cumulative S/N distribution of all the emission line candidates in the FastSound survey. The solid and dashed lines show the number of candidates detected in the normal and inverted frames, respectively. The number of real emission lines can be estimated by the difference between the two.

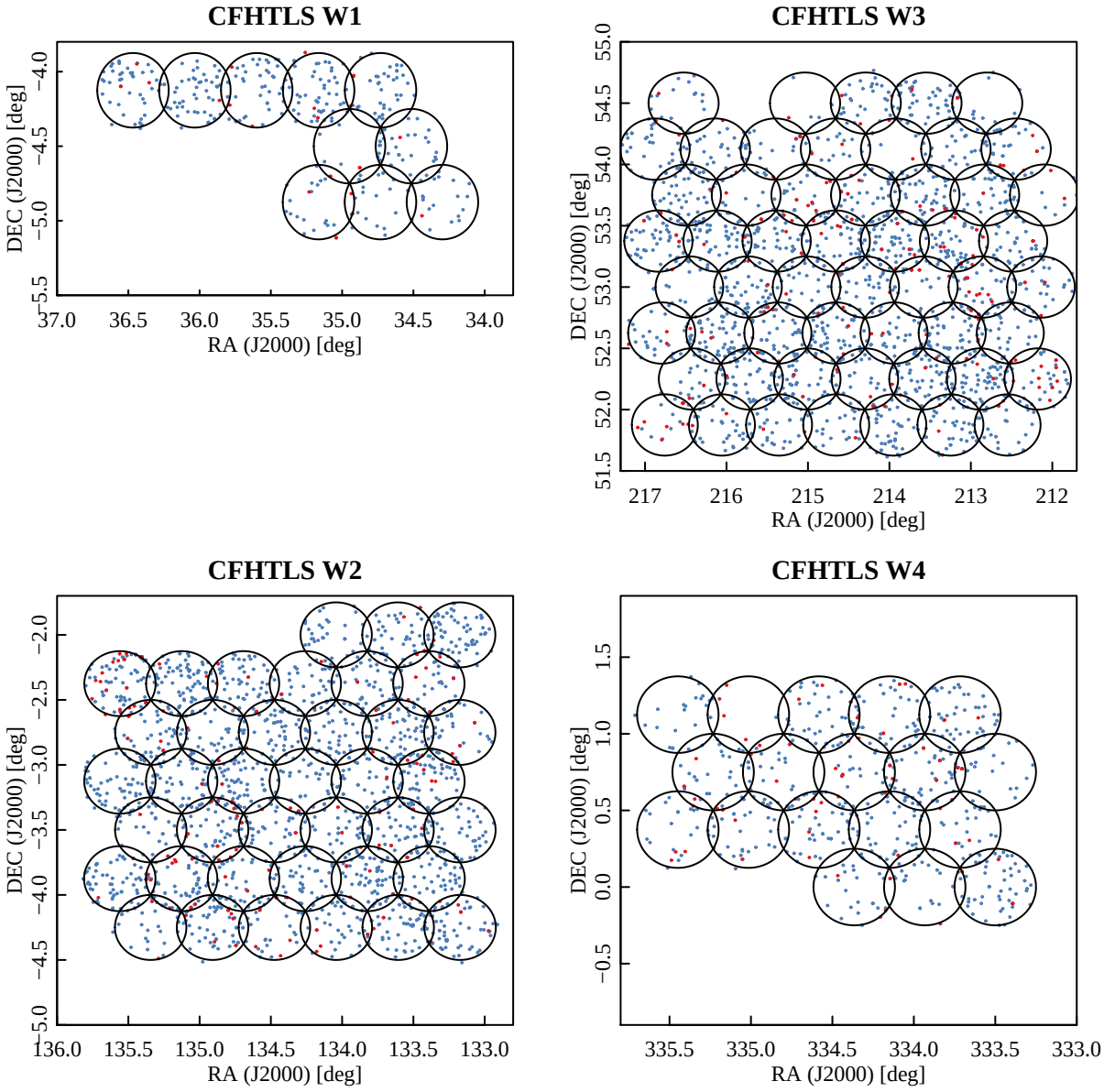

Figure 5.2: The distribution of emission line objects in the celestial sphere detected by FIELD. Blue points are those detected in the normal frames while red points are in the inverted frames. The circles are FoVs of FMOS. Detection threshold is $S/N = 4.0$ for this figure.

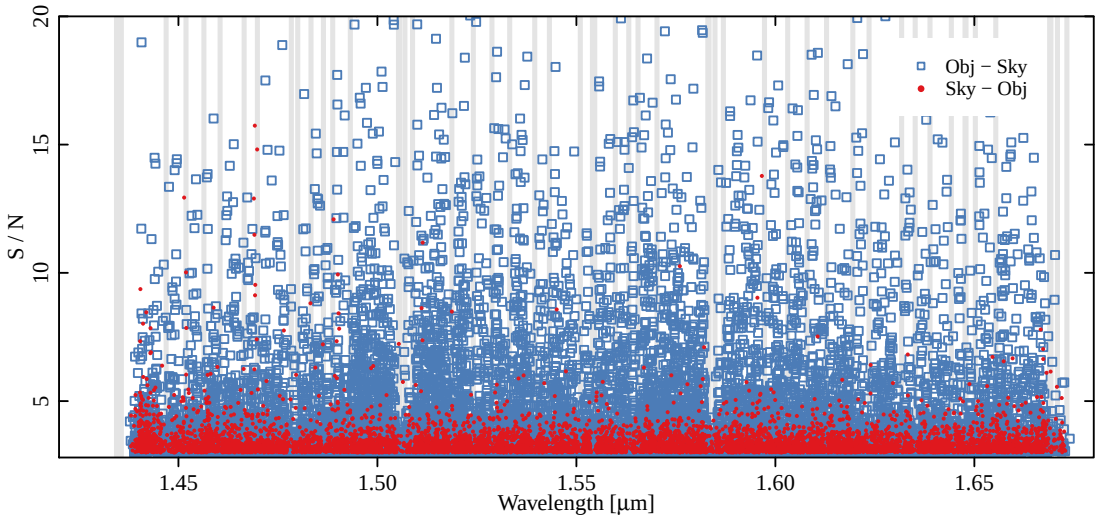

Figure 5.3: The S/N of emission line plotted against the observed wavelength. Blue and red symbols represent the detected objects in normal and inverted frames, respectively. Grey vertical stripes show the positions of OH masks of IRS2.

corrected for transparency and the fiber loss effect are used to produce figure 5.4. Also, the comparison between S/N and the corrected line flux is given in figure 5.5. It is seen from figure 5.5 that the Hα flux of $\sim 2.0 \times 10^{-16}$ [erg/cm^2/s] corresponds to $S/N \sim 5$. However, the scatter is large, and therefore, we need the condition about S/N (such as $S/N > 5.0$) rather than Hα flux (such as $F_{\mathrm{H}\alpha} >\sim 2.0 \times 10^{-16}$ [erg/cm^2/s]), to reduce the false detection rate, as seen in figure 5.4.

5.2 Catalog Production and Data Release

The FastSound data will be public from January 2016. The FastSound catalog data comprise of four text files for four CFHTLS fields: (1) field list files, (2) object catalogs, (3) emission line catalogs, and (4) inverted emission line catalogs. The contents of each file is summarized in Table 5.2, 5.3, and 5.4. In the following, I give additional information on certain columns.

(1) field list files

This file contains basic properties of each FoV such as observation date, the number of target objects, and seeing. Some columns in this file are useful for creating selection

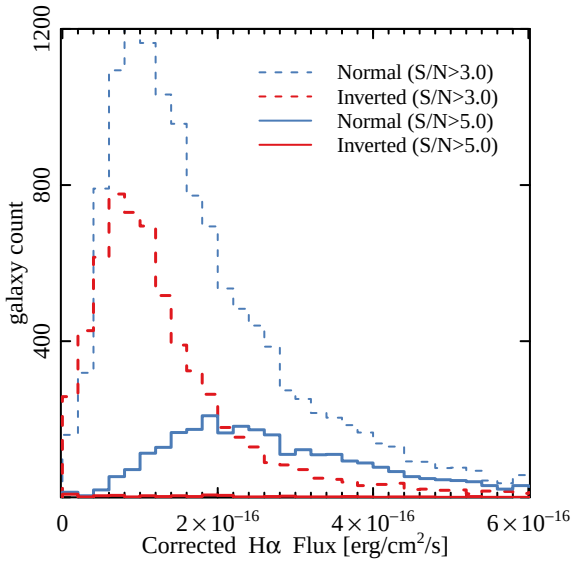

Figure 5.4: The histogram of the corrected Hα flux of emission lines detected by *FIELD*. The blue line is for the normal frames, while the red line is for the inverted frames, in which all emission line candidates are false.

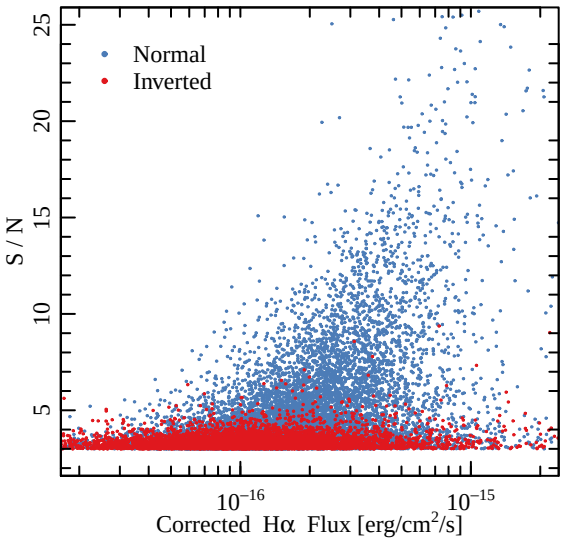

Figure 5.5: The signal-to-noise ratio of emission line detection plotted against the corrected Hα line fluxes. Blue dots represent the normal frames, while red points represent the inverted frames.

function for clustering analysis, while others are useful for calibrating infalling flux to derive physical properties of galaxies.

- `Observation Date:` For IRS1, the mask mirror had been replaced in December 2013, and radial selection function will be different between these periods.
- $N_{\rm tar}$: The number of selected galaxies as candidates of spectroscopic targets within 0.278 [deg] distance from the center of FoV. See §2.3 for the detail of the target selection. The outermost fibers can patrol slightly exceeding 0.25 [deg], and the most distant object was at 0.278 [deg] in our whole sample.
- $N_{\rm obs}$: The number of galaxies to which the FMOS fibers for IRS1/2 were allocated. The value -99 means that the IRS1/2 was not functional and unobserved due to an instrumental trouble.
- $N_{\rm el}$: The number of emission line candidates of IRS1/2 frames detected by FIELD. -1 for unobserved. The same quantity for the inverted frames ($N_{\rm el,f}$) is also provided.
- $N_{\rm g}$: The number of galaxies which possess at least one line candidate in IRS1/2 frames. -1 for unobserved. The same quantity for the inverted frames ($N_{\rm g,f}$) is also provided.
- `seeing:` The seeing during the exposure of the FoV. This is typically measured by applying Gaussian fit to the image of the sky camera of FMOS taken during the re-allocation between the first exposure for sky and the second exposure for objects.
- $\langle f_{\rm obs} \rangle$: The mean of ratios of observed flux to photometric data for calibration stars. -9.99 for unobserved. Divide the line fluxes in the emission line catalog by these numbers, to get the best estimates for the total fluxes from point sources. For galaxies, further (model dependent) correction would be necessary. The simplest correction (see §4.1) was done and provided in the emission line catalog below.

(2) object catalogs

This is the object list for W1-4 fields, including all target galaxies observed by FastSound regardless of emission line detection. The photometric properties and the estimated physical quantities are listed.

Table 5.2: Catalog columns for the FastSound field list files.

Column	Column Name
1	Observation Date
2	Field Name
3	RA_cent
4	DEC_cent
5	$N_{\rm tar}$
6,7	$N_{\rm obs}$ for IRS1/2
8,9	$N_{\rm el}(S/N > 4.5)$ for IRS1/2
10,11	$N_{\rm g}(S/N > 4.5)$ for IRS1/2
12,13	$N_{\rm el}(S/N > 3.0)$ for IRS1/2
14,15	$N_{\rm g}(S/N > 3.0)$ for IRS1/2
16,17	$N_{\rm el,f}(S/N > 4.5)$ for IRS1/2
18,19	$N_{\rm g,f}(S/N > 4.5)$ for IRS1/2
20,21	$N_{\rm el,f}(S/N > 3.0)$ for IRS1/2
22,23	$N_{\rm g,f}(S/N > 3.0)$ for IRS1/2
24	typical seeing
25,26	$\langle f_{\rm obs} \rangle$
27,28	$\sigma_{\langle f_{\rm obs} \rangle}$

- `(MAG_AUTO,MAG_ERROR)`: Optical magnitudes $u^*g'r'i'z'$ are derived from the CFHTLS Wide catalog created by Gwyn (2012) and NIR magnitudes JK from UKIDSS DXS (Lawrence et al. 2007) if the counterparts exist. Galactic extinction is corrected using $E(B-V)$ map of Schlegel et al. (1998).
- `Photometric Redshift Flag`: If 1, z_{ph} derived from CFHTLS official photometric redshift are used for our target selection, and if 2, z_{ph} calculated by FastSound are used.
- $z_{\rm min}$, `zPDF_ML, zPDF_l68, zPDF_h68`: The maximum likelihood value, median, and lower and upper limit of 68% confidence level for the photometric redshift derived by *LePhare* and empirical SED template using $u^*g'r'i'z$. The peak $z_{\rm min}$ can be outside the lower and upper limit if the probability distribution function is not simple.
- `Stellar Mass, Star Formation Rate`: Derived by *LePhare* with theoretical template using $u^*g'r'i'z$. The peak of PDF, lower limit, median, upper limit are provided as well as photometric redshifts.
- `Intrinsic` $E(B-V)$: The expected color excess of each galaxy derived by the SED fittings.
- $F_{\rm H\alpha,est}$: The estimated Hα flux derived from SFR expectation value. See 2.2.2 for the procedure in detail. Lower and upper limits of $F_{\rm H\alpha,est}$ correspond to those for SFR.
- `Number of observations` $n_{\rm obs}$: In the FoV overlapping regions, some galaxies were observed more than once.
- `Number of emission lines` $n_{\rm line}$: The number of line candidates above certain S/N thresholds in the normal frames. If $n_{\rm obs} \geq 2$, the physically same line will be counted more than twice.
- `Number of emission lines` $n_{\rm line,inv}$: The same as $n_{\rm line}$, but for the inverted frames.

(3) emission line catalogs

This file is the catalog of emission lines detected by FIELD (§4.2). The threshold of S/N is 3.0.

Table 5.3: Catalog columns for the FastSound object catalogs.

Column	Column Name	Reference	Unit
1	CFHTLS-Wide ID	Gwyn (2012)	
2	RA	Gwyn (2012)	deg
3	DEC	Gwyn (2012)	deg
4–13	(MAG_AUTO,MAG_ERR) for $u^*g'r'i'z$	Gwyn (2012)	
14–17	(MAG_AUTO,MAG_ERR) for JK	Lawrence et al. (2007)	
18	Galactic $E(B-V)$	Schlegel et al. (1998)	
19	$z_{\rm ph}$ flag	§2.2.2	
20	$z_{\rm min}$	§2.2.2	
21	zPDF_l68	§2.2.2	
22	zPDF_ML	§2.2.2	
23	zPDF_h68	§2.2.2	
24	FastSound $z_{\rm ph}$	§2.2.2	
25	Stellar Mass	§2.2.2	$M_\odot$
26	Stellar Mass LOW68	§2.2.2	$M_\odot$
27	Stellar Mass ML	§2.2.2	$M_\odot$
28	Stellar Mass HIGH68	§2.2.2	$M_\odot$
29	SFR	§2.2.2	$M_\odot$yr$^-$1
30	SFR_LOW68	§2.2.2	$M_\odot$yr$^-$1
31	SFR_ML	§2.2.2	$M_\odot$yr$^-$1
32	SFR_HIGH68	§2.2.2	$M_\odot$yr$^-$1
33	intrinsic $E(B-V)$	§2.2.2	
34	$F_{\rm H\alpha,est}$	§2.2.2	ergcm^{-2}s^{-1}
35	$F_{\rm H\alpha,est}$_l68	§2.2.2	ergcm^{-2}s^{-1}
36	$F_{\rm H\alpha,est}$_ML	§2.2.2	ergcm^{-2}s^{-1}
37	$F_{\rm H\alpha,est}$_l68	§2.2.2	ergcm^{-2}s^{-1}
38	$n_{\rm obs}$	§5.2	
39,40	$n_{\rm line}$ ($S/N>4.5$,$S/N>3.0$)	§5.2	
41,42	$n_{\rm line,inv}$ ($S/N>4.5$,$S/N>3.0$)	§5.2	

- `Emission line ID`: This column includes the FoV ID, spectrograph (IRS1/IRS2), fiber ID (1–200), and the line ID (increasing order of central wavelength). For example, "FastSound-W2_025-IRS1_005-2" means that this is the second shortest line of the object to which the fifth fiber of IRS1 spectrograph was allocated.
- `Central wavelength`: The central wavelength obtained by the fitting using Gaussian in the 1D spectrum.
- `Central wavelength (FIELD)`: Line SN peak location in 2D image calculated by the line detection software FIELD. Comparing this column and the above column will be a test of goodness of 1D spectrum fitting.
- `Corrected Line Flux`: The flux corrected for transparency and fiber aperture loss (see §4).
- `Flag_mask`: The line center is located in the OH masked regions if 1, and outside masked regions if 0.
- $\Delta\lambda_{\rm mask}$: Separation between the line center and the nearest mask edge for shorter/longer wavelength side. If the line is close to the OH mask, one should be cautious because a fraction of infall flux may have been decreased by the OH mask and the contamination from the residual OH lines may be present. For an example of the treatment of this issue for the clustering analysis, see Okumura et al. (2015).
- `Number of observations` $n_{\rm obs}$: In the FoV overlapping regions, some galaxies were observed more than once.
- `Number of emission lines` $n_{\rm line}$: The number of emission lines in the object within one observation / among all observations. One physically same lines in the repeated observations are counted twice if $n_{\rm obs} \geq 2$.
- `Rank of` S/N `of emission lines in the galaxy` $n_{\rm line}$: The S/N rank in the object within one observation / among all observations. To avoid redundant counting and to extract the brightest emission-line (probably Hα), extract the rows whose Col.57 is 1.

(4) inverted emission line catalogs

The content of this file is the same as (3), but detected objects in the inverted frames are listed. The statistics of spurious lines can be estimated by this catalog, in which all lines must be artificial ones.

Table 5.4: Catalog columns for the FastSound emission line catalogs and inverted line catalogs.

Column	Column Name	Reference	Unit
1	FastSound emission line ID	§5.2	
2–38	The same as Col. 1–37 of object catalogs.		
39	Line S/N	§4.2	
40	Central wavelength λ	§4.1	μm
41	σ_λ	§4.1	μm
42	Central wavelength λ (FIELD)	§4.2	μm
43	$F_{\mathrm{H}\alpha}$	§4.1	ergcm^{-2}s^{-1}
44	$\sigma_{F_{\mathrm{H}\alpha}}$	§4.1	ergcm^{-2}s^{-1}
45	Corrected $F_{\mathrm{H}\alpha}$	§4.1	ergcm^{-2}s^{-1}
46	Line Width	§4.1	Å
47	Error of Line Width	§4.1	Å
48	Flag_mask	§5.2	
49,50	$\Delta\lambda_{\mathrm{mask}}$	§5.2	Col.44
51,52	$\Delta\lambda_{\mathrm{line}}$	§5.2	Col.44
53	n_{obs}	§5.2	
54	n_{line} of the galaxy within one observation	§5.2	
55	S/N rank among Col.54	§5.2	
56	n_{line} of the galaxy within all observations	§5.2	
57	S/N rank among Col.56	§5.2	

- `Emission line ID`: The same as the emission line catalogs, but "_inv" is added to clarify that this is found on the inverted frame.

5.3 Measurement of the Growth Rate with FastSound sample

With the FastSound redshift catalog described in the previous section, we can measure the normalized growth rate $f\sigma_8$ from the two-point correlation function via redshift space

distortions. The detail of this analysis is explained by Okumura et al. (2015), and in this section, I will give a brief summary of Okumura et al. (2015), to highlight the usefulness of the FastSound data produced in this thesis for measuring $f\sigma_8$ at $z \sim 1.4$, and treating possible systematic errors.

The redshift space two-point correlation function is measured by the Landy-Szalay estimator (Landy & Szalay 1993):

$$\xi^s(r, \mu) = \frac{DD - 2DR + RR}{RR} \tag{5.3.1}$$

where DD, DR, and RR are the normalized number of pairs with transverse and radial separation (r_p, r_π) satisfying $\mu = r_\pi/\sqrt{r_p^2 + r_\pi^2}$. Here, D denotes the FastSound galaxy catalog and R denotes the random reference catalog without clustering. For example, DR means that one of the pair comes from the FastSound galaxy catalog and the other from the random catalog.

Controlling the systematics associated with observation is crucial for the measurement of the correlation function and hence deriving the final growth rate $f\sigma_8$. Especially, creating the random catalog which is used in Equation (5.3.1) is one of the most delicate tasks, because it serves as the reference for the real galaxy catalog, therefore, any systematic in the random catalog can lead to an artificial anisotropy of the two-point correlation function and a systematic error in $f\sigma_8$. The observation is subject to various effects which changes the observed number density along the line-of-sight $n(z)$ and the line detection efficiency for each FoV, hence these must be correctly included when we create the random catalog. The former is called the radial selection function, while the latter is called the angular selection function.

The first step in constructing the radial selection function is to obtain the redshift distribution of the FastSound galaxy catalog. The redshift distribution of FastSound galaxies is shown in Figure 5.6, where red boxes indicate the raw distribution directly from the emission line catalog. We adopt the functional form (Baugh & Efstathiou 1993):

$$n(z) = Az^2 \exp\left[-\frac{(z - z_c)^2}{\sigma_z^2}\right], \tag{5.3.2}$$

with A, z_c, and σ_z being free parameters, to obtain the radial selection function. The function (5.3.2) should be applied to the true distribution of the FastSound sample, but OH masks of FMOS decrease the line detection efficiency in the vicinity of themselves. In order to correct for this effect, we took the ratio of the number of FastSound galaxies to the mock catalog as

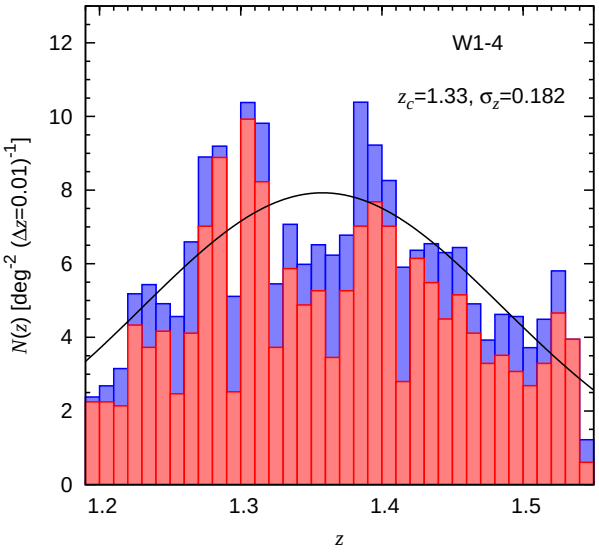

Figure 5.6: The redshift distribution of 2,783 FastSound galaxies in CFHTLS W1–W4 fields. Red boxes are the raw distribution while blue boxes are distribution corrected for the OH mask effect. The functional formula is applied to the blue histogram and shown as the black line. Taken from Okumura et al. (2015) (the same hereinafter).

a function of the wavelength distance from the nearest center of OH masks (Col. 49 and 50 of the emission line catalog), as displayed in Figure 5.7. It is seen that the decrease of line detection efficiency becomes zero beyond $\sim 0.0010\mu$m, which is reasonable considering the width of a OH mask (~ 8 pixels), the typical width of emission lines on the detector (4.26 pixels, see §4.2), and the pixel scale ~ 1.1 [Å/pix], because this decrease is caused by the overlapping of emission lines and OH masks. The plots in Figure 5.7 is fitted by a simple function:

$$g(\delta\lambda) = \begin{cases} 831.5\delta\lambda + 0.06 & (\delta\lambda \leq 0.00113\mu\mathrm{m}) \\ 1 & (\delta\lambda > 0.00113\mu\mathrm{m}). \end{cases} \tag{5.3.3}$$

This function is used to correct the raw redshift distribution (red boxes, Figure 5.6) for the OH mask effect. The resulting distribution is expressed by the blue boxes in Figure 5.6 and equation (5.3.2) is fitted to this distribution, yielding $(z_c, \sigma_z) = (1.34, 0.179)$, which is also shown in Figure 5.6 by the solid line.

The angular selection function needs to be calculated as well as the radial selection function, in order to incorporate the difference in the observing condition for each FoV. We simply calculate the ratio of the number of emission line galaxies N_g to the number of target

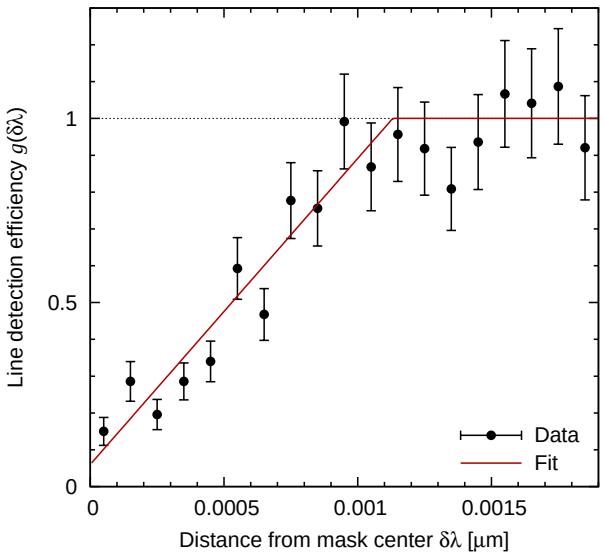

Figure 5.7: The ratio between the number of FastSound galaxies and mock galaxies as a function of wavelength distance from the center of OH masks. The red line is a fitting function (5.3.3).

galaxies selected by the selection criteria N_{tar}. These values can be found in Col. 5, 10 and 11 in the FoV list file (see §5.2). This value reflects the difference of the observing condition (e.g., weather condition and seeing) and fiber allocation efficiency for each FoV, because $N^{\rm g}/N^{tar}$ should be uniform if these two factors are same for all the FoVs.

The random catalog is created using the radial selection function and angular selection function as derived above. Note that the decrease of the detection efficiency due to the OH masks is taken into account again, using equation (5.3.3).

The data-data pairs DD at small scales need to be corrected for the fiber collision effect, where the number of observed pairs is reduced at highly clustered regions because some of targets are not allocated with fibers due to the minimum allowed separation between neighboring fibers. In order to correct for this effect, we calculate the ratio $[1+w^{\rm fib}(\theta)]/[1+w^{\rm tar}(\theta)]$ as a function of angular separation θ, where $w^{\rm fib}(\theta)$ is the angular correlation function of the FastSound galaxies to which fibers were assigned, and $w^{\rm tar}(\theta)$ is that for target galaxies selected by the criteria (§2.3). Figure 5.8 shows the $[1+w^{\rm fib}(\theta)]/[1+w^{\rm tar}(\theta)]$, together with the fitting function

$$[1+w^{\rm fib}(\theta)]/[1+w^{\rm tar}(\theta)] = \exp\left[-(\theta/\theta_0)^{-\alpha}\right], \tag{5.3.4}$$

with the best-fit parameters $(\theta_0, a) = (0.188, 1.22)$. It is seen that the fiber collision effect

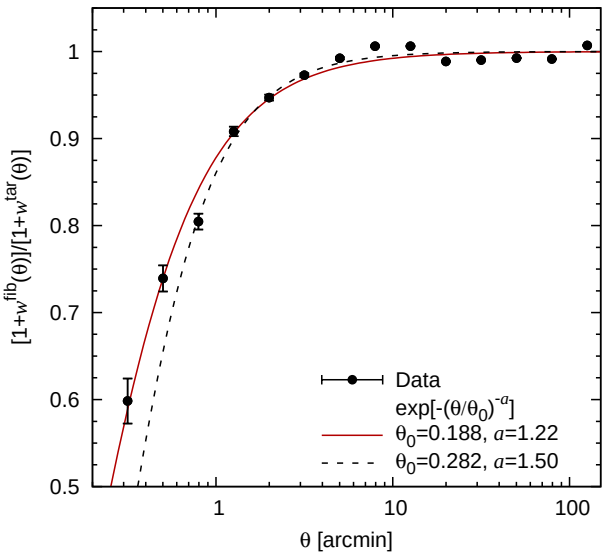

Figure 5.8: The ratio $[1 + w^{\rm fib}(\theta)]/[1 + w^{\rm tar}(\theta)]$ as a function of angular separation θ, where $w^{\rm fib}(\theta)$ is the angular correlation function of fiber-allocated galaxies while $w^{\rm tar}(\theta)$ is that of galaxies selected by the FastSound selection criteria. The solid line is the best-fit model (5.3.4) with (θ_0, a) being determined using $0.3 < \theta < 50$ [arcmin]. The dashed line is similar, but $0.7 < \theta < 50$ [arcmin] is used for the model fitting.

becomes prominent below $\sim$ 10 arcsec, which is consistent with the designed minimum separation of 12 arcsec. Inverse of this function is multiplied to the observed DD pairs, to recover the true pair count at small scales.

Finally, we need the correction of the overall amplitude of the two-point correlation function, because the false detection of line search (see §4.2) and contamination from other emission lines can affect the measured correlation function. They appear in the emission line catalog as mistaken redshifts and deteriorate the anisotropy of the correlation function, hence resulting in a systematic error of $f\sigma_8$. We correct for this effect by applying a correction factor $(1-f_{\rm fake})^2(1-f_{\rm OIII})^2$, where $f_{\rm fake} = 0.041$ is the false detection rate obtained from the ratio between the number of galaxies in the real and inverted catalog and $f_{\rm OIII} = 0.032$ is the contamination from [OIII] lines, which was found to be the largest contamination (Okada et al. 2015).

The constraint of $f\sigma_8$ is based on the monopole ($l = 0$) and quadrupole ($l = 2$) compo-

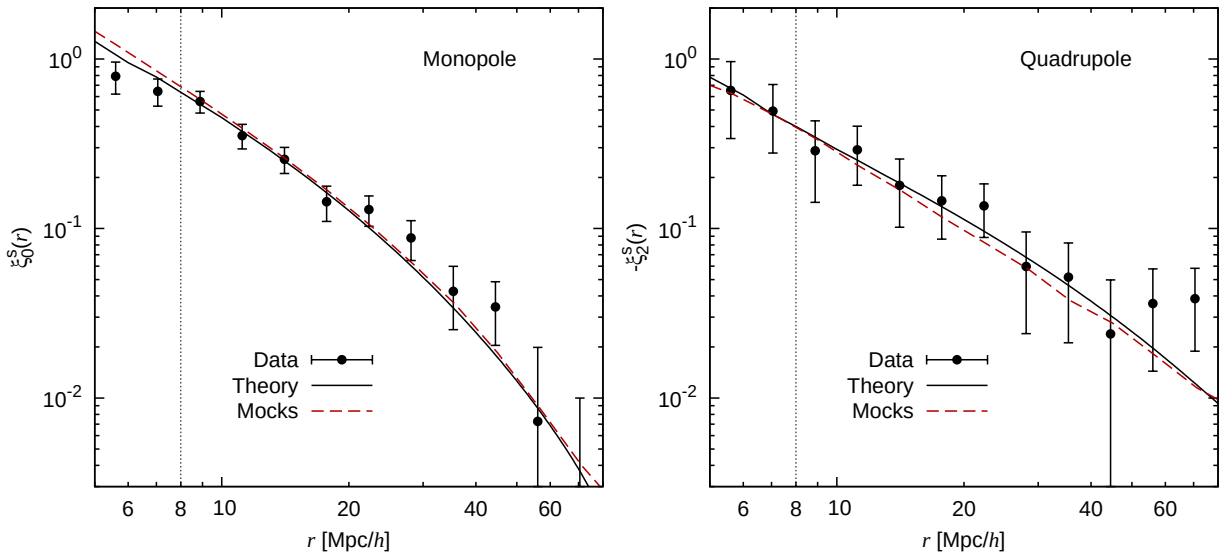

Figure 5.9: The correlation function of the FastSound sample. The left panel is the monopole $\xi^s_1(r)$ and the right is the quadrupole $-\xi^s_2(r)$. Observed values are represented by black points, with error bars estimated using mock catalogs. Black solid lines show the best-fitting model (Kaiser model with non-linear matter power spectrum), with parameters $(f\sigma_8, b\sigma_8) = (0.478, 0.818)$, corrected for the redshift blunder effects. Red dashed lines are the same as the black lines but mock catalogs are used instead. The vertical lines are the minimum scale we adopted.

nents of two-point correlation:

$$\xi^s_l(r) = \frac{2l+1}{2}\int_{-1}^{1} \xi^s(r,\mu)\mathcal{L}_l(\mu)d\mu \tag{5.3.5}$$

where $\mathcal{L}_l$ are the Legendre polynomials. The correlation function $\xi^s(r,\mu)$ is measured by equation (5.3.1) using the emission line catalog and the random catalog prescribed above, with the binning size of $\Delta \log_{10} r = 0.1$ and $\Delta\mu = 0.1$. Then $\xi^s_1(r)$ and $\xi^s_2(r)$ is extracted using equation (5.3.5) by taking the sum over μ. Figure 5.9 shows the two-point correlation function $\xi^s_1(r)$ and $\xi^s_2(r)$ using conservatively selected 2783 galaxies in W1–4 fields (Okumura et al. 2015). The error bars are estimated by measuring the correlation functions of 640 mock catalogs, which are created using N-body simulation (Ishikawa et al. 2014) and halo occupation distribution (HOD) model (Cooray & Sheth 2002; Zheng et al. 2005) constrained by the real-space clustering of the FastSound galaxies (Hikage et al, in prep.).

To predict the theoretical correlation function, we use the Kaiser model with non-linear

matter power spectrum

$$P^s(\boldsymbol{k}) = (b + f\mu^2)^2 P_{\delta\delta}(k) G^2(k\mu\sigma_v) \tag{5.3.6}$$

where b is the linear galaxy bias and $G = \exp\left[-(k\mu\sigma_v)^2/2\right]$ is the damping factor to incorporate the nonlinearities at small scales caused by the velocity dispersion. The improved version of HALOFIT (Smith et al. 2003) developed by Takahashi et al. (2012) is used to compute the non-linear matter power spectrum $P_{\delta\delta}$. Because $P_{\delta\delta}(k) \propto \sigma_8^2$, the free parameters are $f\sigma_8$, $b\sigma_8$, and σ_v. The power spectrum and correlation function are connected by Fourier transformation.

The constraint on $f\sigma_8$ is obtained by χ^2 minimization:

$$\chi^2(\theta) = \sum_{i=1}^{2N_{\rm bin}} \sum_{j=1}^{2N_{\rm bin}} [\xi_l^{\rm s,obs}(r_i) - \xi_l^{\rm s,pred}(r_i;\theta)]^t \; C_{ij}^{-1} \; [\xi_l^{\rm obs}(r_j) - \xi_l^{\rm pred}(r_j;\theta)] \tag{5.3.7}$$

where $\xi_l^{\rm s,obs}(r_i)$ is the measured correlation function and $\xi_l^{\rm s,pred}(r_i;\theta)$ is the theoretical prediction of the correlation function with free parameters $(f\sigma_8, b\sigma_8)$. The covariance matrix C_{ij}^{-1} is estimated using the 640 mock catalogs. We use the monopole and quadrupole components and they are measured in $N_{\rm bin}$ bins, hence the covariance matrix becomes $2N_{\rm bin} \times 2N_{\rm bin}$ matrix. We have found that the velocity dispersion for FastSound emission line galaxies is small, therefore, we fixed $\sigma_v = 0$ (see §4.2 and §5.1 of Okumura et al. 2015).

Figure 5.10 shows the joint constraint of parameters $(f\sigma_8, b\sigma_8)$ obtained from the FastSound galaxy sample. The constraint on the normalized growth rate is $f\sigma_8 = 0.482^{+0.116}_{-0.116}$, i.e., 4σ detection of RSD and consistent with the prediction of ΛCDM model $f\sigma_8 \sim 0.392$ within 1σ uncertainty.

Figure 5.11 shows the FastSound measurement of the growth rate $f\sigma_8$. Previous measurements by various projects, including 6dFGS (Beutler et al. 2012), the SDSS main galaxies (Howlett et al. 2015), the 2dFGRS (Song & Percival 2009), the SDSS LRG (Samushia et al. 2013), the BOSS LOWZ (Chuang et al. 2013), the BOSS CMASS (Reid et al. 2012),WiggleZ (Blake et al. 2011a), VVDS (Guzzo et al. 2008) and VIPERS (de la Torre et al. 2013), are also plotted. Lines in figure 5.11 is the theoretical prediction of GR and other modified gravity, whose amplitudes are determined using 7 data points denoted as filled triangles; 6dFGS (the effective redshift $z_{\rm eff} = 0.067$), SDSS LRG($z_{\rm eff} = 0.25$ and $z_{\rm eff} = 0.37$), the SDSS CMASS ($z_{\rm eff} = 0.57$), the highest redshift bin out of the four from the WiggleZ ($z_{\rm eff} = 0.78$), the VIPERS($z_{\rm eff} = 0.8$), which are selected as the tightest constraints among other surveys in the same survey area.

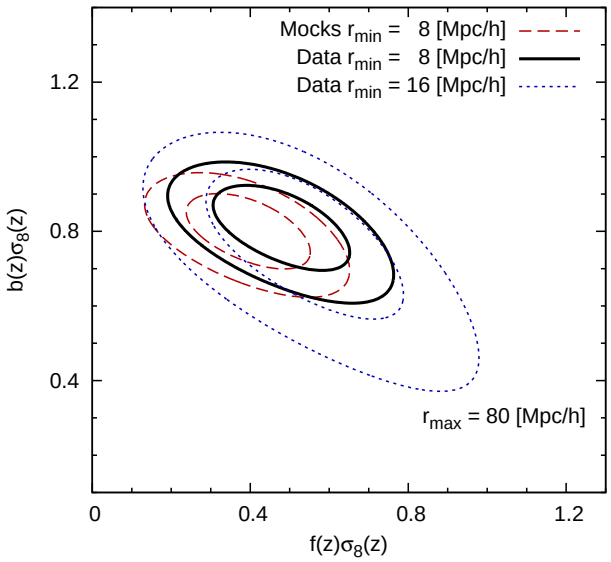

Figure 5.10: The joint constraint on $(f\sigma_8, b\sigma_8)$. The contours show 1σ and 2σ confidence limits. The solid and dotted lines are obtained from the two-point correlation function analysis of FastSound galaxies, with minimum scale of $8h^{-1}$ Mpc and $16h^{-1}$ Mpc. The dashed line is from mock catalogs. The maximum scale is $80h^{-1}$ Mpc and the velocity dispersion σ_v is fixed to be zero.

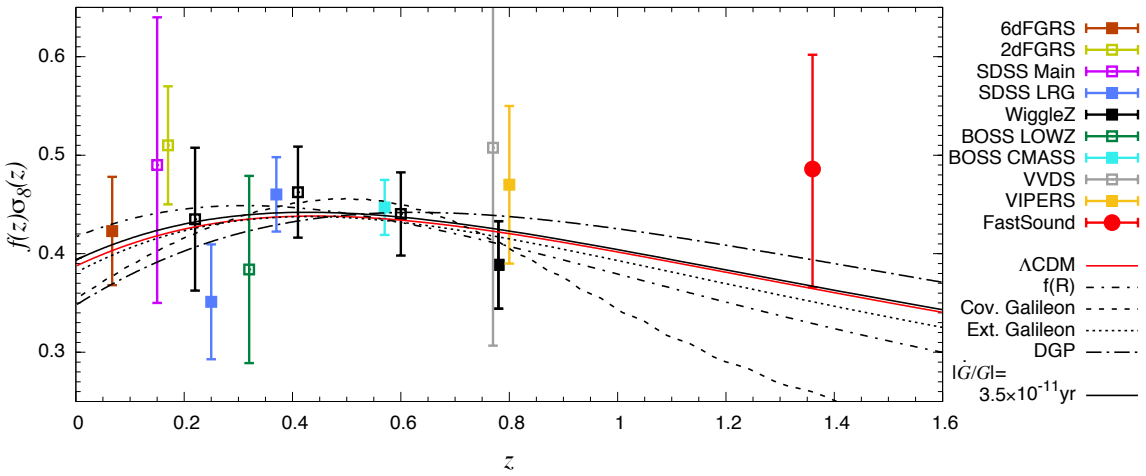

Figure 5.11: The constraints on the growth rate $f\sigma_8(z)$. The red symbol denotes the constraint from the FastSound data set, while other symbols represent various surveys at $z < 1$. The red solid line is the theoretical prediction of ΛCDM model in the framework of General Relativity. Predictions from several modified gravity theories are also drawn. The overall amplitudes of these lines are determined by χ^2 minimization using filled symbols.

The FastSound measurement is consistent with the ΛCDM model within 1σ level, though the error bar is relatively large due to the limited size of the survey. Some theoretical predictions deviate from our measurements, indicating that the FastSound data is useful to discriminate these theories. It is seen that the difference of $f\sigma_8$ predictions between gravity theories becomes larger at high redshifts if we determine the normalization using low-z data, suggesting the importance of tracing time dependence of $f\sigma_8$ in a wide redshift range. Future surveys such as PFS (Takada et al. 2014), DESI (Levi et al. 2013), HETDEX (Hill et al. 2008) will provide larger data sets at redshift $z > 1$, and it will be possible to test gravity theories by RSD more precisely. These surveys also target emission line galaxies as well as FastSound, therefore, the analysis methods developed and presented throughout this thesis will be useful to deal with these data to measure $f\sigma_8$ and put constraints on gravity theories as an origin of the accelerated expansion of the Universe.

Chapter 6

Conclusion

In the past decade, galaxy redshift surveys made a significant contribution to understanding the nature of dark energy as well as type Ia SNe and CMB. Galaxy clustering will continue to be one of the most important probe to obtain insights in the nature of dark energy, therefore, even larger surveys are currently being planned. FastSound is the first cosmological galaxy redshift survey designed to detect redshift space distortions (RSD) in the clustering of galaxies at $z \sim 1.4$. The survey targets Hα emission line galaxies using the near-infrared fiber multi-object spectrograph (FMOS) of the Subaru Telescope, which has a circular FoV with 30 arcmin diameter including 400 fibers. The main scientific goal of the project is to investigate the origin of the accelerated expansion of the Universe by testing General Relativity using a measurement of the growth rate of the large-scale structure. I have presented the fundamentals of this survey in this thesis.

In chapter 2, I showed the target selection and survey field of FastSound project. The pilot observation was carried out to examine the best target selection method using CFHTLS Wide optical photometric data. The color-based selections and photo$z$-based selections were compared, and the efficiency of adding UKIDSS near-infrared bands was examined. It was found that the selection from photometric redshifts tends to give a better efficiency than color-based methods, although there is no significant improvement by adding near-infrared band data within the statistical scatter. Considering the limited coverage of UKIDSS near-infrared data into account, we determined not to use the UKIDSS data in our target selection. The FMOS FoVs were arranged so as to overlap with other surveys to maximally pursue the legacy value.

In chapter 3, I gave the detail of the FastSound observations. The observations were

carried out over 35 nights from April 2012 to July 2014. We observed 121 FMOS FoVs in total (10, 39, 54, and 18 for W1–4, respectively), corresponding to a total area of 20.6 deg^2 tiled with a continuous hexagonal pattern.

In chapter 4, I presented the data processing and the development of a dedicated software algorithm for an automated emission line detection. The FMOS images were first reduced with the standard pipeline (*FIBRE-pac*). An important study in treating a large spectroscopic data set is to automatically search and detect emission lines. Residual OH airglow lines near the OH mask regions and cosmic rays frequently show spectral shapes similar to those of real emission lines on FMOS 2-D images. Because these spurious lines will deteriorate the galaxy clustering power spectra, an efficient automatic line detection with minimized probability of false detection was needed. I have developed an software algorithm for this purpose. Two-dimensional spectral images are used in this algorithm in order to detect faint emission line features, while efficiently filtering out unwanted spurious detections. Also, bad pixels on the detectors and pixels affected by cosmic-rays are efficiently removed by using the information obtained from the FMOS analysis pipeline, resulting in the false detection rate of $\leq 5\%$ above $S/N = 4.5$. Furthermore, the contamination fraction of spurious objects is estimated by inverted 2-D spectral images, which are obtained by exchanging object and sky image in the image reduction process, and in which all detections should be false. These organized procedures enabled us to produce the uniform redshift catalog and discuss systematic errors in the clustering analysis.

In chapter 5, I presented the basic statistical properties of FastSound data obtained by the procedure explained in the previous chapter, and gave the instruction of FastSound catalog, composed of FoV list files, object catalogs, emission line catalogs, and inverted emission line catalogs. The $f\sigma_8$ measurement from the two-point correlation function based on this sample was presented, to demonstrate the usefullness of this data set. We obtained $f\sigma_8 = 0.482^{+0.116}_{-0.116}$, which is consistent with the ΛCDM prediction within 1σ uncertainty. This is the first constraint on $f\sigma_8$ beyond $z = 1$, and we found that measuring $f\sigma_8$ in this redshift range have the potential to descriminate some classes of modified gravity theories.

Various studies are possible using the FastSound data. For example, revealing the mass-metallicity relation at high redshift by metallicity measurement from the stacked [NII] lines and its implication for galaxy evolution is presented by Yabe et al. (2015). This data is useful not only for cosmological analysis, but also for the galaxy formation/evolution at redshift $z \sim 1.4$. The data will be released at the FastSound official website in January

2016.

Larger redshift surveys are being planned to provide tighter constraint on the cosmological parameters or to test gravity theories. These surveys also target the distant universe ($z > 1$) and emission line galaxies, therefore, what are presented in this thesis will be of use to treat these data to investigate the nature of dark energy and put constraints on theories of modified gravity as an origin of the accelerated expansion of the Universe.

Acknowledgements

First of all, I express my sincere thanks to Prof. Tomonori Totani for his long-term encouragement and direction through this study. It has been fortunate for me to experience the frontier of cosmology by being engaged in the FastSound project. Also, his insights over wide field of astronomy and physics generate excitement for me and I have learnt so much from his attitude as a researcher.

I gratefully acknowledge the present and past present members of the laboratory. I have acquired considerable knowledge about variety field of astrophysics other than cosmology, from Assistant Prof. Norita Kawanaka. His talks at the "Astroph Coffee" time was informative about the cutting-edge research in the field of high-energy astrophysics. Dr. Ikkoh Shimizu also taught me a lot about galaxy formation and evolution, during his one-year stay at Totani laboratory. He also helped me analyzing the FastSound data.

I am grateful to my seniors and juniors in Totani laboratory. Mr. Sumiyoshi devoted to the planning of FastSound and data analysis from the very beginning of this project, so my study owes much to his preceding studies. I learned the practical skills and knowledge for a redshift survey from him. I thank Dr. Ishikawa and Mr. Okada for fruitful discussions as the members of FastSound project.

FastSound project has been carried out using the most advanced instrument FMOS, therefore, I would like to acknowledge the continuous support from the FMOS development team. I thank Associate Prof. Fumihide Iwamuro very much for the guidance of FMOS data analysis. Also I am grateful to Assistant Prof. Naoyuki Tamura and Dr. Kiyoto Yabe for supporting us to perform the observation every time.

This work is based on the published papers about FastSound. I would like to thank the co-authors of these papers for the resourceful comments and suggestions. Especially, Prof. Koji Ohta, Prof. Gavin Dalton, Prof. Karl Glazebrook, Associate Prof. Tomotsugu Goto and Associate Prof. Masayuki Akiyama carefully read the draft of my papers every

time and gave me many comments to improve quality of the papers.

I wish to thank the members of the Department of Astronomy, UTokyo during the cooperation for three years. Ms. Ishikawa and Ms. Asakawa helped me with office work and enabled me to concentrate on research. I had opportunities of giving talks in the observational cosmology seminar, where I had an experience of discussion and presentation.

Last but not least, I appreciate very much to my parents for supporting me.

The FastSound project was supported in part by MEXT/JSPS KAKENHI Grant Numbers 19740099, 19035005, 20040005, 22012005, and 23684007.

References

Anderson, L., et al. 2012, MNRAS, 427, 3435

Arnouts, S., Cristiani, S., Moscardini, L., Matarrese, S., Lucchin, F., Fontana, A. & Giallongo, E. 1999, MNRAS, 310, 540

Austermann, J. E., Aird, K. A., Beall, J. A., et al. 2012, Proceedings of SPIE, 8452, 84521E

Baugh, C. M., & Efstathiou, G. 1993, MNRAS, 265, 145

Bennett, C. L., Banday, A. J., Gorski, K. M., et al. 1996, ApJL, 464, L1

Beutler, F., et al. 2011, MNRAS, 416, 3017

Beutler, F., et al. 2012, MNRAS, 423, 3430

Beutler, F., Saito, S., Seo, H.-J., et al. 2014, MNRAS, 443, 1065

BICEP2 Collaboration, Ade, P. A. R., Aikin, R. W., et al. 2014, Physical Review Letters, 112, 241101

Bielby, R., Hill, M. D., Shanks, T., et al. 2013, MNRAS, 430, 425

Blake, C., et al. 2011, MNRAS, 415, 2876

Blake, C., et al. 2011, MNRAS, 415, 2892

Bolzonella, M., Miralles, J.-M., & Pelló, R. 2000, A&A, 363, 476

Brinchmann, J., Charlot, S., White, S. D. M., et al. 2004, MNRAS, 351, 1151

Calzetti, D., Armus, L., Bohlin, R. C., Kinney, A. L., Koornneef, J. & Storchi-Bergmann, T. 2000, ApJ, 533, 682

Chuang, C.-H., Prada, F., Beutler, F., et al. 2013, arXiv:1312.4889

Coe, D., Bradley, L., & Zitrin, A. 2015, ApJ, 800, 84

Cole, S., et al. 2005, MNRAS, 362, 505

Coleman, G. D., Wu, C.-C., Weedman, D. W. 1980, ApJS, 43, 393

Cooper, M. C., Aird, J. A., Coil, A. L., et al. 2011, ApJS, 193, 14

Cooray, A., & Sheth, R. 2002, Phys. Rep., 372, 1

Coupon, J, et al. 2009, A&A, 500, 981

Cutri, R. M., Skrutskie, M. F., van Dyk, S., et al. 2003, VizieR Online Data Catalog, 2246, 0

de la Torre, S., Guzzo, L., Peacock, J. A., et al. 2013, A&A, 557, A54

Dodelson, S. 2003, Modern cosmology / Scott Dodelson. Amsterdam (Netherlands): Academic Press. ISBN 0-12-219141-2, 2003, XIII + 440 p.,

Dvali, G., Gabadadze, G., & Porrati, M. 2000, Physics Letters B, 485, 208

Eisenstein, D. J., Zehavi, I., Hogg, D. W., et al. 2005, ApJ, 633, 560

Eisenstein, D. J., Seo, H.-J., & White, M. 2007, ApJ, 664, 660

FastSound team 2011,
http://www.kusastro.kyoto-u.ac.jp/Fastsound/documents/FMOS_Cosmology_proposal.pdf

Le Fèvre, O., et al. 2005, A&A, 439, 845

Cid Fernandes, R., Mateus, A., Sodré, L., Stasińska, G. & Gomes, J. M. 2005, MNRAS, 358, 363

Filippenko, A. V. 1997, ARA&A, 35, 309

Fioc, M., & Rocca-Volmerange, B. 1999, arXiv:astro-ph/9912179

Frieman, J. A., Turner. M. S. & Huterer, D. 2008, ARA&A, 46, 385

Furusawa, H., Kosugi, G., Akiyama, M., et al. 2008, ApJS, 176, 1

Garilli, B., et al. 2008, A&A, 486, 683

Geach, J. E., Smail, I., Best, P. N., Kurk, J., Casali, M., Ivison, R. J. & Coppin, K. 2008, MNRAS, 388, 1473

Gilbank, D. G., Baldry, I. K., Balogh, M. L., Glazebrook, K., & Bower, R. G. 2010, MNRAS, 405, 2594

Glazebrook, K., Tober, J., Thomson, S., Bland-Hawthorn, J., & Abraham, R. 2004, AJ, 128, 2652

Goranova, Y., et al. 2009, http://terapix.iap.fr/cplt/T0006-doc.pdf

Guzzo, L., et al. 2008, Nature, 451, 541

Guzzo, L., Scodeggio, M., Garilli, B., et al. 2014, A&A, 566, A108

Gwyn, S. D. J 2012, A&A, 143, 38

Hamilton, A. J. S. 1998, The Evolving Universe, 231, 185

Hanson, D., Hoover, S., Crites, A., et al. 2013, Physical Review Letters, 111, 141301

Hawkins, E., et al. 2003, MNRAS, 346, 78

Hill, G. J., Gebhardt, K., Komatsu, E., et al. 2008, Panoramic Views of Galaxy Formation and Evolution, 399, 115

Howlett, C., Ross, A. J., Samushia, L., Percival, W. J., & Manera, M. 2015, MNRAS, 449, 848

Hu, W., & Sawicki, I. 2007, Phys. Rev. D, 76, 064004

Ilbert, O., et al. 2006, A&A, 457, 841

Ishikawa, T., Totani, T., Nishimichi, T., et al. 2014, MNRAS, 443, 3359

Iwamuro, F. et al. 2012, PASJ, 64, 59

Johnson, A., Blake, C., Koda, J., et al. 2014, MNRAS, 444, 3926

Kaiser, N. 1987, MNRAS, 227, 1

Kaiser, N., Aussel, H., Burke, B. E., et al. 2002, Proceedings of SPIE, 4836, 154

Kennicutt, R. C., Jr. 1998, ARA&A, 36, 189

Kimura, M. et al. 2010, PASJ, 62, 1135

Kinney, A. L., Calzetti, D., Bohlin, R. C., McQuade, K., Strochi-Bergmann, T. & Schmitt, H. R. 1996, ApJ, 467, 38

Komatsu, E., Smith, K. M., Dunkley, J., et al. 2011, ApJS, 192, 18

Lawrence, A., et al. 2007, MNRAS, 379, 1599

Levi, M., Bebek, C., Beers, T., et al. 2013, arXiv:1308.0847

Lotz, J., Mountain, M., Grogin, N. A., et al. 2014, American Astronomical Society Meeting Abstracts #223, 223, #254.01

LSST Science Collaboration, Abell, P. A., Allison, J., et al. 2009, arXiv:0912.0201

Landy, S. D., & Szalay, A. S. 1993, ApJ, 412, 64

Linder, E. V. 2005, Phys. Rev. D, 72, 043529

Livio, M. 1999, arXiv:astro-ph/9903264

Maoz, D., & Mannucci, F. 2012, PASA, 29, 447

Martínez, V. J., Saar, E., Martínez-González, E., & Pons-Bordería, M.-J. 2009, Data Analysis in Cosmology, 665,

Matsumura, T., Akiba, Y., Borrill, J., et al. 2014, Journal of Low Temperature Physics, 176, 733

Okada, H., Totani, T., & Tsujikawa, S. 2013, Phys. Rev. D, 87, 103002

Okada, H., et al. 2015, submitted to PASJ (Paper II), arXiv:1504.05592

Okumura, T., et al. 2015, submitted to PASJ (Paper IV), arXiv:1511.08083

Peebles, P. J. E. 1980, Research supported by the National Science Foundation. Princeton, N.J., Princeton University Press, 1980. 435 p.,

Peebles, P. J. & Ratra, B. 2003, RvMP, 75, 559

Perlmutter, S., Aldering, G., Goldhaber, G., et al. 1999, ApJ, 517, 565

Pilbratt, G. L., Riedinger, J. R., Passvogel, T., et al. 2010, A&A, 518, L1

Planck Collaboration, Ade, P. A. R., Aghanim, N., et al. 2014, A&A, 571, AA16

Planck Collaboration, Ade, P. A. R., Aghanim, N., et al. 2015, arXiv:1502.01589

Press, W. H., Flannery, B. P., & Teukolsky, S. A. 1986, Cambridge: University Press, 1986,

The Polarbear Collaboration: P. A. R. Ade, Akiba, Y., Anthony, A. E., et al. 2014, ApJ, 794, 171

Reid, B. A., et al. 2012, MNRAS, 426, 2719

Riess, A. G., Filippenko, A. V., Challis, P., et al. 1998, AJ, 116, 1009

Sachs, R. K., & Wolfe, A. M. 1967, ApJ, 147, 73

Samushia, L, Percival, W. J & Raccanelli, A 2013, MNRAS, 420, 2102

Scalo. J. M. 1986, FCPh, 11, 1

Schaefer, B. E. 2007, ApJ, 660, 16

Schlegel, D. J., Finkbeiner, D. P & Davis, M. 1998, ApJ, 500, 525

Silk, J. 1968, ApJ, 151, 459

Smith, R. E., Peacock, J. A., Jenkins, A., et al. 2003, MNRAS, 341, 1311

Sobral, D., Best, P. N., Geach, J. E., Smail, I, Kurk, J., Cirasuolo, M., Casali, M., Ivison, R. J., Coppin, K. & Dalton, G. B. 2009, MNRAS, 398, 75

Sobral, D., Best, P. N., Matsuda, Y., Smail, I., Geach, J. E. & Cirasuolo, M 2012, MNRAS, 420, 1926

Sobral, D., Smail, I., Best, P. N., Geach, J. E., Matsuda, Y., Scott, J. P., Cirasuolo, M. & Kurk, J. 2013, MNRAS, 428, 1128

Song, Y.-S., & Percival, W. J. 2009, JCAP, 10, 004

Sumiyoshi, M. et al. 2009, arXiv:0902.2064

Takada, M., Ellis, R. S., Chiba, M., et al. 2014, PASJ, 66, R

Takahashi, R., Sato, M., Nishimichi, T., Taruya, A., & Oguri, M. 2012, ApJ, 761, 152

Tamura, N., et al. 2012, Proceedings of SPIE, 8446

Tokunaga "Infrared Astronomy" Allen's Astrophysical Quantities, Springer, 150

Tonegawa, M et al. 2014a, PASJ, 66, 43

Tonegawa, M et al. 2014b, DOI: 10.1093/pasj/psu127

Tonegawa, M., Totani, T., Okada, H., et al. 2015, PASJ, 67, 81

Wall, J. V., Jenkins, C. R., Ellis, R., et al. 2003, Practical statistics for astronomers, by J.V. Wall and C.R. Jenkins. Cambridge observing handbooks for research astronomers, vol. 3. Cambridge, UK: Cambridge University Press, 2003,

Wang, B., & Han, Z. 2012, NAR, 56, 122

Weinberg, S. 1972, Gravitation and Cosmology: Principles and Applications of the General Theory of Relativity, by Steven Weinberg, pp. 688. ISBN 0-471-92567-5. Wiley-VCH , July 1972.,

Weinberg, D. H., Mortonson, M. J., Eisenstein, D. J., et al. 2013, Phys. Rep., 530, 87

Yabe, K., et al. 2012, PASJ, 64, 60

Yabe, K., Ohta, K., Akiyama, M., et al. 2015, PASJ, 244

Zheng, Z., Berlind, A. A., Weinberg, D. H., et al. 2005, ApJ, 633, 791